Tracing the water cycle in the Atacama Desert using water isotopes (δ^2H, $\delta^{17}O$, $\delta^{18}O$) and pedogenic salt distributions

INAUGURAL-DISSERTATION

zur

Erlangung des Doktorgrades

der Mathematisch-Naturwissenschaftlichen Fakultät

der Universität zu Köln

vorgelegt von

Claudia Voigt

aus Leipzig

– Köln 2020 –

Berichterstatter / Gutachter:

Prof. Dr. Michael Staubwasser

Prof. Dr. Andreas Pack

Tag der mündlichen Prüfung: 29.05.2020

Abstract

Stable isotope ratios of water ($^{18}O/^{16}O$ and $^{2}H/^{1}H$) are widely used in hydrological studies. In contrast to classic tracers ($\delta^{2}H$–$\delta^{18}O$, d-excess), the triple oxygen isotope system ($\delta^{17}O$–$\delta^{18}O$, ^{17}O-excess) is virtually insensitive to changes in temperature and salinity, providing additional information on processes in the hydrological cycle. Large isotope effects associated with evaporation occur mainly in response to humidity. These isotope effects can be quantified by the classic Craig-Gordon evaporation model. The main objective of this thesis is to investigate the potential of combined analysis of hydrogen ($^{2}H/^{1}H$) and triple oxygen ($^{18}O/^{17}O/^{16}O$) isotopes of structurally bonded water of gypsum ($CaSO_4 \cdot 2H_2O$) to quantitatively estimate paleo-humidity and reconstruct past changes in the climatic conditions of the presently hyperarid Atacama Desert.

The first study serves to investigate recent dynamics in the isotopic composition of lake water in the complex hydrological system of the Salar del Huasco, Altiplano, Chile, that receives inflow from multiple sources and is affected by seasonal variability in precipitation, temperature and relative humidity. Isotope analyses of lakes and ponds from the Salar del Huasco revealed that their hydrological balance is mainly controlled by evaporation and recharge. Inflow from multiple sources and temporal variability in their isotopic composition lead to scattering of pond data along the evaporation trendline predicted by the Craig-Gordon model. Sporadic flooding events after heavy rainfalls can provoke significant mixing and lead to the emergence of non-recharged lakes. Evaporation without recharge as well as mixing processes can be identified by triple oxygen isotope analysis. The potential occurrence of episodic mixing processes, e.g. due to frequent flooding, should be taken into account in paleo-applications.

The second study presents first results of isotope analyses of structurally bonded water of gypsum from paleo-lake deposits in the Atacama Desert. The isotopic compositions of analyzed samples fall on distinct evaporation trends indicating the preservation of the primary isotope signal of paleo-lake water. A Craig-Gordon model together with a Monte Carlo simulation was used to determine the relative humidity that best fit the isotope data in both d-excess vs $\delta^{18}O$ space and ^{17}O-excess vs $\delta^{18}O$ space. The model output humidity is less affected by changes in the isotopic composition of source water and atmospheric vapor, however, can strongly depend on the selected wind induced turbulence coefficient and the limitations of the recharge rate (E/I). The model provides

reasonable humidity values if the input parameters are set within ranges reasonable for the site. Results imply humid conditions in the northern Atacama Desert about 3.5 million years ago that may have been facilitated by permanent El Niño like conditions in the Early Pliocene Warm Period (4.5 – 3.0 Ma).

The third study aims to improve the understanding of soil formation and secondary redistribution and transformation processes of evaporites in Atacama Desert soils, which is crucial for the interpretation of isotopic compositions of structurally bonded water of pedogenic gypsum. In this study, thin surface crusts, powdery surface material and subsurface concretions from up to 40 cm depth were sampled along several latitudinal transects between 19.5–25°S and 68.5–70.5°W. Results imply that long-term aridity gradients, sources and secondary mobilization processes control the spatial distribution of highly soluble salts – chlorides and nitrates – as well as gypsum and anhydrite in Atacama Desert soils. Hyperaridity is most persistent between 19-22°S. Exceptionally high chloride contents below the altitude of the atmospheric temperature inversion layer (< 1200 m) as well as Na/Cl ratios of 0.83 – close to the global sea water ratio of 0.86 – suggest sea spray as the primary source of halite. Generally, gypsum and anhydrite are the major minerals in Atacama Desert soils. The association of high anhydrite abundances with high chloride and nitrate contents indicate that anhydrite is a secondary product of dissolution-reprecipitation reactions in highly saline brines.

This thesis expands our knowledge of processes controlling the isotopic composition of structurally bonded water of lacustrine and pedogenic gypsum. The results contribute to the development of a powerful isotope tool that can allow for a quantitative reconstruction of past climatic mean states in the Atacama Desert.

Kurzfassung

Die Analyse stabiler Isotopenverhältnisse von Wasser ($^{18}O/^{16}O$ und $^{2}H/^{1}H$) findet häufig Anwendung in hydrologischen Studien. Im Gegensatz zum klassischen $\delta^{2}H$-$\delta^{18}O$ System (d-exess) ist das 3-Sauerstoffisotopensystem ($\delta^{17}O$-$\delta^{18}O$, ^{17}O-excess) nahezu unabhängig von der Temperatur und vom Salzgehalt und bietet somit zusätzliche Erkenntnisse über Prozesse im Wasserkreislauf. Isotopeneffekte, die mit der Verdunstung einhergehen, werden hauptsächlich durch die relative Luftfeuchte in der Atmosphäre kontrolliert. Diese Isotopeneffekte können mit dem klassischen *Craig-Gordon-Verdunstungsmodells* quantifiziert werden. Das Hauptziel dieser Arbeit ist es das Potenzial von Wasserstoff- ($^{2}H/^{1}H$) und 3-Sauerstoffisotopenanalysen ($^{18}O/^{17}O/^{16}O$) von strukturell gebundenem Wasser in Gips zu untersuchen, um die vergangene relative Luftfeuchtigkeit quantitativ abzuschätzen und Klimaschwankungen in der Vergangenheit der Atacama Wüste zu untersuchen.

Die erste Studie untersucht die Dynamik der Isotopenzusammensetzung des Seewassers im komplexen hydrologischen System des *Salar del Huasco*, Altiplano, Chile, welches durch verschiedene Quellen gespeist und durch saisonale Schwankungen in Niederschlag, Temperatur und relativer Luftfeuchtigkeit beeinflusst wird. Isotopenanalysen von Seen im *Salar del Huasco* zeigen, dass das hydrologische Gleichgewicht hauptsächlich durch Verdunstung und Zufluss gesteuert wird. Zuflüsse aus mehreren Quellen und zeitliche Variabilität in ihrer Isotopenzusammensetzung führen zu einer Streuung der Isotopendaten der Seen entlang des vom *Craig-Gordon-Modell* vorhergesagten Verdunstungstrends. Sporadische Überflutungen nach starken Regenfällen können zu Mischungsprozessen und zur Entstehung ephemerer Seen ohne Zufluss führen. Verdunstung ohne Zufluss und Mischungsprozesse können mithilfe von 3-Sauerstoffisotopenanalysen identifiziert werden. Die Möglichkeit episodischer Mischungsprozesse, zum Beispiel durch häufige Überflutungsereignisse, sollte bei der Paläo-Anwendung berücksichtigt werden.

Die zweite Studie präsentiert erste Ergebnisse von Isotopenanalysen von strukturell gebundenem Gipswasser aus lakustrinen Ablagerungen in der Atacama Wüste. Die Isotopenzusammensetzungen der analysierten Proben fallen auf charakteristische Verdunstungstrends, die auf die Erhaltung des primären Isotopensignals des Paläoseewassers hinweisen. Das *Craig-Gordon-Modell* wurde zusammen mit einer Monte-Carlo-Simulation verwendet, um die relative

Luftfeuchtigkeit zu bestimmen, die die Isotopendaten sowohl im d-excess vs. $\delta^{18}O$ Diagramm als auch im ^{17}O-excess vs. $\delta^{18}O$ Diagramm am besten widerspiegelt. Die Luftfeuchte, die das Modell ausgibt, wird nur minimal durch Änderungen der Isotopenzusammensetzung des Zuflusses und des atmosphärischen Dampfes beeinflusst. Sie kann jedoch stark vom gewählten windbedingten Turbulenzkoeffizienten und den Beschränkungen des Verdunstung-zu-Zufluss-Verhältnisses (E/I) abhängen. Die Modellierung liefert sinnvolle Luftfeuchtigkeitswerte, wenn die Modelleingangsparameter für die jeweiligen Standorte plausibel begrenzt werden. Die Ergebnisse deuten darauf hin, dass in der nördlichen Atacama Wüste vor etwa 3.5 Millionen Jahren feuchtere Bedingungen vorherrschten. Die Feuchtphase wurde möglicherweise begünstigt durch permanente El-Niño-ähnliche Bedingungen in der Wärmeperiode im frühen Pliozän (4.5 – 3.0 Ma).

Die dritte Studie befasst sich mit der Bodenbildung und sekundären Umverteilungs- und Transformationsprozesse von Evaporiten in Böden der Atacama-Wüste. Ein besseres Verständnis dieser Prozesse ist von entscheidender Bedeutung für die Interpretation der Isotopenzusammensetzung des strukturell gebundenen Gipswassers in pedogenen Ablagerungen. Für diese Studie wurden dünne Oberflächenkrusten, pulvriges Oberflächenmaterial und Konkretionen aus bis zu 40 cm Tiefe entlang mehrerer latitudinaler Transekte zwischen 19.5–25°S und 68.5–70.5°W beprobt. Die Ergebnisse dieser Studie zeigen, dass langfristige Ariditätsgradienten, Quellen und sekundäre Mobilisierungsprozesse die räumliche Verteilung von leicht löslichen Salzen – Chloriden und Nitraten – sowie Gips und Anhydrit in Böden der Atacama Wüste bestimmen. Die Hyperaridität ist zwischen 19-22°S am beständigsten. Außergewöhnlich hohe Chloridgehalte unterhalb der atmosphärischen Temperaturinversionsschicht (< 1200 m), sowie Na/Cl-Verhältnisse von 0.83 – ähnlich dem globalen Meerwasserverhältnis von 0.86 – lassen auf Gischt als primäre Quelle für Halit schließen. Grundsätzlich sind Gips und Anhydrit die häufigsten Minerale in den Böden der Atacama-Wüste. Das Vorkommen von Anhydriten zusammen mit hohen Chlorid- und Nitratgehalten deutet darauf hin, dass Anhydrit ein Sekundärprodukt von Auflösungs- und Fällungsreaktionen in stark salzhaltigen Lösungen ist.

Diese Arbeit erweitert das Wissen über Prozesse, die die Isotopenzusammensetzung von strukturell gebundenem Wasser aus lakustrinem und pedogenem Gips kontrollieren. Die Ergebnisse tragen zur Entwicklung eines leistungsfähigen Isotopenwerkzeugs bei, welches eine quantitative Rekonstruktion vergangener klimatischer Zustände in der Atacama Wüste ermöglicht.

Acknowledgements

First of all, I would like to express my sincere gratitude to my supervisor Prof. Dr. Michael Staubwasser for the continuous support during my PhD study and the opportunity to participate in several field campaigns. He fostered my scientific skills with insightful comments and critical feedback. I have greatly benefited from his enthusiasm and sharp thoughts on broad scientific topics.

I am particularly grateful to Dr. Daniel Herwartz without whom I would not have made it through my PhD studies. He always shows excitement for various scientific topics and never gave up overcoming the difficult problems one after another. He always supported me during my studies with fruitful discussions and gave me great motivation. He helped me to look at this research in different ways and to open my mind for new approaches.

I am glad and thankful to Dr. Oliver Bödeker for insightful suggestions, fruitful scientific exchange and discussions. Many thanks also go to Prof. Dr. Andreas Pack for being my second supervisor and Prof. Dr. Sandro Jahn for taking the chair of my examination committee.

I would like to acknowledge our Chilean colleagues Prof. Eduardo Campos, Prof. Guillermo Chong and Prof. Cristina Dorador for support with administrative issues, for collaborative field work and for sharing their comprehensive scientific knowledge about the Atacama Desert.

For financial support during my PhD, I would like to thank the University of Cologne and the CRC 1211 "Earth-Evolution at the Dry limit". Furthermore, I am thankful to the Graduate School of Geoscience (GSGS) for financial support of international conferences.

Furthermore, I would like to thank all the colleagues from the institute and from the CRC 1211 for their support and friendship during the past three years. Particularly, I would like to thank my office mates Jakub and Swea, who have supported me and had to put up with my stresses and moans for the past three years. They gave me constructive comments and warm encouragement during every stage of my PhD. A special thanks goes to our student helpers Chiara and Niklas for doing all the chemical analyses in the lab. Incredible thank goes to our technicians Jochen Scheld and Andreas Vogt, who have always supported and encouraged me. You helped me in whatever I asked you for, thanks a lot! Finally, my deepest gratitude goes to Christina Obert and Benedikt Ritter for all the support they gave me during my PhD studies. I was most fortunate to have their company, assistance, and encouragement.

Table of Contents

1 Introduction

Water is one of the most important components on Earth. It sustains life, is a critical part in weather processes and defines much of natural climate variability. Processes such as evaporation, condensation, precipitation, infiltration and runoff continually cycle water from oceans to the atmosphere to land and back to the ocean and thereby maintain water and energy balance between Earth's subsystems – the hydrosphere, the atmosphere, the lithosphere and the biosphere (Trenberth et al., 2009; Berner and Berner, 2012). Understanding if and how the hydrological cycle responses to climate change is fundamental to understand how Earth works, but also of increasing importance for environmental policy. Global warming, as it is induced by human activity in modern times, influences the spatial distribution of water on Earth leading to regional changes in precipitation, aridification of vast areas, and a more frequent occurrence of extreme weather events.

In response to changes in water availability, fundamental changes occur in both biological activity and Earth surface processes. The relationship between biological and landscape evolution is interdisciplinary studied within the CRC 1211 "Earth – Evolution at the Dry Limit". The project focusses on arid to hyperarid environments, where both biological activity and Earth surface processes are predominantly limited to the persistence and temporal occurrence of water. Long-term hyperarid conditions lead to isolation of species and fossilization of landscapes. On the other hand, biological activity becomes increasingly important with increasing water availability – eventually dominating soil formation and influencing geomorphologic processes. Even short episodes of increased water availability can leave long-lasting traces on Earth's surface.

Understanding processes that influence the temporal and spatial occurrence of water is of central interest for understanding life and Earth surface processes under hyperarid conditions. The scientific focus of this thesis lies on the Atacama Desert in northern Chile, which is characterized by pronounced aridity for at least several million years (Alpers and Brimhall, 1988; Hartley and Chong, 2002; Dunai et al., 2005; Rech et al., 2006; Evenstar et al., 2009, 2017; Jordan et al., 2014; Ritter et al., 2018b). In the hyperarid core, mean annual precipitation amounts are lower than 2 $mm \cdot a^{-1}$ with decades of absolute drought (Houston, 2006). However, coastal areas still sporadically receive moisture by fog, which can penetrate inland through topographic corridors but is restricted to elevations below 1200 m by a temperature inversion layer (Cereceda et al., 2002,

2008). Groundwater-supplied salt lakes, so called 'salars', and a few rivers display the only surface water occurrence. Groundwater originates by precipitation from deep headwaters in the Precordillera and the Western Cordillera. Additionally, sporadic precipitation events can cause extensive surface runoff along the western slopes of the Andes.

The aridity in the Atacama Desert is primarily caused by subtropical subsidence of warm and dry air masses induced by the Hadley circulation and upwelling of cold-water masses of the coast-parallel Humboldt Current along the west coast of South America (Houston and Hartley, 2003). This upwelling leads to the formation of a temperature inversion layer preventing moisture uptake and transport to the Atacama Desert. Aridity is further intensified by the rain shadow effect of the Andes to the east lowering potential precipitation from Atlantic air masses (Hartley et al., 2005). The virtual absence of water in the Atacama Desert makes it to an ideal environment to investigate forcing and feedback mechanisms of aridity as well as impacts of short humid periods on surface processes and biological activity.

Understanding and reconstructing the state, amount and impact of past water availability is of central interest for studying the relationship between the water cycle and climate. Stable hydrogen and oxygen isotopes of water have been proven as a powerful tool to trace hydrological processes providing information on the spatial distribution of water and water availability in general. Knowledge of fundamental processes governing the general hydrologic balance of water reservoirs is essential to unravel key driving mechanisms of past climate changes.

Different hydrological reservoirs – oceans, precipitation, fog, dew, groundwater, rivers, and lakes – have distinct isotopic compositions. These differences are caused by fractionation processes that accompany solid-liquid-vapor phase transitions, e.g. evaporation of surface waters or condensation in clouds (Dansgaard, 1964). Evaporation is a crucial component in the extremely arid environment of the Atacama Desert. Large isotope effects that are associated with evaporation are mainly controlled by the humidity in the atmosphere (Craig and Gordon, 1965; Gonfiantini, 1986; Gat, 1996; Criss, 1999; Horita et al., 2008). Recent studies demonstrated that isotope analyses of lake water in arid environments can provide quantitative information on humidity during evaporation (Surma et al., 2015, 2018). Thus, isotope analyses of evaporated paleo-waters can serve as a useful tool to reconstruct past changes in the atmospheric moisture content and, thus, water availability in the Atacama Desert.

Although water of the geologic past is barely available directly for isotopic analysis, they are widely present as structurally bonded water in evaporite salts. Gypsum ($CaSO_4 \cdot 2H_2O$), for example, is a hydrated mineral that precipitates in lakes due to concentration of solutes by evaporation and preserves the isotopic composition of ambient lake water in its crystal lattice (Khademi et al., 1997; Farpoor et al., 2004; Evans et al., 2015; Herwartz et al., 2017; Gázquez et al., 2018). First applications of isotope analyses of structurally bonded water of gypsum focused on the understanding of gypsum sources and climatic conditions during gypsum formation (Matsubaya and Sakai, 1973; Sofer, 1978; Hałas and Krouse, 1982; Khademi et al., 1997). Recent studies investigated their potential for paleoclimate reconstruction (Hodell et al., 2012; Palacio et al., 2014; Herwartz et al., 2017; Gázquez et al., 2018). A recent study by Gázquez et al. (2018) demonstrated that combining hydrogen and triple oxygen isotope analyses of structurally bonded water of gypsum can serve as a powerful tool to quantitatively reconstruct past changes in atmospheric relative humidity. Thus, application of this method to lacustrine gypsum deposits in the Atacama Desert may provide quantitative information on phases of increased or decreased water availability in the geological past and ultimately contribute to an improved understanding of the climate evolution to the recent hyperarid state of the Atacama Desert.

2 Climate evolution of the Atacama Desert

The Atacama Desert – one of the driest regions on Earth – extends from southern Peru to northern Chile along the west coast of South America. It is bounded to the east by the high Andes and restricted to the west by the Pacific Ocean. Running from west to east the major N-S trending topographic units are the Coastal Cordillera, the Central Depression, the Precordillera and the high Andes (Fig. 2.1). The high Andes encompass the Western and the Eastern Cordillera framing the high-altitude Altiplano-Puna plateau. Although there are regional climatic differences, arid conditions prevail throughout the Atacama Desert. A hyperarid core with < 2 $mm \cdot a^{-1}$ precipitation is centered in the Coastal Cordillera and at the western margin of the Central Depression between 19°S and 22°S (Houston, 2006; Ritter et al., 2018b). Aridity decreases with increasing altitude along the western slopes of the Precordillera over the Western Cordillera (up to 6000 m) and the Altiplano-Puna Plateau (~4000 m) receiving moisture mainly from Atlantic air masses. Increasing precipitation to the south (south of 23.5°S) is attributed to the frequent occurrence of storm events. Furthermore, a narrow band along the coast receives regularly moisture by fog (Cereceda et al., 2002, 2008). Fog, also called 'camanchaca', forms mainly during night with more and longer fog events occurring in austral winter (June-September) (Schween et al., 2020). The 'fog zone' is restricted by the oceanic boundary layer to elevations < 1200 m as indicated by cloud height data of stratocumulus clouds at the coast and the presence of *Tillandsia sp.* vegetation (Cereceda et al., 2008). The highest frequency of fog events is observed in the central area of the Atacama Desert, where fog can penetrate further inland along the Rio Loa canyon (Schween et al., 2020). Rarely, fog can reach the slopes of the Andes (Schween et al., 2020).

The primary cause for the prevalence of arid conditions in the Atacama Desert is its position within the subtropical high-pressure belt (Hartley et al., 2005), where the Hadley circulation induces the subsidence of warm and dry air masses. Furthermore, the upwelling of the cold Humboldt Current leads to the formation of a temperature inversion layer over the Pacific Ocean that inhibits moisture uptake and transport from the Pacific Ocean across the Coastal Cordillera (Hartley and Chong, 2002). The aridity is further intensified by the rain shadow effect of the high Andes to the east (Hartley and Chong, 2002; Houston and Hartley, 2003). Thus, the driving forces for recent aridity might be identified, however, the onset of hyperaridity and the climate evolution of the Atacama Desert are still a matter of debate (Evenstar et al., 2017 and references therein).

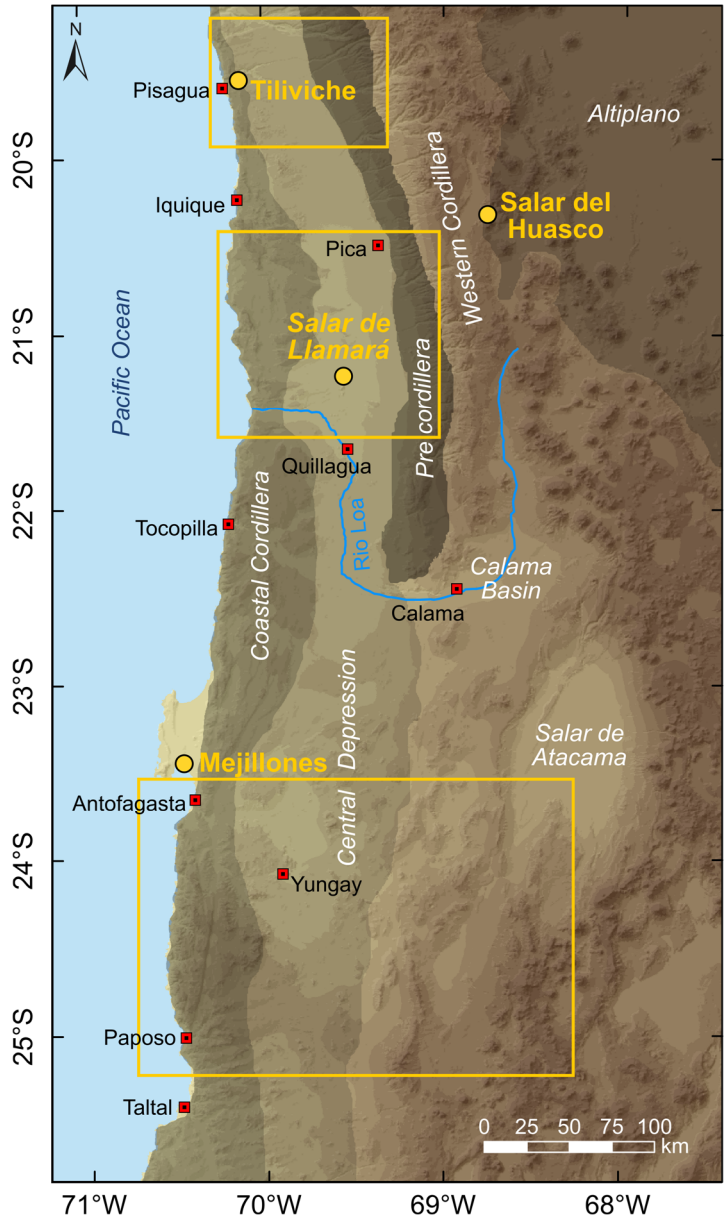

Figure 2.1: Color-shaded digital elevation model of west-central South America (derived from SRTM data, created using ArcGIS 10.5.1) showing the major morphotectonic units of the Atacama Desert and the Andes. Yellow circles and frames indicate areas that are subject of this thesis.

The latitudinal position of the South American plate is static since at least 150 Ma pointing to prevailing semiarid to arid climate conditions since the late Jurassic (Hartley et al., 2005). Deep opening of the Drake Passage and the establishment of the Antarctic Circumpolar Current about 30 Ma ago initiated the Humboldt Current, which promotes climate stability and aridification of western South America (e.g. Barker and Burrell, 1977; Pfuhl and McCave, 2005; Scher et al., 2015). The Andean orogeny started during the Cretaceous with the reactivation of the Nazca-South American plate subduction system (Haschke et al., 2002). The magmatic arc that was initially located in the present-day Coastal Cordillera, progressively migrated eastwards resulting in the

establishment of the present arc in the Western Cordillera since the Miocene (Haschke et al., 2002). Significant uplift of the Altiplano-Puna region occurred in the Mid-Miocene (Mortimer, 1973; Gregory-Wodzicki, 2000; Wörner et al., 2002; Hartley, 2003; Hartley et al., 2005). Investigations of supergene copper ore deposits suggest that this period of extensive uplift of the Andes initiated hyperaridity in the Atacama Desert (Alpers and Brimhall, 1988; Sillitoe and McKee, 1996). Several studies of cosmogenic nuclide exposure ages, relict geomorphic landforms, and paleosol chemistry support a dominantly hyperarid climate since the middle Miocene (Hoke et al., 2004; Nishiizumi et al., 2005; Rech et al., 2006; Jordan et al., 2014). However, other studies suggest that global climate cooling after the Mid-Miocene climatic optimum rather than the uplift of the Andes led to the establishment of hyperarid conditions in the Atacama Desert (Hartley and Chong, 2002; Hartley, 2003; Lamb and Davis, 2003). Oldest surface exposure ages derived from cosmogenic nuclide analyses date back to 34 Ma indicating dominantly hyperarid climate since the Oligocene (Dunai et al., 2005; Ritter et al., 2018b). Hyperaridity was episodically interrupted by short-lived phases of more humid (but still arid) conditions driven by paleoclimate changes (Sáez et al., 1999, 2012; Evenstar et al., 2009, 2017; Placzek et al., 2010; Jordan et al., 2014; Ritter et al., 2018b, 2018a). Several pluvial phases occurred in late Pleistocene and Holocene times as suggested by radiocarbon analyses of plant macrofossils and rodent midden records (Latorre et al., 2006; Nester et al., 2007; Gayo et al., 2012). These pluvial phases can be related to periods of increased ENSO activity and glacial retreat in Antarctica and Patagonia (Latorre et al., 2006; Nester et al., 2007; Gayo et al., 2012). La Niña-like conditions reflect periods of pronounced sea surface temperature gradients in the tropical Pacific and higher latitudes, which lead to a southward displacement and intensification of the Bolivian High and strengthening of easterly winds (Vuille et al., 2000; Gayo et al., 2012). Corresponding moisture fluxes from Atlantic and Amazonian sources lead to increased precipitation in the Andes and intensified surface runoff along the western slopes of the Precordillera and distal parts in the Central Depression (Betancourt et al., 2000; Bobst et al., 2001; Garreaud et al., 2003). In contrast, during El Niño-like conditions, moisture transport along the west coast of South America is increased due to meltwater injections during Antarctic and Patagonian ice sheet retreat and weakening of the Humboldt Current that go along with warmer sea surface temperatures in the eastern Pacific Ocean and weakening of the subtropical Anticyclone (Dekens et al., 2007; Garreaud et al., 2010). Furthermore, marine archives indicate that in areas south of 23°S more humid conditions during glacials may be caused by northward migrating South Pacific cut-off low systems (Lamy et al., 1998, 2000; Stuut and Lamy, 2004; Rojas et al., 2009).

The chronology of the Atacama Desert is extensively studied, however, as recently shown by Ritter et al. (2018b), temporal and spatial differences of the climate evolution within the Atacama Desert is far more complex and need further analysis. Stratigraphic and sedimentological studies often do not provide unique information on past climate changes but are rather dependent on the tectonic stability of the catchment. Aridity can vary on a local scale for topographic or tectonic reasons. Even gentle tectonic movements could result in changes in the hydrological balance and trigger variations in the depositional record (Sáez et al., 1999). Moreover, as wetter conditions in the Precordillera and the Andes can cause extensive surface runoff to the Central Depression, investigated archives in the present hyperarid core may reflect paleoclimate conditions in high-altitude regions rather than local variations in aridity. Sedimentary archives that reflect a local, autochthonous climate signal in the Atacama Desert are principally rare.

The overarching goal of the project, in which this thesis embedded, is the development of a new tool that can provide quantitative paleoclimatic information on a local scale independent from tectonic movements in the catchment. The method is based on stable isotope analyses of water structurally bonded in gypsum. Gypsum ($CaSO_4 \cdot 2H_2O$) is one of the most common evaporites in the Atacama Desert formed by precipitation from calcium sulfate-saturated solution due to evaporation either in lakes (lacustrine gypsum) or in soils (pedogenic gypsum). In principal, the isotopic composition of structurally bonded water of gypsum reflects the isotopic composition of ambient water during gypsum formation that provides quantitative information on environmental conditions and hydrological parameters at the time of gypsum precipitation. Within the framework of this thesis, we aim to improve the understanding of triple oxygen isotope systematics of structurally bonded water of lacustrine gypsum and test its potential to quantify paleo-humidity and other climatic variables (e.g. temperature). With the success of the method and improvements in direct dating techniques of gypsum, we can quantitatively reconstruct past climate changes in the Atacama Desert and compare different pluvial and arid phases of Atacama's climate history.

3 Stable oxygen and hydrogen isotopes in the water cycle

The water cycle describes the continuous movement of water on Earth's surface and in the atmosphere. The main driving factors are evaporation, condensation and precipitation. However, the water cycle is much more complex and still not fully understood. The ocean, which constitutes about 97 % of the hydrosphere, is the ultimate source for atmospheric vapor and all meteoric waters. Water evaporates from the ocean, condenses in the atmosphere, forms clouds, and precipitates in the form of rain or snow directly over the ocean or after transport over continents. On land, water resides in ice caps, glaciers, lakes, rivers, soils and groundwater systems. A large fraction of continental water returns to the atmosphere via evaporation and evapotranspiration from surface waters and plants. As a final point, to close the cycle, the water flows back into the ocean via rivers, groundwater and surface runoff, where it will evaporate once again.

Variations in stable isotope ratios of natural waters are known since more than 70 years. The pioneering work of Epstein and Mayeda (1953), who analyzed oxygen isotope ratios of marine and fresh waters and Friedman (1953), who precisely determined respective hydrogen isotope ratios, set the cornerstone to understand variations in isotopic compositions of different natural waters and their interrelationship. A linear correlation between oxygen and hydrogen isotope ratios in meteoric waters – known as the Global Meteoric Water Line – was first described by Craig (1961). These early foundations were summarized on a quantitative basis by Dansgaard (1964).

Nowadays, stable isotope measurements are a powerful tool with an extremely wide range of applications. Stable isotope analyses of natural waters allow the identification of and differentiation between different water reservoirs and the tracing of processes that modify them. Furthermore, isotope studies of various proxy materials such as ice cores, lake and ocean sediments, shells, and plant material have demonstrated its suitability for paleoclimate reconstructions.

3.1 Basic principles

In general, abundances of heavy isotopes in natural terrestrial materials are low and natural variations in absolute isotope ratios are small. Since relative differences can be determined more precisely, the δ-notation was introduced to report isotopic data (McKinney et al., 1950):

$$\delta\,(‰) = \left(\frac{R_{smp}}{R_{std}} - 1\right) \cdot 1000 \tag{3.1}$$

where R is the absolute ratio of the rare (heavy) to the abundant (light) isotope (e.g. $^{2}H/^{1}H$, $^{18}O/^{16}O$, $^{17}O/^{16}O$) in the sample (smp) and the standard reference material (std) resulting in respective δ values (e.g. $\delta^{2}H$, $\delta^{17}O$, $\delta^{18}O$). Hydrogen and oxygen isotope ratios in water are usually reported relative to Vienna Standard Mean Ocean Water (VSMOW) – an artificial mixture representative for the average isotopic composition of ocean water that is provided by the IAEA Isotope Hydrology Laboratory (Vienna). By definition, the $\delta^{2}H$, $\delta^{17}O$, and $\delta^{18}O$ values of VSMOW are 0 ‰.

Isotopes are separated during phase transitions or isotope exchange reactions. The isotopic fractionation factor $\alpha_{A\text{-}B}$ between two phases A and B is defined as:

$$\alpha_{A-B} = \frac{R_A}{R_B} = \frac{1000+\delta_A}{1000+\delta_B} \tag{3.2}$$

Two main types of isotope fractionation can be distinguished. Equilibrium isotope fractionation is associated with bidirectional (reversible) processes. The fractionation factor decreases with increasing temperature. Equilibrium fractionation factors for $^{2}H/^{1}H$ and $^{18}O/^{16}O$ between liquid water and water vapor are well established. Throughout this thesis, the definition of Horita and Wessolowski (1994) is used:

$$\ln {}^{2}\alpha_{eq,\,l-v} = 1158.8 \cdot 10^{-12}\,T^{3} - 1620.1 \cdot 10^{-9}\,T^{2} + 794.84 \cdot 10^{-6}\,T - 0.16104 + 2.9992 \cdot 10^{6}\,T^{-3} \tag{3.3a}$$

$$\ln {}^{18}\alpha_{eq,\,l-v} = -0.007685 + 6.7123\,T^{-1} - 1.6664 \cdot 10^{3}\,T^{-2} + 0.35041 \cdot 10^{6}\,T^{-3} \tag{3.3b}$$

For room temperature conditions (20°C), this results in $^{2}\alpha_{eq,\,l\text{-}v} = 1.0836$ and $^{18}\alpha_{eq,\,l\text{-}v} = 1.0097$.

Diffusive isotope fractionation normally accompanies irreversible incomplete, or unidirectional processes such as evaporation, diffusion and dissociation reactions. In principle, kinetic isotope effects can be explained by different translational velocities of different isotopic forms of molecules within a phase or during phase transition (Sharp, 2017). The isotope fractionation factor of vapor diffusion in air can be estimated from the kinetic theory of gases (Merlivat, 1978):

$$\alpha_{diff,\,l-v} = \frac{D_x}{D_a} = \left(\frac{M_a}{M_x} \cdot \frac{M_x+M_G}{M_a+M_G}\right)^{1/2} \left(\frac{\Gamma_a+\Gamma_G}{\Gamma_x+\Gamma_G}\right)^{2} \tag{3.4}$$

where D is the molecular diffusivity, M is the molecular mass, Γ is the molecular collision diameter, and the subscripts x, a, and G refer to the rare isotopologues (e.g. $^{2}H^{1}H^{16}O$, $^{1}H_{2}{}^{17}O$, $^{1}H_{2}{}^{18}O$), the

abundant isotopologues ($^1H_2{}^{16}O$), and the gas in which diffusion occurs (air, N_2). Respective fractionation factors for $^2H^1H^{16}O/^1H_2{}^{16}O$ and $^1H_2{}^{18}O/^1H_2{}^{16}O$ derived from gas kinetic theory are $^2\alpha_{diff,\,l\text{-}v} = 1.0166$ and $^{18}\alpha_{diff,\,l\text{-}v} = 1.0324$. These values are slightly different from the values experimentally determined by Merlivat (1978), which are $^2\alpha_{diff,\,l\text{-}v} = 1.0251$ and $^{18}\alpha_{diff,\,l\text{-}v} = 1.0285$, where the latter is in good agreement with that determined by Barkan and Luz (2007). The discrepancy between values derived experimentally and from theory is not well known but may be related to the different behavior of water isotopologues interacting with N_2 and O_2 molecules in air (Gonfiantini et al., 2018). Throughout this thesis, diffusive fractionation factors of Merlivat (1978) were used.

Craig (1961) observed that δ^2H and $\delta^{18}O$ values of globally distributed meteoric waters are linearly related by:

$$\delta^2H = 8 \cdot \delta^{18}O + 10 \tag{3.5}$$

This relationship has become known as the Global Meteoric Water Line (GMWL). The slope of the GMWL is related to equilibrium fractionation of hydrogen and oxygen isotopes that accompanies cloud condensation processes. The intercept is caused by diffusive isotope effects that are associated with evaporation of oceanic water into unsaturated air.

Large deviations from the slope of the GMWL are caused by kinetic effects, which are associated with evaporation of surface waters. Evaporation drives the remaining water to higher δ^2H and $\delta^{18}O$ values but progresses along shallower slopes. To quantify these departures, the d-excess parameter was introduced (Craig, 1961):

$$d - excess = \delta^2H - 8 \cdot \delta^{18}O \tag{3.6}$$

While evaporation shifts the remaining water below the GMWL – and thus to lower d-excess values – the vapor evolves complementary tending to lower δ^2H and $\delta^{18}O$, and higher d-excess values. As condensation is generally considered to be an equilibrium process, precipitation has d-excess values similar to atmospheric vapor. Spatial variations in the isotopic composition of atmospheric vapor and precipitation are related to different source regions, temperature differences, humidity and evapotranspiration (Sharp, 2017).

3.2 The triple oxygen isotope system

For a long time, it was thought that, due to mass dependence principles, the analyses of the rare ^{17}O isotope provides no additional information to the widely used $^{18}O/^{16}O$ isotope ratio. Recent advances in high-precision mass spectrometry unveiled small variations in the relationship between $^{17}O/^{16}O$ and $^{18}O/^{16}O$ isotope ratios in different fractionation processes (Barkan and Luz, 2005, 2007). This advance initiated detailed investigations of triple oxygen isotope compositions ($^{16}O/^{17}O/^{18}O$) of marine and meteoric waters, ice cores, rocks and plant materials aiming to refine their fractionation by evaporation, condensation, mixing, exchange reactions and other processes (e.g. Landais et al., 2006, 2008, 2010; Luz and Barkan, 2010; Surma et al., 2015, 2018; Gázquez et al., 2017; Alexandre et al., 2018, 2019).

The equilibrium and diffusive isotope fractionation factors of $^{17}O/^{16}O$ were precisely determined in laboratory experiments (Barkan and Luz, 2005, 2007). In triple isotope systems the fractionation factors are related by the exponent θ (e.g. Rozanski et al., 2001):

$$^{17}\alpha_{l-v} = {}^{18}\alpha_{l-v}{}^{\theta} \tag{3.7}$$

In the triple oxygen isotope system is $\theta_{eq} = 0.529$ for equilibrium fractionation (Barkan and Luz, 2005) and $\theta_{diff} = 0.5185$ for diffusive fractionation (Barkan and Luz, 2007). The respective fractionation factors are $^{17}\alpha_{eq,\,l\text{-}v} = 1.0051$ at 20°C and $^{17}\alpha_{diff,\,l\text{-}v} = 1.0146$.

As in the classic δ^2H-$\delta^{18}O$ system, $\delta^{17}O$ and $\delta^{18}O$ of globally distributed meteoric waters are linearly correlated (Luz and Barkan, 2010):

$$\delta'^{17}O = 0.528 \cdot \delta'^{18}O + 0.000033 \tag{3.8}$$

where $\delta'^{x}O = 1000 \cdot \ln(\delta^{x}O/1000 + 1)$ and x refers to 17 or 18, respectively. Deviations from that Global Meteoric Water Line can be quantified by the ^{17}O-excess parameter (Luz and Barkan, 2010):

$$^{17}O - \text{excess} = \delta'^{17}O - 0.528 \cdot \delta'^{18}O \tag{3.9}$$

Variations in ^{17}O-excess for mass dependent processes are very small and therefore usually reported as per meg (i.e. ‰/1000). Note that the ^{17}O-excess value of sea water is slightly negative (-5 per meg) (Luz and Barkan, 2010).

3.3 Evaporation

Evaporation is a fundamental process in the hydrologic cycle occurring in various reservoirs including open-surface water bodies like oceans, lakes and rivers, but also clouds, soils, and plants. Thus, knowledge of the isotope effects associated with evaporation is essential for a comprehensive understanding of isotope variations in the hydrologic cycle.

Evaporation of water is accompanied by large isotope effects, where light isotopes preferentially pass into the vapor phase and the residual liquid phase becomes enriched in heavier isotopes. These isotope effects were systematically described in a conceptual model developed by Craig and Gordon (Craig and Gordon, 1965). The isotopic composition of an evaporating water body depends on a number of factors with the main driving forces being the relative humidity, the isotopic composition of atmospheric vapor and initial / inflowing water (Craig and Gordon, 1965). Over the decades, the Craig-Gordon isotopic evaporation model (C-G model) became fundamental for isotopic studies in the hydrological cycle (e.g. Gonfiantini, 1986; Gat, 1996; Horita et al., 2008; Gonfiantini et al., 2018).

The C-G model considers discrete layers that are characterized by specific transport mechanisms allowing to quantify the overall isotope fractionation using a series of relatively simple equations. The model is schematically illustrated in Fig. 3.1 and described in detail in the following.

Three distinct processes contribute to the overall isotope fractionation associated with evaporation. First, a layer of saturated air (h = 100 %) forms in isotopic equilibrium with the water directly above the water surface (Gonfiantini et al., 2018):

$$\frac{R_W}{R_{eq}} = \alpha_{eq,\,W-eq} \tag{3.10}$$

where R_W is the isotopic composition of the liquid phase, R_{eq} is the isotopic composition of vapor in the 'equilibrium layer' and $\alpha_{eq,\,W\text{-}eq}$ is the equilibrium fractionation factor between the liquid and the vapor phase of water.

Second, the vapor escapes from this saturated layer by either molecular or turbulent diffusion (Gonfiantini et al., 2018):

$$\frac{R_{eq}}{R_{esc}} = \alpha_{diff,\,eq-esc}^{n} \tag{3.11}$$

where R_{esc} describes the isotopic composition of the escaping vapor, $\alpha_{diff,\,eq\text{-}esc}$ is the diffusive fractionation factor for molecular diffusion and n is the turbulence index. In a calm environment,

isotope fractionation is only controlled by molecular diffusion and n = 1. In a totally turbulent atmosphere, no isotope fractionation occurs and, thus, n = 0. If the laminar layer is discontinuous, isotope fractionation is controlled by both molecular and turbulent diffusion and can be described by values of 0 < n < 1.

Finally, the vapor in the free atmosphere re-equilibrates with the liquid water surface by back-diffusion (Gonfiantini et al., 2018):

$$\frac{R_V}{R_{cap}} = \alpha^{n}_{diff,\,V-cap} \tag{3.12}$$

where R_V is the isotopic composition of vapor in the free atmosphere, R_{cap} is the isotopic composition of the water captured by the liquid water surface and $\alpha_{diff,\,V\text{-}cap}$ describes the isotopic fractionation between both phases in dependence on the stability of the laminar layer (n).

The overall isotope fractionation during evaporation between the liquid phase R_W and the evaporated water R_E can be quantified by (Barkan and Luz, 2007):

$$\alpha_{evap} = \frac{R_W}{R_E} = \frac{\alpha^{n}_{diff} \cdot \alpha_{eq} \cdot (1 - h)}{1 - \alpha_{eq} \cdot h \cdot (R_V/R_W)} \tag{3.13}$$

where the subscripts W, E, and V denote the isotopic composition of the liquid water, the evaporating vapor and the atmospheric vapor and h refers to the relative humidity in the free atmosphere. In general, the total isotope fractionation during evaporation increases with decreasing relative humidity (Fig. 3.2).

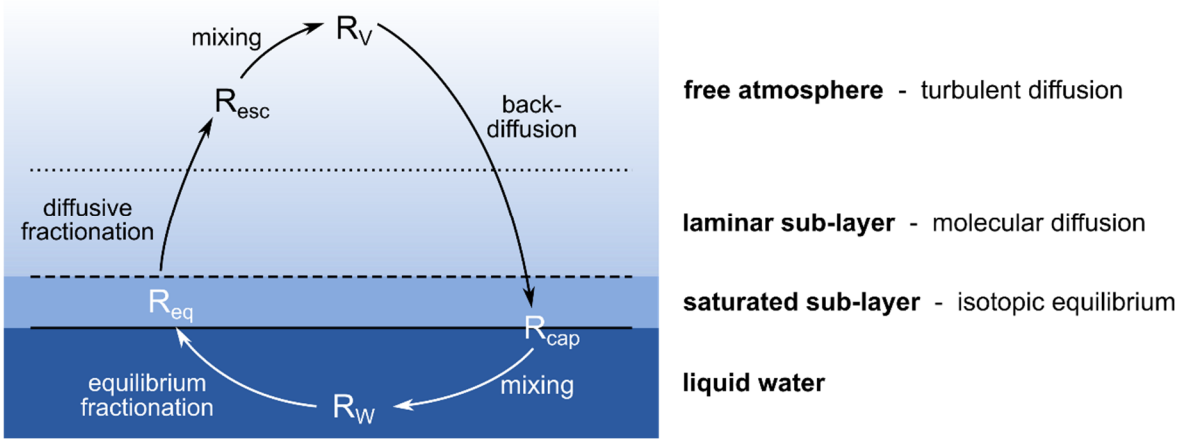

Figure 3.1: Schematic illustration of the Craig-Gordon model. The Craig-Gordon model separates the atmosphere in discrete layers – a water vapor-saturated sub-layer, a laminar sub-layer, and a turbulent sub-layer – to describe isotope effects associated with evaporation of liquid water. The driving processes are equilibrium and diffusive fractionation during evaporation as well as isotopic exchange between atmospheric vapor and liquid water via back-diffusion.

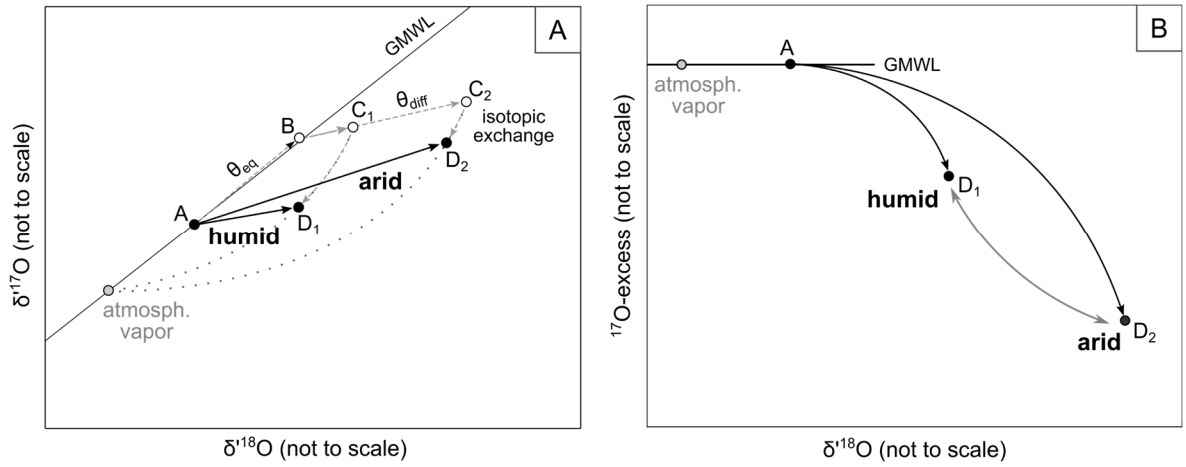

Figure 3.2: Schematic illustration of isotope effects on the residual water body during evaporation in $\delta^{17}O$ vs $\delta^{18}O$ (A) and ^{17}O-excess vs $\delta^{18}O$ (B) for low (arid) and high (humid) humidity (modified after Landais et al., 2006). Open circles represent conceptual intermediate states during the evaporation process. A: initial isotopic composition of the water body, A -> B: equilibrium fractionation, B -> C: diffusive fractionation, C -> D: isotopic exchange with air moisture, D: Isotopic composition of residual water. The proportion of diffusive fractionation and isotopic exchange depend on relative humidity.

Classically, δ^2H and $\delta^{18}O$ isotope analyses are used in combination with the C-G model to investigate lake system dynamics, to quantify water balances and to identify interactions between lake and groundwater (e.g. Rozanski et al., 2001 and references therein). Recent studies evaluated its potential to determine fundamental environmental variables like relative humidity and temperature (Gibson, 2002; Gibson and Reid, 2010, 2014; Gibson et al., 2016). However, a unique interpretation from δ^2H and $\delta^{18}O$ of evaporated waters alone is challenging, since the isotopic composition can be affected by several factors including temperature, salinity, mixing and exchange reactions as well as vital effects induced by biologic activity.

The novel $\delta^{17}O$-$\delta^{18}O$ system holds a great potential to add additional information to the classic δ^2H-$\delta^{18}O$ system. In principle, both isotope systems show similar trends during evaporation, but are differently sensitive to, e.g., temperature and salinity (e.g. Barkan and Luz, 2007; Surma et al., 2015, 2018). Together with the different equilibrium and diffusive isotope fractionation of hydrogen ($^2H/^1H$) and oxygen ($^{18}O/^{16}O$, $^{17}O/^{16}O$), the combination of hydrogen and triple oxygen isotope analysis of evaporated waters will help to improve the knowledge about isotope effects associated with evaporation.

3.4 Natural evaporation in non-recharged and recharged lake systems

Triple oxygen isotope systematics during evaporation for recharged and non-recharged surface water bodies were systematically investigated in arid environments by Surma et al. (2015, 2018).

The isotopic evolution of non-recharged water bodies during evaporation can be described by (Fig. 3.3; Criss, 1999; Gonfiantini et al., 2018):

$$R_W = f^B \cdot \left(R_{WI} - \frac{A}{B} \cdot R_V\right) + \frac{A}{B} \cdot R_V \tag{3.14}$$

where R_{WI} is the initial isotopic composition of the evaporating water, R_V is the isotopic composition of atmospheric vapor, and f is the fraction of residual water. The parameter A describes the isotopic fractionation associated with the escape of vapor from the liquid water surface through the equilibrium and the molecular diffusion layer, while the parameter B represents isotope fractionation associated with back-diffusion of vapor to the liquid water surface (Gonfiantini et al., 2018):

$$A = -\frac{h}{\alpha^n_{diff,\,l-v} \cdot (1-h)} \tag{3.15}$$

$$B = \frac{1}{\alpha_{eq,\,l-v} \cdot \alpha^n_{diff,\,l-v} \cdot (1-h)} - 1 \tag{3.16}$$

Both parameters depend on the relative humidity h of the atmosphere. During evaporation, the isotopic composition of the residual water R_W continuously tends to achieve isotopic stationary state, the so-called 'isotopic end value', which is denoted by R_{SS} (Criss, 1999; Gonfiantini et al., 2018):

$$R_{SS} = \frac{A}{B} \cdot R_V \tag{3.17}$$

Isotopic stationary state conditions can only be achieved for high relative humidity ($h \gtrsim 0.5$), where $B \geq 1$ (Gonfiantini et al., 2018). Note that the isotopic end value is independent of the isotopic composition of the initial water R_{WI}.

In the case of recharged water bodies, the evaporation-to-inflow ratio (E/I) must be considered (Fig. 3.3; Criss, 1999):

$$R_{WS} = \frac{\alpha_{eq,\,l-v} \cdot \alpha^n_{diff\ \ l-v} \cdot (1-h) \cdot R_{WI} + \alpha_{eq,\,l-v} \cdot h \cdot E/I \cdot R_V}{E/I + \alpha_{eq,\,l-v} \cdot \alpha^n_{diff,\,l-v} \cdot (1-h) \cdot (1-E/I)} \tag{3.18}$$

Here, R_{WI} refers to the isotopic composition of the inflowing water. Lake systems in steady state have $E/I \leq 1$, whereby in the special case of a terminal lake $E/I = 1$. E/I ratios higher than 1 indicate non-steady-state conditions, where the lake tends to desiccate.

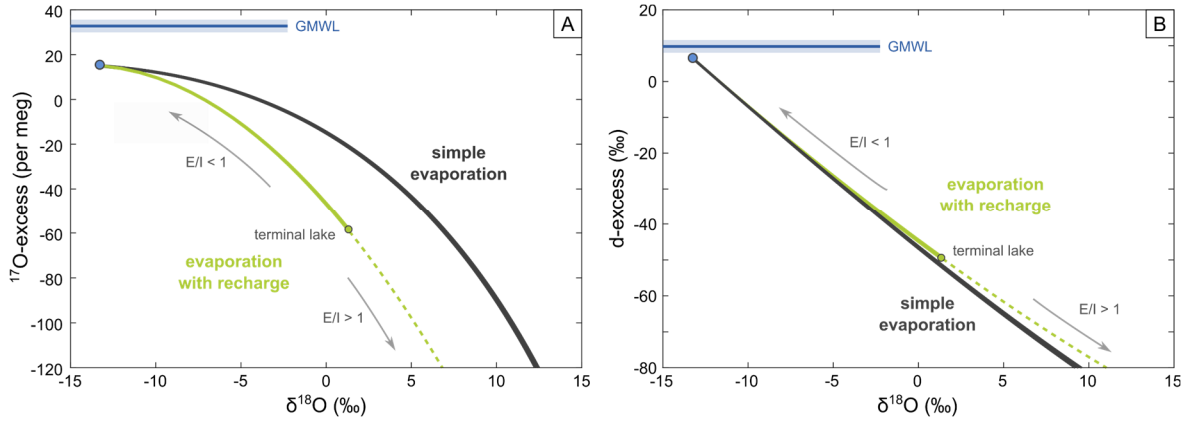

Figure 3.3: Comparison of evaporation trajectories for non-recharged (black) and recharged water bodies (green) in triple oxygen isotope space (A) and in the classic d-excess – $\delta^{18}O$ system (B). In the case of simple evaporation without recharge, evaporation continuously drives the isotopic composition of the residual water body to higher $\delta^{18}O$ and lower d-excess and ^{17}O-excess values. In recharged systems, continuous inflow of isotopically light water prevents a strong enrichment in $\delta^{18}O$ as it is observed for simple evaporation. The isotopic composition of recharged water bodies is controlled by the E/I ratio, where $E/I \leq 1$ represent steady-state conditions and in the case of $E/I > 1$, the water body tends to dry out. In a terminal lake the inflow is completely balanced by evaporation ($E/I = 1$).

For water bodies with high salt concentrations (> 30 $g \cdot l^{-1}$) salinity effects must be considered. The effect of salinity on the isotopic composition of evaporating waters is twofold.

(1) Ion hydration causes isotope fractionation between the free water and the water in the hydration shell that affects the activity ratio of the water body. This so-called salt effect can be corrected by $\alpha_{eq,\,l\text{-}v\_solution} = \Gamma \cdot \alpha_{eq,\,l\text{-}v\_pure\ water}$ (e.g. Sofer and Gat, 1975). The magnitude of the salt effect Γ depends on the ion concentration in the solution (Sofer and Gat, 1972, 1975; Horita, 1989, 2005; Koehler et al., 2013; Oerter et al., 2018). For naturally common sodium chloride solutions, the salt effect can be expressed as (Horita, 2005):

$$10^3 \ln \Gamma\,(^2H/^1H) = 2.2m\ NaCl + 2.5m\ KCl + 5.1m\ MgCl_2 + 6.1m\ CaCl_2 \quad (3.19a)$$

$$10^3 \ln \Gamma\,(^{18}O/^{16}O) = 0.16\ m\ KCl - 1.11m\ MgCl_2 - 0.47m\ CaCl_2 \quad (3.19b)$$

where m is the molality (mol/kg H_2O). In chloride-type brines, the salt effect on oxygen isotopes is negligible, but has a significant impact on hydrogen isotopes.

(2) An increasing salt content increases the viscosity of the solution that leads to a lowering of the vapor pressure above the fluid. This effect is accounted for using an effective humidity estimated from Raoult's law (Criss, 1999): $h_{eff} = h \cdot \rho_{solution}/\rho_{pure\ water}$, where $\rho_{solution}$ is the density of the brine solution and $\rho_{pure\ water}$ is the density of pure water (0.9982 $g \cdot cm^{-3}$ at 20°C).

3.5 Structurally bonded water of gypsum

Gypsum ($CaSO_4 \cdot 2H_2O$) is a hydrated mineral that comprises up to 20.9 wt-% structurally bonded water in its crystal lattice. In arid environments, gypsum can form by precipitation in lakes due to concentration of ions in the solution by evaporation. Thereby, it captures the isotopic composition of ambient evaporitic water in its crystal lattice, which can be preserved over tens of millions of years (Khademi et al., 1997; Farpoor et al., 2004; Evans et al., 2015; Gázquez et al., 2018). Several studies demonstrated that the isotopic composition of structurally bonded water of gypsum provides information on environmental conditions during gypsum formation (Matsubaya and Sakai, 1973; Sofer, 1978; Hałas and Krouse, 1982; Khademi et al., 1997; Farpoor et al., 2004; Evans et al., 2015, 2018; Herwartz et al., 2017; J. Li et al., 2017; Gázquez et al., 2018).

As recently shown, the combined analyses of hydrogen and triple oxygen isotopes of structurally bonded water of gypsum can serve as a useful tool to reconstruct paleo-humidity conditions (Gázquez et al., 2018).

Formation of gypsum occurs either by direct precipitation due to evaporation, hydration of anhydrite or oxidation of sulfides (Murray, 1964; Sofer, 1978). The equilibrium fractionation factor between structurally bonded water (SBW) of gypsum and ambient water (AW) during gypsum formation is defined as:

$$\alpha_{\mathrm{SBW-AW}} = \frac{1000 + \delta_{\mathrm{SBW}}}{1000 + \delta_{\mathrm{AW}}} \tag{3.20}$$

Accurate knowledge of the fractionation factors for ^{2}H, ^{17}O, and ^{18}O is fundamental to reconstruct the isotopic composition of the mother solution. Therefore, several studies applied different techniques to determine respective equilibrium fractionation factors, including (1) hydration of anhydrite, (2) evaporation of solution saturated in $CaSO_4$, and (3) mixing of $CaCl_2$ and Na_2SO_4 solutions (Baertschi, 1953; Gonfiantini and Fontes, 1963; Matsubaya, 1971; Sofer, 1978; Hodell et al., 2012; Tan et al., 2014; Gázquez et al., 2017; Herwartz et al., 2017). The reported equilibrium fractionation factors generally agree within error indicating that values derived from different techniques can be treated as equivalent (Fig. 3.4). In principle, variations of fractionation factors are insignificant in the natural temperature range from 10°C to 35°C and at salinities < 150 $g \cdot l^{-1}$ (Gonfiantini and Fontes, 1963; Sofer and Gat, 1972, 1975; Horita, 1989). However, Gázquez et al. (2017) showed that a salt correction of $^{2}\alpha_{\mathrm{SBW-AW}}$ is necessary even at relatively low salinities. Fractionation factors published by Gázquez et al. (2017) are $^{2}\alpha_{\mathrm{SBW-AW}} = 0.9812 \pm 0.0007$ at 20°C

and $^{18}\alpha_{SBW\text{-}AW} = 1.0035 \pm 0.0002$ between 3° and 55°C. The fractionation factor for $^{17}O/^{16}O$ can be determined using the triple isotope law (e.g. Rozanski et al., 2001):

$$^{17}\alpha_{SBW-AW} = {}^{18}\alpha^{\theta}_{SBW-AW} \tag{3.21}$$

with $\theta_{SBW\text{-}AW} = 0.5297 \pm 0.0012$ as determined by Gázquez et al. (2017), this results in $^{17}\alpha_{SBW\text{-}AW} = 1.00185 \pm 0.0001$.

The opposite fractionation of hydrogen and oxygen isotopes between SBW of gypsum and AW may be attributed to isotope fractionation between the free ambient water and the hydration sphere of the dissolved ion (Taube, 1954; Gonfiantini and Fontes, 1963; Oi and Morimoto, 2013). The enrichment in ^{18}O may be explained by the effect of the Ca^{2+} hydration sphere, while the depletion in ^{2}H may be caused by the hydration sphere of SO_4^{2-}.

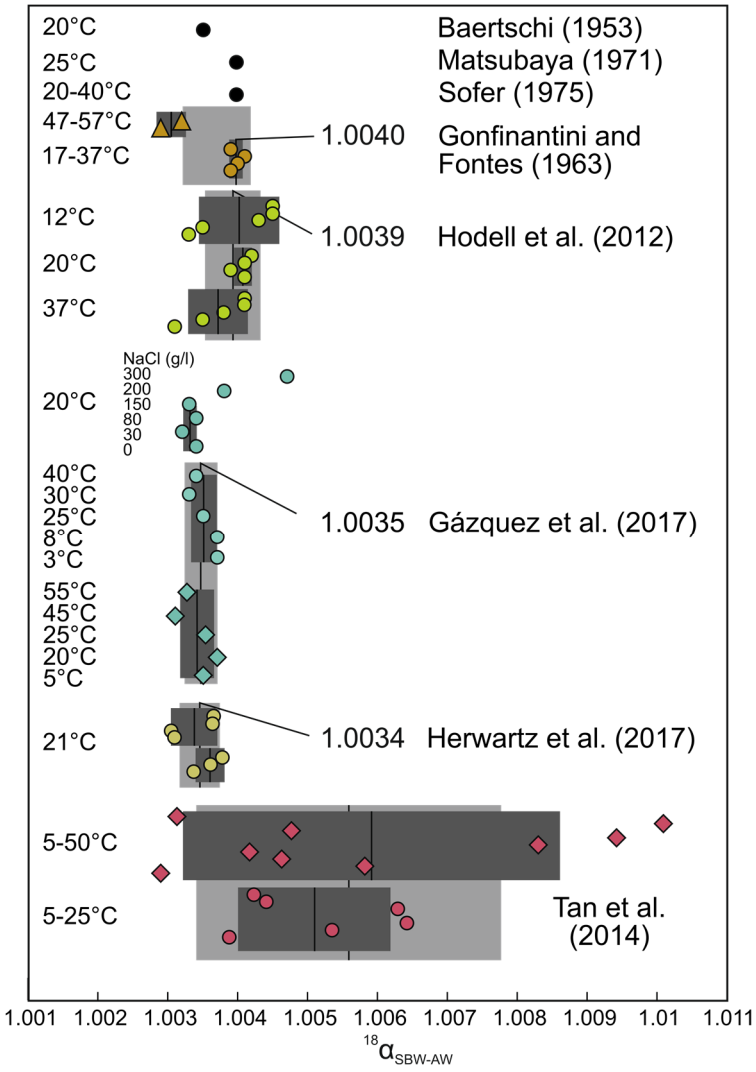

Figure 3.4: Published $^{18}\alpha_{SBW\text{-}AW}$ equilibrium fractionation factors. Different symbology represents applied techniques. Triangles: evaporation of solution saturated in $CaSO_4$, circles: hydration of anhydrite, and diamonds: mixing of $CaCl_2$ and Na_2SO_4 solutions (modified after Herwartz et al., 2017).

4 Objectives

The primary objective of this thesis is to evaluate the potential of combining analyses of hydrogen and triple oxygen isotopes of structurally bonded water of lacustrine and pedogenic gypsum to reconstruct paleoclimate changes. Within this framework, the presented studies aim to improve the understanding of fundamental processes in complex and highly dynamic hydrological systems and evaluate impacts of variations in water availability on soil formation and secondary transformation processes. Isotope analyses of structurally bonded water of lacustrine gypsum deposits intended to examine the applicability of the method to quantitatively estimate paleo-humidity. The successful application of this new method to different lacustrine and pedogenic gypsum deposits in the Atacama Desert will ultimately contribute to an improved understanding of forcing and feedback mechanisms that determine local climatic conditions but also impact climate on a global scale.

Chapter 5 deals with hydrogen and triple oxygen isotope systematics during evaporation that were investigated at the Salar del Huasco, an endorheic salt flat located in the semiarid Altiplano, N-Chile. This salar is a complex and dynamic hydrological system with multiple sources and seasonally distributed short events of precipitation, episodic surface runoff and fluctuations in the water table. The environment is characterized by exceptionally high evaporation rates and high variability in relative humidity and temperature throughout the year. Several natural waters in and around the salar were sampled during several field campaigns to investigate the dynamic seasonality of the hydrological system. Additionally, in-situ pan evaporation experiments were carried out to constrain relevant variables of the C-G model equation. The isotopic compositions of the waters were determined by isotope ratio mass spectrometry and compared to modeled evaporation trajectories based on the Craig-Gordon model using modern seasonal average conditions at the Salar del Huasco site. The results reveal the potential of triple oxygen isotope analyses to determine processes controlling the hydrologic balance of lakes. The study contributes to a better understanding of hydrological processes in complex and highly dynamic salt lake systems.

Chapter 6 focusses on the applicability of isotope analyses of structurally bonded water of lacustrine gypsum for paleo-climate reconstruction. Gypsum crystals were collected from individual stratigraphic units of lacustrine deposits from two sites in the Atacama Desert. Both sites are of Miocene to Plio-Pleistocene age. In laboratory, the water that is structurally bonded in the gypsum

crystal was extracted and analyzed for its hydrogen and triple oxygen isotope composition. The Craig-Gordon model together with a Monte Carlo simulation was applied to determine the range of possible model solutions that fit the measured isotope data. The results provide information on climatic conditions (humidity, temperature, wind) during gypsum formation. Different scenarios were used to evaluate the applicability of the method to quantify paleo-humidity and potentially estimate paleo-temperature.

Chapter 7 presents the first systematic study on the spatial distribution of calcium sulfate phases and soluble salts in Atacama Desert soils between 19.5-25°S and 68.5-70.5°W. Total soil chemical analysis (ICP-OES and spectrophotometric analysis) as well as XRD and thermogravimetric analysis were applied to determine gypsum and anhydrite abundances along with contents of chloride, nitrate, and major elements. The results give insights into soil formation and secondary mobilization processes and their links to water availability, which is crucial in understanding the history of landscape evolution. Along with this study, valuable information on processes controlling anhydrite formation and secondary transformation of gypsum in Atacama Desert soils were gathered.

5 Triple oxygen isotope systematics of evaporation and mixing processes in a dynamic lake system

5.1 Introduction

Triple oxygen isotope analysis of ice, lake water, plant water, water structurally bonded in minerals – e.g. gypsum – or minerals exchanging with ambient water during their formation – e.g. amorphous silica and carbonate – have been recognized as a potentially powerful tool in studies of the present and the past hydrologic cycle (e.g. Landais et al., 2006, 2008; Uemura et al., 2010; Surma et al., 2015, 2018; Evans et al., 2015, 2018; Herwartz et al., 2017; S. Li et al., 2017; Alexandre et al., 2018, 2019; Gázquez et al., 2018; Passey and Ji, 2019). The foundations of this tool lie in isotope fractionation theory, which predicts small differences in the relationship between $^{17}\alpha$ and $^{18}\alpha$ during kinetic and equilibrium fractionation (Angert et al., 2004). Later, improvements in analytical procedures (Baker et al., 2002) allowed to resolve these small variations (Barkan and Luz, 2005, 2007). The triple oxygen isotope exponent $\theta = \ln {}^{17}\alpha / \ln {}^{18}\alpha$ was found to be 0.529 for liquid-vapor equilibrium (Barkan and Luz, 2005) and 0.5185 for diffusion of water vapor in air (Barkan and Luz, 2007). Triple oxygen isotope analyses of meteoric water across the globe reveal a linear relationship between $\delta^{17}O$ and $\delta^{18}O$ – the Global Meteoric Water Line (GMWL) similarly to the classic $\delta^{2}H$-$\delta^{18}O$ system (Luz and Barkan, 2010):

$$\delta'^{17}O = 0.528 \cdot \delta'^{18}O + 0.000033 \qquad (6.1)$$

with $\delta' {}^{x}O = 1000 \cdot \ln(\delta {}^{x}O/1000 + 1)$. For better visualization of deviations from the GMWL, the ^{17}O excess parameter has been defined (Luz and Barkan, 2010):

$$^{17}O - \text{excess} = \delta'^{17}O - 0.528 \cdot \delta'^{18}O \qquad (6.2)$$

In natural desert lakes, the progress of evaporation causes a systematic decrease of ^{17}O-excess largely in response to relative humidity. The evaporation trend is principally predictable on regional scale by the classic Craig-Gordon (C-G) isotopic evaporation model (Surma et al., 2015, 2018). The studies by Surma et al (2015, 2018) also laid out how, besides humidity, other climate variables and hydrological parameters including temperature, wind turbulence, the isotopic composition of atmospheric vapor, continuous groundwater recharge, and progressively increasing salinity shape evaporation trajectories in a diagram of ^{17}O-excess over $\delta^{18}O$.

Most highly evaporative environments show significant seasonal variability in all the above variables. In addition, mixing with episodic sources – e.g. flooding after thunderstorms or snowmelt – or simply a variable proportion of multiple groundwater sources with different composition may affect lake's isotope composition. To examine these factors, we tested the applicability and robustness of the C-G model for triple oxygen isotopes in a complex and highly dynamic desert lake system – the Salar del Huasco, an endorheic salt flat located in the semiarid high-altitude Altiplano Plateau, N-Chile. The hydrological balance of this salar is controlled by a shallow groundwater table, perennial streams, rare and highly seasonal precipitation, and episodic injection of runoff water after thunderstorms and snowmelt. The environment is characterized by exceptionally high evaporation rates and high variability in relative humidity and temperature throughout the year with considerable diurnal amplitude. An on-site weather station provides records of local weather data. In addition, we were able to constrain relevant variables from the C-G model equation by in-situ pan evaporation experiments. Springs around the Salar del Huasco were sampled to evaluate isotopic variability of inflowing water sources. We show evaporation trajectories modeled for seasonal conditions at the Salar del Huasco in comparison to measured isotope data from water samples covering a 300 ‰ salinity range. This study identifies many aspects of the seasonal dynamics in this complex hydrological system that influence the isotopic composition of natural ponds at the Salar del Huasco. We also demonstrate that triple oxygen isotope analyses, in contrast to classic δ^2H and $\delta^{18}O$ measurements, may distinguish different major hydrological processes like recharge and mixing and allow to identify changes in the hydrological balance of lakes.

5.2 Study area

The Salar del Huasco is an endorheic salt flat located in the south of a longitudinal volcano-tectonic depression in the Chilean Altiplano at about 3770 m (Fig. 5.1). It covers an area of about 50 km^2 but only 5 % of the surface is permanently covered by water (Risacher et al., 2003).

Mean annual values of relative humidity and temperatures are 42 % and 4°C, respectively (CEAZA, 2019). Both relative humidity and temperature are highly variable throughout the year with mean seasonal values of 59 % and 8°C in austral summer (Dec-Mar) and 34 % and 1°C in austral winter (Jun-Sep) (CEAZA, 2019). Day-night fluctuations range between 1 and 99 %, and from -19°C to 22°C (CEAZA, 2019). Mean annual wind speed is about 2.5 $m \cdot s^{-1}$, most times coming from S to

SW direction (CEAZA, 2019). Typically, it is calm in the morning, but very windy in the afternoon with 4 $m \cdot s^{-1}$ average wind speed and gusts up to 20 $m \cdot s^{-1}$ (CEAZA, 2019).

Precipitation occurs mainly in austral summer (Dec-Mar), where it is often of convective nature and related to easterly airflow from the Atlantic Ocean and the Amazon Basin (e.g. Aravena et al., 1999; Garreaud et al., 2003; Houston, 2006). In contrast, less frequent winter rains and snow are associated with the interaction of cold air masses from the Pacific with tropical air masses from the Amazon Basin (Aravena et al., 1999). Long-term mean annual precipitation is 150 $mm \cdot a^{-1}$, but interannual variability is high due to their dependence on wind patterns (Garreaud and Aceituno, 2001; Risacher et al., 2003).

The hydrogeological system consists of three aquifers, where the upper and the intermediate aquifer are located in the basin's sediment infill, separated by a thin aquitard, and the lower aquifer is formed in volcanic bedrock (Acosta and Custodio, 2008). The upper aquifer is recharged by the Collacagua river that drains the northern part of the basin and completely infiltrates 10 km before reaching the salar (Acosta and Custodio, 2008). In periods of heavy rainfall, the river can directly flow into the salar leading to widespread flooding of the northern area (Fig. 5.2e). Several springs and creeks around the salar and the shallow groundwater table contribute to the formation of perennial lakes. Furthermore, ephemeral ponds emerge episodically due to precipitation, surface and subsurface runoff and a rising groundwater table in the rainy season.

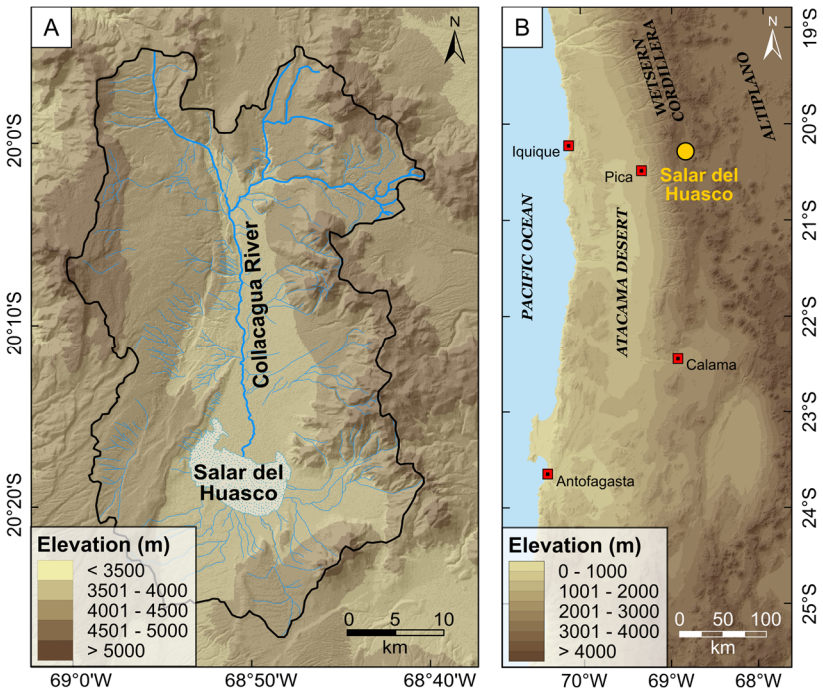

Figure 5.1: Study Area. (A) Catchment of the Salar del Huasco (Salar del Huasco basin) with drainage. (B) Overview map. (DEM derived from SRTM data, created using ArcGIS 10.5.1)

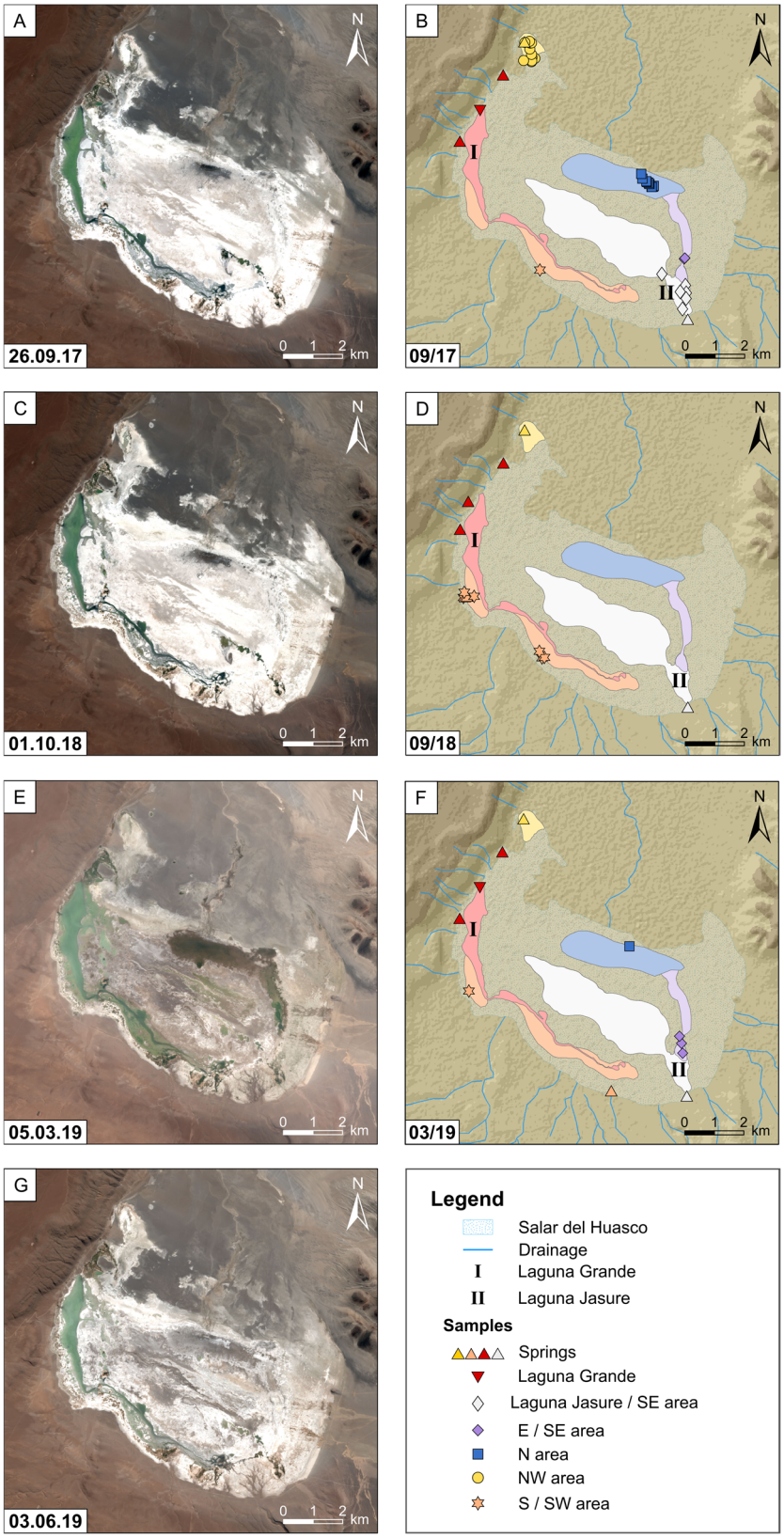

Figure 5.2: Illustration of the hydrological situation at the Salar del Huasco over the sampling period with sample locations for field campaigns in 09/17 (A and B), 09/18 (C and D), and 03/19 (E and F). Panel (G) reflects the hydrological situation at the Salar del Huasco 6 months after the last sampling campaign. Several hydrological subsystems (coloured areas) were identified based on satellite images (Copernicus Sentinel data, 2017, 2018, 2019) and field observations. Different symbols of sample locations refer to the corresponding hydrological subsystem (see text for details). (DEM derived from SRTM data, created using ArcGIS 10.5.1)

Variable groundwater and stream sources, episodic precipitation and surface runoff, and ephemeral flooding in austral summer result in a highly dynamic system with strongly fluctuating lake level. Based on satellite images and field observations, four main hydrological subsystems could be identified (Fig. 5.2). Three springs at the western part of the salt flat and one at the south-eastern margin establish two perennial lake systems – *Laguna Grande* and *Laguna Jasure* (Fig. 5.2b). A channel originating from the *Laguna Grande* extends along the southern margin of the salt flat. This connection may contribute to flooding of southern areas during lake's high level (Fig. 5.2e). Lowering of the water table over the dry season may lead to isolation of small lakes at the southern margin of the salar. A further subsystem in the north is probably fed by subsurface inflow of the Collacagua river. The northern area may become widely flooded in austral summer (Fig. 5.2e), but likely dries up rapidly after the rainy season (Fig. 5.2g). The northern subsystem is at least temporarily connected to the south-eastern system as indicated by a small channel observed in satellite images. A minor subsystem in the north-western area seems to be mainly fed by the shallow groundwater table since no surface inflow could be observed during either field campaign. Several chains of lakes and a number of isolated ponds on topographic highs were observed in the north-western subsystem during field campaigns in September 2017 and 2018. In contrast, despite extensive rainfall in February 2019 that flooded much of the salt flat, the north-western area was almost dry in March 2019.

5.3 Sampling

Pan evaporation experiments with 600 ml, 800 ml, and 1000 ml of fresh water (0.805 $mS \cdot cm^{-1}$) filled in stainless steel evaporation pans (Ø 20 cm) were carried out on site over a period of three days. Samples were taken every day around 18:00 and, additionally, at the third day after 13:00. The pan filled with 600 ml fresh water, dried up before the end of the experiment so that no sample could be taken in the evening of the last day. Air temperature, relative humidity, and wind speed were monitored locally at the experiment using a *Kestrel 5500 weather meter* (Fig. A1.1). Mean relative humidity and temperature are 4°C and 35 % over the whole period of the experiment. As temperatures dropped below 0°C in the night, a considerable fraction, if not all, of the water in the pans froze during the night leading to either a solid ice block or a thick ice layer above some of the remaining liquid. Consequently, evaporation from pans was mostly restricted to daytime. The effective evaporation time interval was assumed to last from 9:30 to 23:30 – the period when

T > 0°C. During that time, average air temperature and relative humidity were 11°C and 21 %, with extreme values of 23°C and 7 % occurring just after midday (Fig. A1.1). Water temperatures measured during sampling were found to be up to 5°C lower than ambient air temperatures. However, during midday, temperatures of water may exceed air temperatures by several degrees due to solar heating of the pans. The wind was very strong between 12:00 and 19:00 with an average wind speed of 5 $m \cdot s^{-1}$ and gusts up to 14 $m \cdot s^{-1}$ coming from S to W direction, i.e. the general direction of the Pacific coast.

Natural water samples from the Salar del Huasco were taken during field campaigns in September 2017, September 2018 and March 2019 (Fig. 5.2 and Table A1.1). The sample set includes spring waters, perennial lakes (*Laguna Grande* in the W, and *Laguna Jasure* in the SE) and ephemeral ponds of which several were apparently recharged and some apparently stagnant. Lakes and ponds are all very shallow (5-30 cm). Samples were taken from the water surface and temperature, pH, and conductivity were measured on site using a digital precision meter *Multi 3620 IDS*.

In the south-eastern area, a perennial spring feeds a chain of lakes with generally low salinity < 2 $g \cdot l^{-1}$. Some ponds were visibly connected by streams and creeks. Others located closer to the eastern margin of the salt flat, were topographically elevated and therefore isolated from the main south-eastern inflow. Satellite images indicate that ponds closer to the salar's center may represent a mixture of source water from the south-eastern inflow and the northern Collacagua subsystem (Fig. 5.2e).

Ponds from the northern area sampled in 09/17 were characterized by an extreme salinity gradient from 2 to 343 $g \cdot l^{-1}$ broadly decreasing from east to west (Table A2.1). These ponds were often salt-encrusted and showed black, sulfur-reducing microbial mats at the bottom. In 03/19, this entire area was covered by a large low-salinity lake.

In the north-western area, a spring originating from a small, vegetated hill fed a series of ponds with salinities < 1 $g \cdot l^{-1}$. An adjacent chain of ponds about 750 m to the south-east with salinities between 1 and 6 $g \cdot l^{-1}$ was not visibly connected to this spring and must have been sustained by the shallow groundwater table. Three topographically elevated ponds close to the margin had higher salinity of 8 to 40 $g \cdot l^{-1}$. The area around these ponds was more vegetated, indicating that these ponds were older, i.e. represented an earlier flooding but became isolated from recharge.

Additional samples were taken from shallow lakes and ponds at the south to south-western margin of the salar. Satellite images and field observations indicate that this area is flooded by branches of the Laguna Grande during the rainy season and that lowering of the water table over the course of the year leads to isolation of ponds (Fig. 5.2e,g).

Besides water samples from surface waters, we sampled atmospheric vapor using a Stirling cooler (*Le-Tehnika*, Kranj, Slovenia) built after Peters and Yakir (2010). Sampling was carried out on the 20.09.17 and the 21.09.17 during the evening from about 18:00 to 21:00 using an air-flow rate of 600-800 ml·min^{-1}.

5.4 Methods

The hydrogen and triple oxygen isotope composition of water samples were analyzed by isotope ratio mass spectrometry (IRMS). Complementary concentration data of Na^+, K^+, Ca^{2+}, Mg^{2+}, Cl^-, and SO_4^{2-} in natural samples were determined by ICP-OES (see Fig. A1.7, Table A1.1).

Hydrogen isotope ratios are measured by continuous-flow IRMS of H_2. Water samples are injected in a silicon carbide reactor (*Heka-Tech*, Wegberg, Germany) that is filled with glassy carbon and heated to 1550°C, where they are reduced to H_2 and CO. The produced gases are separated in a helium gas stream (100-130 ml·min^{-1}) by gas chromatography (GC) and finally, are introduced in a *Thermo Scientific MAT 253* mass spectrometer for hydrogen isotope analysis. The long-term external reproducibility (SD) is about 0.9 ‰ and 1.15 ‰ for δ^2H and d-excess, respectively.

For triple oxygen isotope analysis, water samples are fluorinated, followed by dual-inlet IRMS of O_2. The method is described in detail in Surma et al. (2015) and Herwartz et al. (2017). In brief, 2.8 µl of water are injected in a heated CoF_3 reactor (370°C) that is continuously flushed with helium (30 ml·min^{-1}). The produced oxygen gas is cryogenically purified and trapped in one of twelve sample tubes of a manifold. The manifold is connected to a *Thermo Scientific MAT 253* for dual-inlet IRMS analysis. The long-term external reproducibility (SD) is about 0.12 ‰, 0.25 ‰ and 8 per meg for $\delta^{17}O$, $\delta^{18}O$ and ^{17}O-excess, respectively. All isotope data herein are reported on SMOW-SLAP scale (Schoenemann et al., 2013). The scale is usually contracted using the setup described herein. This can partly be attributed to blank contribution (Herwartz et al., 2017). We observe an increase in scale contraction over the usage period of a CoF_3 reactor filling and a reduction of precision and accuracy of isotopic data, which may indicate that the blank contribution increases with time. To account for this effect, SMOW-SLAP scaling was performed daily using

internal laboratory standards. Isotope measurements with anomalous high scaling factors or standard deviations were discarded.

5.5 The Craig-Gordon isotopic evaporation model at the Salar del Huasco

The classic evaporation theory distinguishes two principal evaporation scenarios, one with recharge (recharge evaporation) and one without recharge (simple evaporation) (Craig and Gordon, 1965; Criss, 1999; Horita et al., 2008). The C-G model does not account for mixing processes, e.g. as a result of flooding or snowmelt, but can be used to calculate such effect by applying mass balance. These three main trajectories are principally resolvable in triple oxygen isotope space, whereas in the classic δ^2H–$\delta^{18}O$ system they tend to merge within data uncertainty (Fig. 5.3). All three trajectories can be expected in a dynamic arid hydrological setting such as the Salar del Huasco. Water affected exclusively by evaporation must progress along either of the two principal evaporation trajectories defined by the C-G model. Episodic flooding after rainfall events are detectable on satellite images of Salar del Huasco (Fig. 5.2). Thus, mixing processes are likely, but should only be transient due to the rarity of flooding events.

The major variables determining the isotopic composition of evaporating water (i.e. residual water) are relative humidity (h), temperature (T) and wind-induced turbulence (an empirically determined coefficient n) along with the isotopic composition of atmospheric vapor (δ_V) and initial or inflowing water (δ_{WI}) (Craig and Gordon, 1965; Criss, 1999; Horita et al., 2008). The effect of wind turbulence – which is related to wind speed – is accounted for by inserting a correcting exponent to the diffusive fractionation factor, $\alpha_{diff,l\text{-}v}{}^n$ (Dongmann et al., 1974). The turbulence coefficient n can theoretically vary between 0 (fully turbulent atmosphere) and 1 (still atmosphere), but typically assumes values of $n \geq 0.5$ under natural conditions (Gonfiantini, 1986; Mathieu and Bariac, 1996; Surma et al., 2018). Salinity affects isotope activities and increases fluid viscosity thereby decreasing the vapor pressure above the water body. In the C-G model, this may be accounted for by correcting equilibrium fractionation factors for the classic salt effect (Horita, 1989, 2005; Horita et al., 1993) and using effective rather than actual relative humidity. However, this effect only requires consideration in the δ^2H–$\delta^{18}O$ system at salinities > 100 $g \cdot l^{-1}$ and was therefore neglected in our model calculations (Sofer and Gat, 1972, 1975; Horita, 1989, 2005).

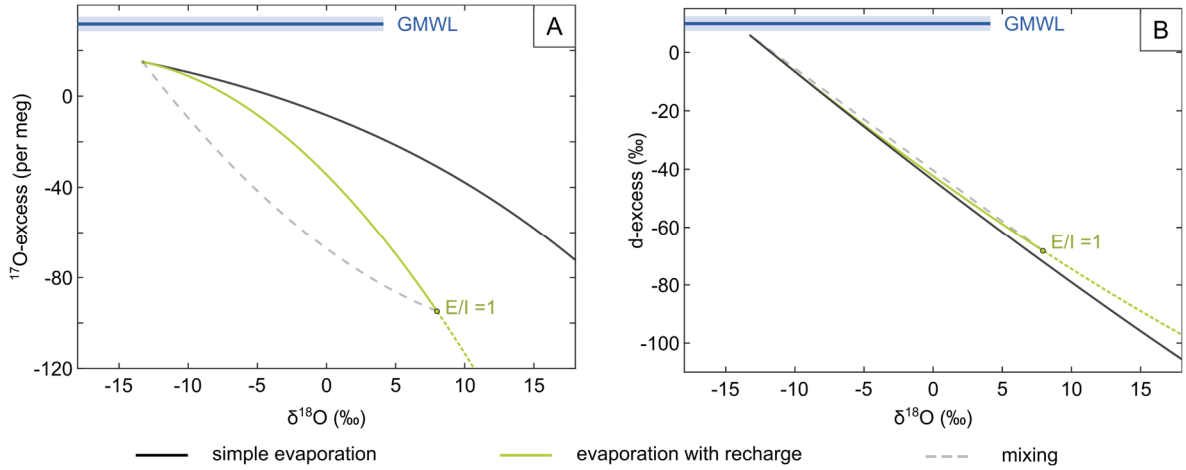

Figure 5.3: Comparison of evaporation trajectories for simple and recharged evaporation and mixing in triple oxygen isotope space (A) and in the classic d-excess vs $\delta^{18}O$ system (B). The solid black line shows a simple evaporation trajectory for the case of evaporation without recharge. The solid green line illustrates the isotopic evolution of a recharged lake system during evaporation in dependence on the E/I ratio. The dashed grey line exemplifies mixing for the case of a terminal lake (E/I = 1), e.g. by flooding after a storm event.

In this study, four of the five variables (T, h, n, δ_{WI}, δ_V) in the C-G equation are known from monitoring (T, h) and direct measurements (δ_{WI}, δ_V). The turbulence coefficient n is not easily obtainable from wind speed monitoring but can be derived from the evaporation experiment (see section 5.6.2). The vapor composition (δ_V) was measured directly but may be more variable over the sampling period than our two days of measurement suggest. There may only be a weak relationship on average between vapor and rainfall composition at the Salar del Huasco. High-precipitation events in austral summer show significant isotopic variability that is related to a variable continental effect in the Amazon Basin and the intensity of convective storms (Aravena et al., 1999). Winter rains comprise generally higher $\delta^{18}O$ values and are isotopically less variable than summer rains. This may be attributed to less variability in the contribution of pre-evaporated water from the Amazon Basin in the dry season and the non-convective nature of winter storms (Aravena et al., 1999). The isotopic composition of winter rains reflects a mixture of moisture from air masses originating from the Amazon Basin and from the Pacific Ocean, while the mean annual isotopic composition of atmospheric vapor over the Salar del Huasco basin is dominated by air masses derived from Pacific sources (Garreaud et al., 2003).

5.6 Results and Discussion

5.6.1 Atmospheric vapor

Atmospheric vapor was sampled on 20.09.17 and 21.09.17. Measurements revealed an average $\delta^{18}O_V$ value of -19.4 ± 2.3 ‰. Average d-excess$_V$ and ^{17}O-excess$_V$ values are 30 ± 3 ‰ and 18 ± 2 ‰, respectively. Seven-day air mass back trajectories calculated using the HYSPLIT Lagrangian model suggest that air masses during vapor sampling are mainly derived from westerly sources (Fig. A1.3). A predominantly western origin of vapor is confirmed for the time of our sampling campaign in 09/17 by 7-day air mass back-trajectories calculated for the month prior to sampling using the HYSPLIT Lagrangian model (Fig. 5.4; Stein et al., 2015).

Results apparently deviate only slightly from the OIPC model's mean annual $\delta^{18}O_V$ value of -21.8 ‰ (Bowen et al., 2005). However, the OIPC model estimate is based on two fundamentally different precipitation processes, where on one hand there is a major contribution of the Amazon moisture source with convective summer rain, high rainout and depletion of heavy isotopes, and on the other hand a relatively enriched winter snow moisture source (cf. Aravena et al., 1999). These two seasonal aspects coincidently combine to an average value that is similar to our measurements. As such, rainfall data available from the global OIPC precipitation database (Bowen et al., 2005) are not reliable in deriving vapor composition in this environment. The isotopic composition of atmospheric vapor is therefore better represented by the small number of direct measurements of water vapor collected during the sampling campaign at a time, where the actual synoptic weather condition during sampling most likely reflects the annual average condition reasonably well.

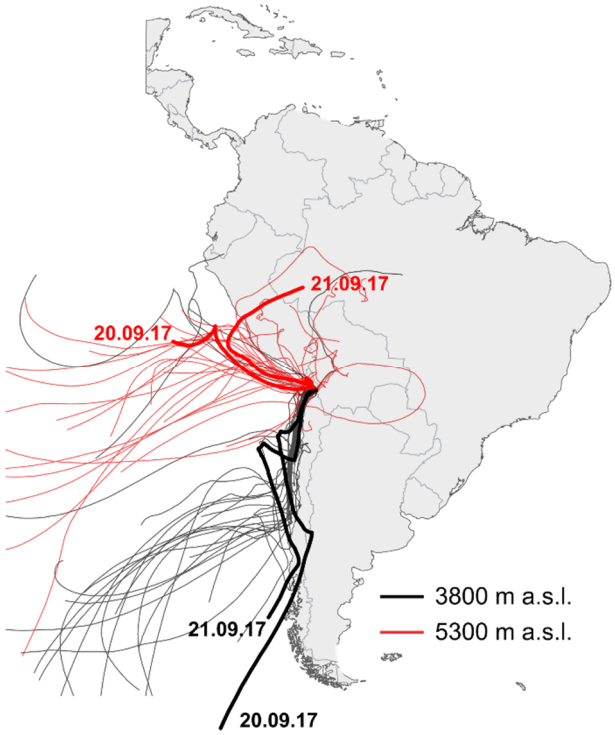

Figure 5.4: HYSPLIT 7-day air mass back trajectories modeled for ground level at the Salar del Huasco (~3800 m above sea level (a.s.l.)) (black) and 1500 m above ground level (5300 m a.s.l.) (red) in daily resolution for the period from 23.08.2017 to 22.09.2017. The thick red and black trajectories represent the origin of atmospheric air masses at the Salar del Huasco for the time of vapour sampling on 20.09. and 21.09.2017.

5.6.2 Pan evaporation experiments

Evaporation trajectories in the isotope diagrams were modeled for pan evaporation experiments using the simple (pan) C-G model. Here, the isotopic composition of inflowing water and atmospheric vapor, salinity, temperature and relative humidity are constrained by direct measurement or monitoring over the period of the experiment (Table A.1.1). The coefficient *n* for wind-induced turbulence is a parametrized value that cannot be directly measured but is well constrainable from isotopic data. An evaporation trajectory for given boundary conditions with a suitable turbulence coefficient *n* may be derived empirically from a plot of d-excess over the fraction of remaining water by determining the best model fit through all experimental data (Fig. 5.5). In this diagram, the trajectory is predominantly affected by the magnitude of the turbulence coefficient, and only barely sensitive to the other variables of the C-G equation. Notably, this approach is insensitive to our least well constrained variable, $\delta^{18}O_V$ (Fig. 5.5b). A Monte Carlo error simulation yields n = 0.44. However, turbulence coefficients observed under natural conditions world-wide are typically ≥ 0.5 (Merlivat and Jouzel, 1979; Gonfiantini, 1986; Mathieu and Bariac,

1996; Surma et al., 2018). The above-average turbulence indicated by this low value could reflect excessive evaporation at prevailing gale-force winds during midday, and reduced evaporation during the calmer times of the day and during the night and early morning when the experiment waters were frozen over. Unfortunately, the freezing at nighttime introduces a complicating aspect that results in uncontrollable effects on the relationship between d-excess and the fraction of remaining water in this particular experiment. When the ice begins to melt slowly in the morning, a considerable fraction, if not the whole resulting water film on top of the pan's frozen surface layer may evaporate at the same time. The fraction of total water in the pan would thus be reduced without affecting the isotopic composition of the bulk ice. In our experimental setup, this essentially equals an overestimation of the fraction of water lost during daytime evaporation and would systematically shift the isotopic data above the predicted evaporation trajectory in d-excess vs residual fraction, limiting its potential to precisely estimate the turbulence coefficient. Alternatively, the C-G model may be used to derive the turbulence coefficient n by fitting the evaporation trajectory through measured isotopic data in a diagram of d-excess over $\delta^{18}O$. This comes with the caveat of considerable sensitivity to the assumed value for $\delta^{18}O_V$. However, at given boundary conditions – including the measured average $\delta^{18}O_V$ = -19.4 ‰ – the best fit is obtained for a value of n = 0.54 (Fig 5.6a). For n = 0.44 estimate and the given boundary conditions, the data do not fall on the modeled evaporation trajectory (Fig. 5.6b). To obtain a fit with $n = 0.44$, $\delta^{18}O_V$ = -28.9 ± 0.25 ‰ must be assumed. Such a value appears unrealistically low in comparison to our measurements as well as a hypothetical value derived from the OPIC model assuming equilibrium fractionation between vapor and rain ($\delta^{18}O_V$ = -21.8 ‰). Because $n = 0.54$ derived from the latter approach is in good agreement with the global range of values, and because the freeze-over of the pan experiment may effectively lead to an undesired weighting of the estimate towards the stormy midday in the former approach that is not representative for the majority of unfrozen natural ponds, we tentatively choose to work with the higher value.

In a ^{17}O-excess vs $\delta^{18}O$ diagram, the isotopic data fall below the predicted evaporation trend, regardless which turbulence coefficient is used. In this case, two unresolvable effects may be the reason for the mismatch. Partial melting during the thawing of our experiment in the morning may result in uncontrollable mixing effects that are only observable in a ^{17}O-excess over $\delta^{18}O$ diagram (Fig A1.4). Furthermore, in evaporation experiments the diurnal variations of temperature and relative humidity, and corresponding changes of the isotopic end point of evaporation lead to a

diurnal evolution of the simple (pan) evaporation trajectory (Fig. A1.5; Surma et al., 2018). Both effects become increasingly important, as the experiment progresses to smaller residual water volumes, consistent with our data. Unfortunately, we were not able to perform the necessary high-resolution sampling of the evaporation experiment to resolve these effects and obtain a representative average evaporation trajectory.

In conclusion of this experiment, we suggest that the complementary analysis of all water isotopes in evaporation experiments principally allows to determine the turbulence coefficient and to constrain the composition of ambient vapor with sufficient confidence. The remaining uncertainty in the accuracy of our estimate of *n* in this particular study is, fortunately, not relevant for the following discussion.

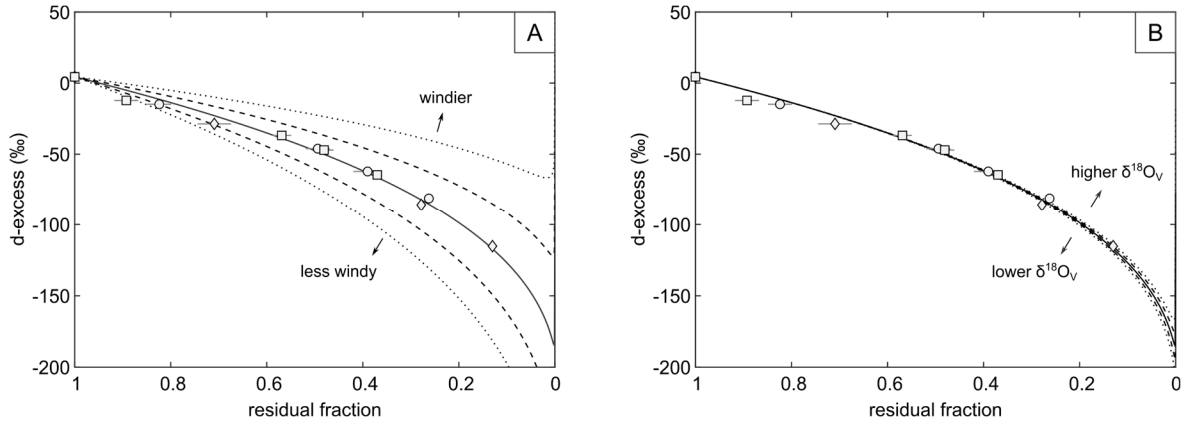

Figure 5.5: Sensitivity of d-excess vs residual fraction to A) the turbulence coefficient *n* and B) the isotopic composition of atmospheric vapor $\delta^{18}O_V$ with isotopic data of pan evaporation experiments with initial volume of 600 ml (diamonds), 800 ml (circles), 1000 ml (squares). Note that the symbol size is larger than error bars. The solid line represents the modeled evaporation trajectory for simple evaporation conditions using model input parameters as summarized in Table 5.1 and a turbulence coefficient of 0.44. Dashed lines show model results with A) different turbulence coefficients *n* in steps of 0.1 and B) varying isotopic composition of atmospheric vapor $\delta^{18}O_V$ in steps of 5 ‰, keeping all other parameters constant.

Table 5.1: Model input parameters for the simple evaporation model for pan evaporation experiments.

Parameter	Value
$\delta^{18}O_{WI}$ (‰)	-10.96
d-excess$_{WI}$ (‰)	4.4
^{17}O-excess$_{WI}$ (per meg)	16
$\delta^{18}O_V$ (‰)	-19.4
d-excess$_V$ (‰)	30
^{17}O-excess$_V$ (per meg)	18
Temperature (°C)	11
Relative humidity (%)	21
Turbulence coefficient	0.54

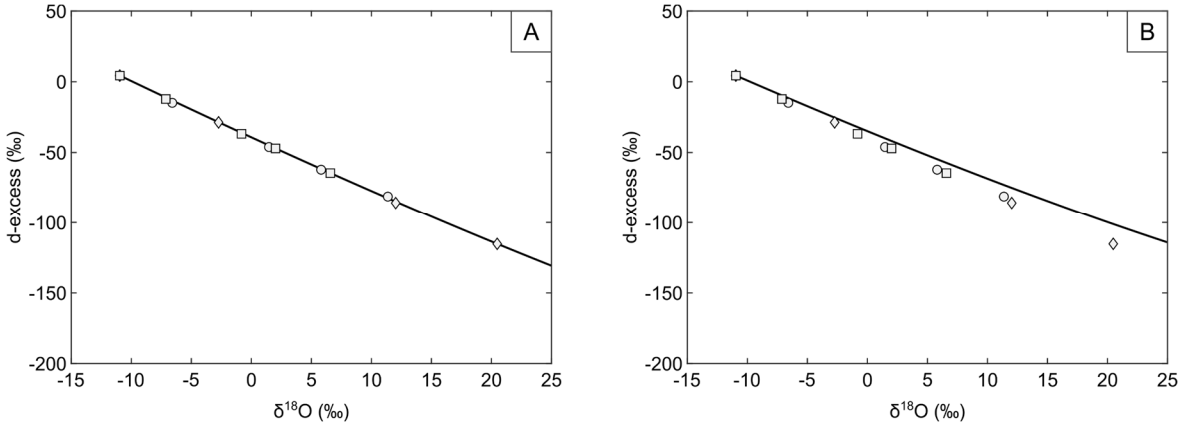

Figure 5.6: Comparison of evaporation trajectories in d-excess vs $\delta^{18}O$ modeled for turbulence coefficients n = 0.54 (A) and n = 0.44 (B), keeping other parameters constant (Table 5.1). Additionally, isotopic data of pan evaporation experiments are shown. Different initial volumes are represented by different symbols: 600 ml – diamonds, 800 ml – circles, 1000 ml – squares. Note that the symbol size is larger than error bars.

5.6.3 Springs and the Collacagua river

The different aquifers in the Salar del Huasco basin are reasonably similar in isotopic composition as indicated by previously published isotopic data of springs and wells (-12.56 ± 1.36 ‰ in $\delta^{18}O$ and 3.2 ± 5.7 ‰ in d-excess; data from Fritz et al., 1981; Uribe et al., 2015; Jayne et al., 2016). These values are in good agreement with our own data derived from springs sampled in 09/17 around the salar with average $\delta^{18}O$ of -12.45 ± 0.64 ‰, d-excess of 2.2 ± 2.9 ‰, and ^{17}O-excess 11 ± 7 per meg. The springs' isotopic composition shows only slight intra- and interannual variability comprising average $\delta^{18}O$, d-excess and ^{17}O-excess values of -12.31 ± 0.50 ‰, 1.3 ± 2.2 ‰ and 6 ± 7 per meg in 09/18 and -12.55 ± 0.68 ‰, 5.5 ± 2.0 ‰, and 2 ± 6 per meg in 03/19, respectively. The $\delta^{18}O$ values of springs in the Salar del Huasco basin are within the range of local precipitation ($\delta^{18}O$ = -17 to -13 ‰; Scheihing et al., 2017 and references therein), but the springs' isotopic range generally falls below the GMWL which seems to be typical for rivers and groundwaters in the Atacama Desert and is also observed in other desert environments (Aravena, 1995; Surma et al., 2015, 2018). Low d-excess values may principally be attributed to evaporation along the riverbed and during infiltration of precipitation in the soil (Aravena, 1995). However, since evaporation trajectories are generally flat in triple oxygen isotope space at early stages of evaporation, low ^{17}O-excess values of springs and rivers cannot be explained by evaporation alone. The only process known to cause lowering in ^{17}O-excess without strongly affecting $\delta^{18}O$ is admixture of an evaporitic endmember (cf. Fig. 5.3). Such mixing processes may occur during flooding events, where pristine precipitation eventually mixes with evaporated residual pond waters prior to infiltration or

evaporitic water reservoirs within the soil. As mixing may occur in several events, the ^{17}O-excess can be substantially lowered.

The Collacagua river, sampled at about 15 km distance from the salar, revealed similar δ^{18}O values in 09/18 (-12.38 ‰) and 03/19 (-12.45 ‰) that coincide well with the average isotopic composition of springs. As for the springs, the isotopic composition of the Collacagua river falls below the GMWL comprising d-excess and ^{17}O-excess values of 1.6 ‰ and 5 per meg in 09/18 and 5.8 ‰ and 5 per meg in 03/19, respectively. The Collacagua river and its tributaries originate from springs at different altitudes in the Salar del Huasco basin (c.f. Fig. 5.1). These springs, and thus the tributaries of the Collacagua river, probably differ slightly in isotopic composition due to the altitude effect (Uribe et al., 2015). The measured isotopic composition of the Collacagua river likely reflects a mixture of water from its tributaries, further modified by evaporation along the riverbed.

5.6.4 Water isotopes in ponds and lakes of the Salar del Huasco

The isotopic composition of lakes and ponds from the Salar del Huasco sampled in the period from 09/17 to 03/19 principally reflect evaporation trends predicted by the C–G model for given boundary conditions (Table 5.2; Fig. 5.7). Most of the ponds fall close to the recharged evaporation trajectory indicating that evaporation along with surface inflow by springs, streams and creeks as well as groundwater recharge dominate the hydrological system (Fig. 5.7). A few ponds sampled in 03/19 seem to be 'non-recharged' as their isotopic composition follows the simple evaporation trajectory (Fig. 5.7). These ponds are probably of transient nature filled up by heavy rainfalls and flooding in 02/19. Both evaporation trends – recharge evaporation and simple (pan) evaporation – are well resolved in a plot of ^{17}O-excess over δ^{18}O but are blurred by insensitivity in a diagram of d-excess over δ^{18}O (Fig. 5.7).

A considerable number of ponds, particularly those sampled in 09/17, falls below the predicted recharge evaporation trajectory (Fig. 5.7). This may be partly attributed to source variability (δ_{WI}). Ponds and lakes in the Salar del Huasco receive inflow from multiple sources that especially differ in their ^{17}O-excess values (Fig. 5.7). Additionally, the isotopic composition of recharging groundwater may vary spatially due to admixture of evaporated pond water to the groundwater table. The isotopic composition of inflowing water also varies slightly intra- and interannually due to the seasonality of precipitation and the impact of evaporation (Fig. 5.7a,c,e). The variability in the isotopic composition of spring water, particularly in ^{17}O-excess$_{WI}$, broadens the range of

evaporation trend lines in the diagram of ^{17}O-excess over $\delta^{18}O$, especially for throughflow lakes ($E/I < 0.5$) and can account for the offset of most of the ponds.

Additionally, discrepancies between the predicted evaporation trendline and the actual isotopic composition of ponds and lakes from the Salar del Huasco may arise due to remaining uncertainty in other model input parameters, particularly the isotopic composition of atmospheric vapor. The value of $\delta^{18}O_V$ was estimated from a two-spot measurement but might be more variable over the course of the year. Slightly lower $\delta^{18}O_V$ values would lead to a stronger curvature of evaporation trajectories in a diagram of ^{17}O-excess over $\delta^{18}O$. However, the best fit is produced by lowering $\delta^{18}O_V$ to about -30.0 ‰, which seems unlikely considering our measurements (-19.4 ‰) and the hypothetical value derived from the OPIC model (-21.8 ‰). Furthermore, using $\delta^{18}O_V$ = -30.0 ‰, all pond data would fall slightly above predicted evaporation trendlines in a diagram of d-excess over $\delta^{18}O$. Simple mass balance suggests isotopic depletion of $\delta^{18}O_V$ by -30 ‰ between the Pacific coast and the Salar del Huasco implying $\delta^{18}O_V < -40$ ‰ for the Salar del Huasco site. However, such extreme values are highly unlikely. On their way from the Pacific Ocean, the air masses cross the hyperarid Atacama Desert, where precipitation is extremely rare and isotope fractionation due to condensation should be low. Condensation may only occur during the ascent of air masses over the Coastal Cordillera and the Western Cordillera. Measurements of atmospheric vapor revealed a systematic decrease in the isotopic composition of atmospheric vapor with increasing distance from the coast (A1.5). The process that leads to this systematic trend is not yet understood. A possible mechanism could be fog and dew formation by radiative cooling at night that re-evaporates in daytime. Furthermore, absorption of atmospheric vapor by salts is feasible.

Table 5.2: Model input parameters of the simple and the recharge evaporation model for ponds and lakes.

Parameter	2017	2018	2019
$\delta^{18}O_{WI}$ (‰)	-13.28	-13.03	-13.22
d-excess$_{WI}$ (‰)	6.0	5.1	6.3
^{17}O-excess$_{WI}$ (per meg)	15	7	9
$\delta^{18}O_V$ (‰)	-19.4	-19.4	-19.4
d-excess$_V$ (‰)	30	30	10
^{17}O-excess$_V$ (per meg)	18	18	18
Temperature (°C)	6	6	11
Relative humidity (%)	23	30	44
Turbulence coefficient	0.54	0.54	0.54

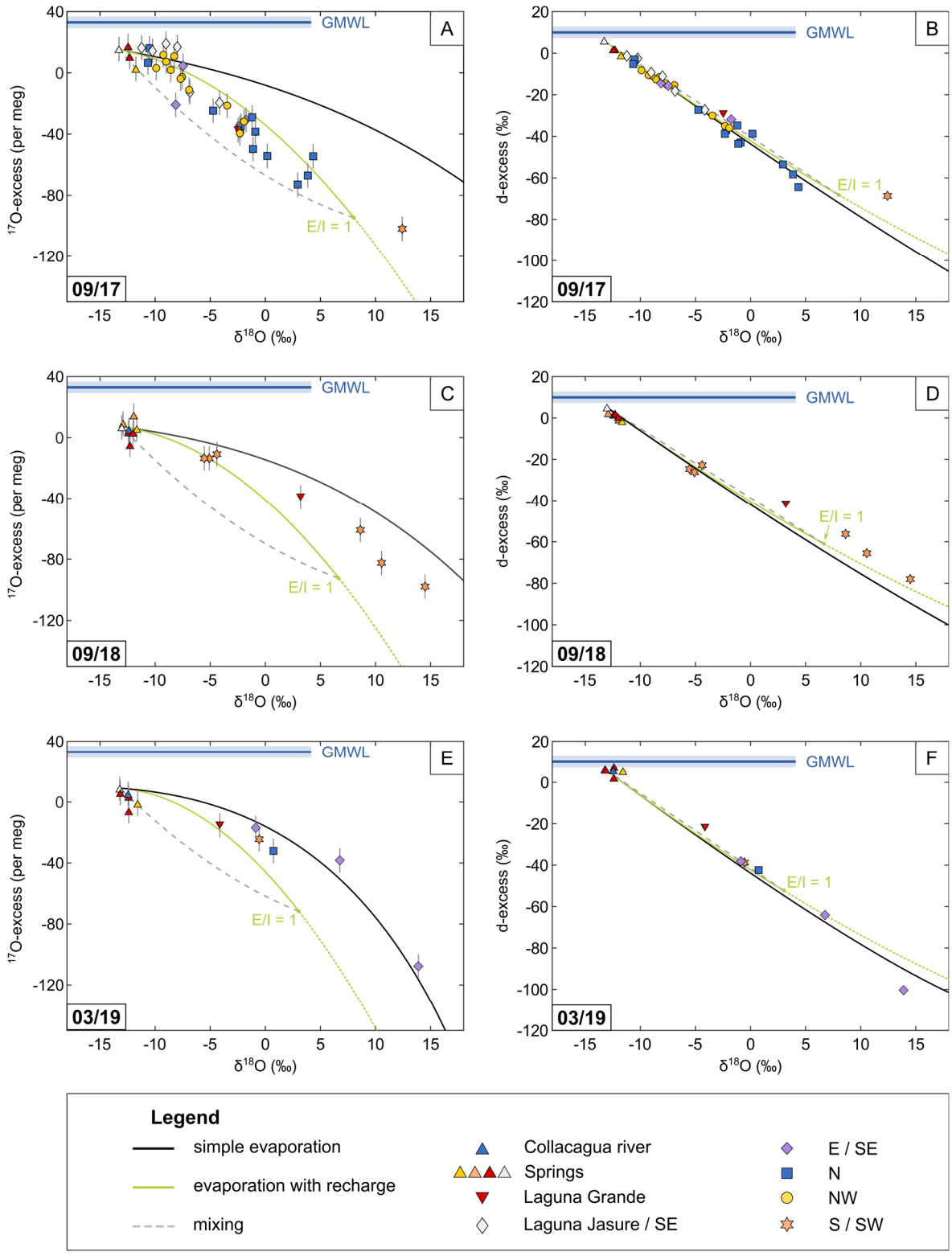

Figure 5.7: Oxygen and hydrogen isotope data of the Collacagua river, springs, lakes and ponds sampled in the Salar del Huasco basin during field campaigns in 09/17 (A and B), 09/18 ((C and D), and 03/19 (E and F). Color coding refers to different hydrological subsystems (see legend and cf. Fig. 5.1). Note that the symbol size can be larger than the error bars. Trajectories for simple evaporation (black) and evaporation with recharge (green) were modeled using input parameters as summarized in Table 5.2. Additionally, admixture of fresh groundwater as it might occur during flooding or snowmelt is exemplified for the case of a terminal lake (E/I = 1) (dashed grey line). The Global Meteoric Water Line (GMWL) serves as reference.

Some uncertainty also remains in assumed values for temperature and relative humidity. Evaporation rates are probably highly variable throughout the day as indicated by the strong diurnal amplitude of temperature, relative humidity and wind speed. Thus, temperature and relative humidity need to be weighted based on actual evaporation rates. However, using T = 9°C and h = 17 % weighted for the diurnal distribution of temperature and wind speed rather than the seasonal daytime mean values of T = 10°C and h = 23 % do not significantly affect the evaporation trajectory in triple oxygen isotope space. As evaporation trajectories in triple oxygen isotope space are relatively insensitive to both temperature and relative humidity at given boundary conditions (δ_{WI}, δ_V) at the Salar del Huasco, the uncertainty introduced by the diurnal variability of temperature and relative humidity to modeled trajectories is principally low.

Besides uncertainty in the modeled trajectories, mixing processes that occur episodically at the Salar del Huasco e.g. during flooding and snowmelt, may contribute to the large offset to the predicted recharge evaporation trendline observed for a few ponds from the Salar del Huasco. All ponds and lakes from 09/17 fall between the mixing line for a terminal lake and the predicted recharge evaporation trend (Fig. 5.7). Thus, the isotopic composition of all ponds can be explained by admixture of freshwater to recharged ponds at different steady-states ($0 \leq E/I \leq 1$). Depending on the E/I ratio of the lake, admixture of meteoric water to evaporated lake water during flooding shifts the lake's isotopic composition along mixing lines below the predicted evaporation trend in triple oxygen isotope space (Fig. 5.3). Since flooding events are principally rare, isotope effects due to mixing should be transient. After flooding the isotopic composition of the pond water tends back to the steady-state value on the recharge evaporation trajectory.

Based on satellite images and field observations different hydrological subsystems in the Salar del Huasco were identified (cf. Fig. 5.2). The perennial lakes – *Laguna Grande* in the western part and *Laguna Jasure* in the south-eastern part – are visibly recharged by springs, streams and creeks. However, at lake's high level in austral summer, the recharge rate may be insignificant compared to the volume of the water body driving the isotopic composition of lakes in both areas on the simple evaporation trend (Fig. 5.7e). The north-western subsystem is isolated from surface inflow and, thus, may be sustained by the shallow groundwater table. Variations in the groundwater table may contribute to fluctuations in the extend of lakes in this area. The hydrological balance of ponds and lakes in the northern area depends on the flow discharge of the Collacagua river that may fluctuate strongly over the course of the year due to the seasonality of precipitation and high evaporation

along the riverbed. Satellite images indicate that in periods of heavy rainfall in austral summer the river can flow directly into the salar leading to widespread flooding of the northern area and the emergence of a large ephemeral summer lagoon (Fig. 5.2e). Due to extreme evaporation (1500 mm·a^{-1}; Risacher et al., 2003), this lagoon rapidly desiccated (Fig. 5.2g). Small very saline ponds may be sustained by low groundwater recharge. Ponds and lakes in the southern area are highly dynamic throughout the year. Satellite images and field observations indicate that the area is flooded by branches of the Laguna Grande in the rainy season, and that drop down of the water table over the course of the year may cause changes in the recharge rate and can ultimately lead to isolation of individual ponds (Fig. 5.2). When recharge is completely stopped, the isotopic composition of the lake evolves towards the simple evaporation trendline. Our sample set may include ponds that were still connected to the main flow and others that were already 'cut-off' from recharge explaining the large variability observed in their isotopic composition. A few ponds with slighter higher ^{17}O-excess values than springs sampled in 09/18 indicate the existence of small springs along the southern margin of the salar (Fig. 5.7c,d).

5.7 Conclusion

The classic Craig-Gordon isotopic evaporation model reliably predicts isotopic evaporation trends of lakes and ponds in highly dynamic lacustrine systems in a desert environment with considerable seasonal and diurnal variability in temperature and relative humidity. Deviations from the predicted trendline occur with episodic inflow from a secondary source, e.g. flooding after precipitation events, that can lead to the emergence of ephemeral non-recharged lakes and may induce mixing processes. Furthermore, inflow from multiple sources and spatial and temporal variability in their isotopic composition may lead to dynamic variations in the isotopic composition of ponds and lakes. Triple oxygen isotope analysis of lakes provides the opportunity to identify these processes, which are not resolvable with conventional δ^2H–δ^{18}O measurements. As mixing processes may be transient and source variability may be averaged out over timescales of gypsum precipitation, reconstructing changes in paleo-humidity by combined analyses of hydrogen and triple oxygen isotopes of water structurally bonded in minerals, e.g. gypsum, may principally be applicable in complex and highly dynamic lake systems.

The turbulence coefficient in the C-G model can be estimated with confidence from a series of in-situ pan evaporation experiments by fitting evaporation trajectories to the isotopic data in a plot of

d-excess over the fraction of remaining water or in d-excess over $\delta^{18}O$ space. More systematic experimental studies of on-site evaporation may eventually allow to calibrate the turbulence coefficient with respect to wind speed.

6 Quantitative reconstruction of paleo-humidity using triple oxygen and hydrogen isotopes

6.1 Introduction

Stable isotope analyses of hydrogen ($^{2}H/^{1}H$) and oxygen isotopes ($^{18}O/^{16}O$) in water are a widely used tool in hydrological studies. Recent advances in mass spectrometry permit the precise analysis of the ^{17}O isotope (Barkan and Luz, 2005). In contrast to the classic $\delta^{2}H$-$\delta^{18}O$ system, the triple oxygen isotope system ($\delta^{17}O$-$\delta^{18}O$) is nearly independent of salinity and temperature providing additional information on processes in the hydrological cycle. In natural desert lakes, evaporation systematically affects the isotopic composition of lake water – mostly in response to humidity. Hydrogen and triple oxygen isotope systematics during evaporation are principally predictable by the classic Craig-Gordon (C-G) evaporation model (Craig and Gordon, 1965; Horita et al., 2008; Surma et al., 2015, 2018).

Lacustrine gypsum ($CaSO_4 \cdot 2\ H_2O$) forms in evaporative environments and thereby captures the isotopic composition of ambient lake water in its crystal lattice. Several studies of gypsum deposits up to Miocene age demonstrated that the primary isotopic signature of structurally bonded water (SBW) of gypsum can be preserved over prolonged timescales (Sofer, 1978; Khademi et al., 1997; Farpoor et al., 2004; Hodell et al., 2012; Evans et al., 2015; J. Li et al., 2017; Gázquez et al., 2018). Thus, the isotopic composition of SBW of gypsum principally provides information on the isotopic composition of paleo-lake water at the time of gypsum precipitation (Hodell et al., 2012; Evans et al., 2015, 2018; Grauel et al., 2016; Herwartz et al., 2017; J. Li et al., 2017; Gázquez et al., 2018). Recent studies demonstrated that past changes in relative humidity can be quantified by fitting the C-G function to isotopic data of paleo-lake water derived from SBW of gypsum (Gázquez et al., 2018).

In this study, we analyzed the isotopic composition of SBW of gypsum sampled from two spatially separated stratigraphic units of Late Miocene to Plio-Pleistocene lacustrine deposits from the Atacama Desert in order to investigate its potential to quantitatively reconstruct paleo-humidity conditions during gypsum formation. Primary evaporation trends in paleo-lake water seem to be preserved in SBW of gypsum, which principally allows to quantify individual climate parameters, i.e. humidity and temperature. A set of reasonable model input parameters including the isotopic

composition of atmospheric vapor and source water of paleo-lakes, is defined based on the environmental setting of the gypsum deposits and site information gained from other studies. We use a Monte Carlo simulation to find the Craig-Gordon evaporation model solution that best fit the measured isotopic data. The model provides valuable information on humidity conditions at the time of gypsum formation independent of other input variables such as temperature, the isotopic composition of source water and atmospheric vapor.

6.2 Regional overview and study sites

The Atacama Desert extends along the west coast of South America from northern Chile to southern Peru. It is bounded by the Pacific Ocean to the west and the high Andes to the east. The tectonic morphology is characterized by three major north-south trending geomorphologic provinces that reflect the Nazca-South America convergent plate boundary system (Fig. 6.1). The Coastal Cordillera forms the western margin of the Atacama Desert with elevations between 800 and 2000 m. It constitutes the remnant of the volcanic arc that was active during the Cretaceous (Haschke et al., 2002). To the east follows the Central Depression, which is a sedimentary forearc basin characterized by low-relief surface with an average elevation of 1000 m (Hartley et al., 2000; Hartley and Evenstar, 2010). Large parts of the Central Depression are endorheic collecting sediments derived from the high Andes in the east. Between 19°35'S and 25°25'S, the Rio Loa river is the only drainage to the Pacific Ocean, while north of 19°35'S, the Central Depression is deeply incised by several canyons ('quebradas') that drain headwaters from the Andes to the Pacific Ocean. The Central Depression gently slopes eastwards to the Precordillera and the Western Cordillera reaching elevations around 4000 m with peaks up to 6000 m. The Western Cordillera represents the presently active volcanic arc of the Central Andes (Garzione et al., 2017).

Arid conditions ($< 10\ mm \cdot a^{-1}$) dominate throughout the Atacama Desert with pronounced hyperaridity of $< 2mm \cdot a^{-1}$ prevailing between 19°S and 22°S (Houston, 2006; Ritter et al., 2018b). Aridity broadly decreases eastwards with increasing elevation from the Central Depression towards the Andes (Houston, 2006). Moreover, coastal areas between 650 and 1200 m receive sporadically fog that is caused by low stratocumulus clouds forming below the atmospheric temperature inversion layer over the Pacific Ocean (Cereceda et al., 2002, 2008). Fog may penetrate further inland through topographic corridors in the Coastal Cordillera.

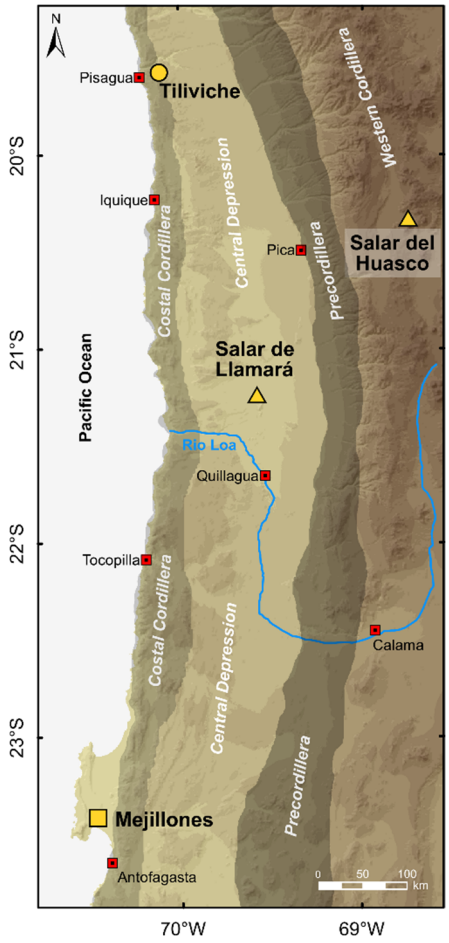

Figure 6.1: Regional overview of the Atacama Desert. The Atacama Desert is bounded to the west by the Pacific Ocean and to the east by the high Andes. Running from west to east, the major tectonic units are the Coastal Cordillera, the Central Depression, Precordillera and the Western Cordillera. Within this study, past climate conditions during the formation of gypsum deposits at the Mejillones Peninsula (square) and close to the Tiliviche Canyon (circle) were investigated and compared to present environmental conditions in the Central Depression (Salar de Llamará) and in the high-altitude Altiplano (Salar del Huasco) (triangles).

The present hyperaridity results from the combination of (1) the latitudinal position within the subtropical high-pressure belt and the associated subsidence of dry and warm air masses induced by the Hadley circulation, (2) the coastal upwelling of cold water masses of the Humboldt Current that prevents moisture uptake and transport to the Atacama Desert, and (3) the rain shadow effect of the Andes that act as a moisture barrier for humid air masses derived from the Atlantic Ocean and the Amazon Basin (Hartley and Chong, 2002; Houston and Hartley, 2003). Arid conditions prevail throughout the Atacama Desert at least since 25 Ma, but were locally interrupted by several pluvial phases (Evenstar et al., 2017 and references therein). The temporal and spatial climate variability in the past Atacama Desert is under extensive investigation but still poorly understood. Especially quantitative climate data are scarce, since paleoclimate investigations are mostly based on proxy material, e.g. lacustrine sediments, paleosols and subfossil biological material (Gaupp et

al., 1999; Sáez et al., 1999, 2012; Betancourt et al., 2000; Rech et al., 2006, 2019). Furthermore, paleoclimate archives often integrate over large catchments that cover several magnitudes of climate gradients (e.g. Bao et al., 1999; Evenstar et al., 2009; Sáez et al., 2012; Kirk-Lawlor et al., 2013; Jordan et al., 2014; Pfeiffer et al., 2018). Thus, local aridity may be diminished by more humid conditions in spacious catchments. The aim of this study is to develop and establish a new tool based on hydrogen and triple oxygen isotope analyses of structurally bonded water of gypsum that can provide quantitative information on local climatic conditions during gypsum formation.

6.2.1 Mejillones

The 'Mejillones' site (23°20.14'S 70°32.85'W) is an active gypsum mine that is located in the southern part of the Mejillones Peninsula about 30 km north of Antofagasta at the western edge of the central Atacama Desert (Fig. 6.1). The Mejillones Peninsula is bounded to the east by the Coastal Cliff (~1000 m high) and extends up to 30 km along the N-S trending coastline (Fig. 6.1). The topography of the peninsula is dominated by horst and half-graben structures that are generated by N-S striking normal faults (Armijo and Thiele, 1990; González et al., 2003; Di Celma et al., 2014).

The investigated gypsum outcrop forms a local topographic high in the western part of the central half-graben basin (*Caleta Heradura* basin) at an elevation of about 130 m about sea level (asl). The hill is approximately 10 m high. Most of the hill is covered by debris, however, several massive gypsum banks of up to 1 m thickness crop out at surface. These banks are partly intercalated by thin, up to 10 cm thick, grey muddy sediment layers. The base of the gypsum deposits is formed by dark grey sandy sediment that is rich in mollusc and shell fragments. In general, the gypsum crystals are elongated, vertically exposed and often intergrown. The size of gypsum crystals ranges from < 1 cm to ~10 cm and typically increases from bottom to top within individual banks. Samples were taken from gypsum banks at the top of the hill as well as from several banks within the outcrop (Fig. A2.1). Some banks that show several cycles of gypsum growth were sampled in detail.

The gypsum crystals probably formed in a marine lagoon that was active in Pliocene times (Di Celma et al., 2014). Marine sedimentation on the Mejillones Peninsula was initiated with the beginning of fault activity during the Early Miocene (Armijo and Thiele, 1990; Hartley and Jolley, 1995; Hartley et al., 2000; González et al., 2003). It was initially restricted to the north-western sector, but subsequently extended over large areas of the peninsula resulting in a widespread

shallow marine environment throughout the Pliocene (Di Celma et al., 2014). Periodic accretion of sediments may have cut off areas from open marine circulation leading to the formation of lagoons in which evaporites such as gypsum precipitated (Di Celma et al., 2014). Marine sedimentation terminated in the Pleistocene when tectonic uplift raised the central part of the Mejillones Peninsula above sea level, most likely around 790 ka ago (Victor et al., 2011).

The recent climate on the Mejillones Peninsula is mainly controlled by the Pacific Ocean. Mild temperatures with 16°C in annual mean and relative humidity of around 70 % dominate throughout the year (Dirección Meteorológica de Chile, 2020). The temperature profile shows weak seasonality with maximum temperatures of about 21°C during austral summer (Feb) and minimum temperatures around 14°C in austral winter (Jul) (Dirección Meteorológica de Chile, 2020). Daily temperature fluctuations are considerable higher ranging between 9°C and 30°C, while the relative humidity varies within 56-90 % between day and night (Dirección Meteorológica de Chile, 2020). A sea breeze is typical for coastal sites like Mejillones. Wind speeds average to 4 $m \cdot s^{-1}$ and reach maxima of up to 10 $m \cdot s^{-1}$ in the afternoon. Precipitation occurs sporadically by fog, dew or rain, mostly in austral winter (Jun/Jul) and spring (Oct/Nov). Precipitation amounts are usually less than 2 mm per event and < 5$mm \cdot a^{-1}$ (Dirección Meteorológica de Chile, 2020).

6.2.2 Tiliviche

The 'Tiliviche' site (19°33.90'S 70°07.05'W) is located in the northern Atacama Desert near Pisagua around 9 km further inland from the coast (Fig. 6.1). The sample site is situated in the westernmost part of the Central Depression and directly abuts the Coastal Cordillera (Fig. 6.1). The investigated area spans approximately 1-2 km^2 of relatively low relief at an average elevation of about 920 m asl. To the north, the area is restricted by the *Quebrada Tiliviche* that drains headwaters from the high Andes to the Pacific Ocean. Deposits of the *Tiliviche Formation* (salar halites) are outcropping in at least four distinct levels of up to 1-2 m thickness with decreasing thickness towards the east (Fig. A2.2). A relict gypsic soil covers the uppermost halite bank.

Gypsum crystals occur locally in small nests of about 1 m^2 on top of the second and the third bank (Fig. A2.2). At one site, we found gypsum crystals at the transition to the lowermost halite bank. Gypsum crystals are often elongated ranging in length approximately between 1 and 10 cm. They probably grew at the bottom of a paleo-salar as it can be observed in recent salar systems such as the Salar de Llamará (Herwartz et al., 2017). Based on sedimentological, stratigraphic and

geomorphological data, Kirk-Lawlor et al. (2013) proposed the existence of a deep-water lake in the western part of the Central Depression between 19.3°S and 19.7°S during the Late Miocene to Pliocene (10.86–6.4 Ma). The lake was probably fed by proto-streams of *Quebrada Tiliviche* and *Quebrada Tana* with minor contributions of *Quebrada Aroma*. Subsequently, the hydrological balance of the lake shifted from balance-fill to underfilled and the near surface groundwater table led to the development of a salar environment and the accumulation of evaporites, e.g. gypsum, at ~3.5 Ma (Kirk-Lawlor et al., 2013). The reason for the ultimate termination of the lacustrine-salar system is highly debated (Farías et al., 2005; Garcia et al., 2011; Kirk-Lawlor et al., 2013; Evenstar et al., 2015; Cosentino and Jordan, 2017). The drop of the water table can either be tectonically driven (Garcia and Hérail, 2005; Kirk-Lawlor et al., 2013; Coudurier-Curveur et al., 2015; Evenstar et al., 2015; Cosentino and Jordan, 2017; Binnie et al., 2020) or caused by climatic variations (Farías et al., 2005; Garcia et al., 2011; Jeffery et al., 2012). Recent results support the hypothesis that tectonic uplift of the sedimentary forearc basin and coastal retreat caused a ~1 km base level drop that initiate canyon incision and finally led to the desiccation of the salar (Kirk-Lawlor et al., 2013; Coudurier-Curveur et al., 2015; Cosentino and Jordan, 2017). The widespread occurrence of lacustrine and evaporitic deposits of Late Miocene and Plio-Pleistocene age in the western part of the Central Depression may be an indication of generally more humid (but still arid) conditions in the Atacama Desert, - e.g. in their large scale catchment areas including the Precordillera (e.g. Gaupp et al., 1999; Sáez et al., 1999, 2012). This period of lacustrine deposition coincide with the Pliocene warm period that contributed to wetter than present climate in the Altiplano and the Central Andes at the Miocene-Pliocene transition (Gaupp et al., 1999; Sáez et al., 1999, 2012; de Wet et al., 2015). The Early Pliocene Warm period (4.5 – 3.0 Ma) may be characterized by permanent El Niño-like conditions with decreased upwelling and warmer sea surface temperatures in the eastern Pacific and a relatively weak Walker circulation (Wara et al., 2005). Permanent El Niño-like conditions may have led to a weakening of the temperature inversion layer over the Pacific Ocean resulting in increased precipitation in the central Atacama Desert (de Wet et al., 2015). However, it remains unclear, how far inland this precipitation could have reached (Feitl et al., 2019).

Today, the Tiliviche site is characterized by mild and dry conditions. Mean annual humidity and temperature are 50 % and 16°C, respectively (Hoffmeister, 2018). The humidity shows strong seasonal variations between 20 % in austral winter (Aug) and about 70 % in austral summer (Jan/Feb). High relative humidity values in austral summer may be related to the frequent

occurrence of fog as indicated by leaf wetness sensor data (Hoffmeister, 2018). The observation of active lichen on pebbles found in the studied area support this assumption. The temperature shows only slight seasonal variations between 14 and 18°C but varies strongly between day and night with minima of 2°C and maxima up to 30°C (Hoffmeister, 2018). The wind system is controlled by temperature gradients between the land surface and the Pacific Ocean. It is typically calm in the morning, since the temperature gradient is small. As the land surface warms up faster than the sea, a local surface low pressure cell develops over the continent and initiates onshore air flow. At the Tiliviche site, in the afternoon hours wind speeds of around 3 $m \cdot s^{-1}$ with gusts up to 6 $m \cdot s^{-1}$ are reached (Hoffmeister, 2018).

6.3 Approach

Evaporation is accompanied by equilibrium and diffusive isotope fractionation that lead to a systematic increase of δ^2H, $\delta^{17}O$, and $\delta^{18}O$ and decrease of d-excess, and ^{17}O-excess in lake water with increasing evaporation. These isotope effects were first described in a conceptual model developed by Craig and Gordon (1965). The main parameters that affect the isotopic composition of evaporating water bodies include the climate variables relative humidity, temperature, and wind turbulence as well as the isotopic composition of inflowing water and atmospheric vapor. Based on the Craig-Gordon model, the isotopic composition of a recharged water body can be quantified by (e.g. Criss, 1999):

$$^{*}R_{WS} = \frac{\alpha_{eq,\,l-v} \cdot \alpha_{diff,\,l-v} \cdot (1 - h) \cdot R_{WI} + \alpha_{eq,\,l-v} \cdot h \cdot E/I \cdot R_V}{E/I + \alpha_{eq,\,l-v} \cdot \alpha_{diff,\,l-v} \cdot (1 - h) \cdot (1 - E/I)} \qquad (6.1)$$

where E/I describes the fraction of water loss by evaporation with respect to inflow, h is the relative humidity, R_{WI} is the isotopic composition of inflowing water, and R_V is the isotopic composition of atmospheric vapor. Temperature dependent equilibrium fractionation factors $\alpha_{eq,\,l\text{-}v}$ and diffusive fractionation factors $\alpha_{diff,\,l\text{-}v}$ for $^2H/^1H$ and $^{18}O/^{16}O$ determined by Horita and Wessolowski (1994) and Merlivat (1978) are used herein. The isotope fractionation factor for $^{17}O/^{16}O$ can be derived from the fractionation factor of $^{18}O/^{16}O$: $^{17}\alpha_{l\text{-}v} = {}^{18}\alpha_{l\text{-}v}{}^{\theta}$ using $\theta = 0.529$ for equilibrium fractionation (Barkan and Luz, 2005) and $\theta = 0.5185$ for diffusive fractionation (Barkan and Luz, 2007).

Diffusive isotope fractionation during evaporation results from the combined effect of molecular and turbulent diffusion, with no isotope fractionation occurring in a turbulent atmosphere. This process is accounted for by adding a turbulence coefficient *n* as an exponent to the diffusive

fractionation factor, $\alpha_{diff,l\text{-}v}{}^{n}$. The turbulence coefficient *n* can principally vary between 0 (no wind) and 1 (fully turbulent atmosphere). However, values of n ≥ 0.5 are typically observed in natural environments (Merlivat and Jouzel, 1979; Gonfiantini, 1986; Mathieu and Bariac, 1996; Surma et al., 2018). Evaporation experiments performed in the Atacama Desert by Surma et al. (2018) and described in the previous study of this thesis (Chapter 5) point to a universal turbulence coefficient of n = 0.5 representative for wind conditions in the Atacama Desert. Therefore, we define n = 0.5 ± 0.1 in this study.

Evaporation trajectories are calculated in dependence on the E/I ratio. In a terminal lake, all inflowing water is lost by evaporation and E/I = 1. Using higher values of E/I > 1 is not intuitive since this would mean that water loss by evaporation exceeds the amount of inflow and the lake desiccates. However, the isotopic composition of a terminal lake depends on the isotopic composition of inflowing water, which may vary over time or be affected by admixture of pre-evaporated water leading to steady state (E/I ≤ 1) at higher $\delta^{18}O$ as implied by our evaporation model. Additionally, large amounts of gypsum can also precipitate in desiccating lakes, e.g. if the lake is episodically refilled in rainy seasons. In our model, we used a maximum E/I value of E/I_{max} = 1.2 to account for possible effects of source variability and episodic flooding.

The predicted evaporation trends take the form of curves, where different diffusive fractionation of $^{2}H/^{1}H$ and $^{17}O/^{16}O$ relative to $^{18}O/^{16}O$ principally cause a different shape of evaporation curvatures in ^{17}O-excess vs $\delta^{18}O$ space and d-excess vs $\delta^{18}O$ space (Figs. A2.3, A2.4). The evaporation trajectories are highly sensitive to relative humidity and $\delta^{18}O_V$ of atmospheric vapor in both ^{17}O-excess and d-excess (Figs. A2.3, A2.4). Temperature has a moderate effect, which is generally smaller for ^{17}O-excess than for d-excess (Gázquez et al., 2018; Surma et al., 2018). Changes in the isotopic composition of inflowing water have a low impact on evaporation trajectories in both cross plots (Figs. A2.3, A2.4). The effect is almost negligible for waters with E/I ratios close to 1. Variations in the wind coefficient mainly influence the length of the curvature (Figs. A2.3, A2.4). Increasing salt contents generally lead to a shortening of the trajectory but become only significant for hydrogen isotopes at high salinities (> 100 $g \cdot l^{-1}$) (Sofer and Gat, 1972, 1975; Horita, 2005; Surma et al., 2018).

The reconstruction of the isotopic composition of the lake water from gypsum requires accurate knowledge of the fractionation factors between structurally bonded water (SBW) of gypsum and ambient water (AW) during gypsum formation. Equilibrium fractionation factors have been

determined experimentally by hydration of anhydrite, gypsum precipitation from $CaSO_4$ saturated solution, and mixing of $CaCl_2$ and Na_2SO_4 solutions (Gonfiantini and Fontes, 1963; Matsubaya, 1971; Sofer, 1978; Hodell et al., 2012; Tan et al., 2014; Gázquez et al., 2017; Herwartz et al., 2017). Regardless the approach used, reported equilibrium fractionation factors broadly agree. A recent systematic study by Gázquez et al. (2017) unveiled a slight temperature dependence for both $^{18}\alpha_{SBW\text{-}AW}$ and $^{2}\alpha_{SBW\text{-}AW}$ and a strong dependence on salinity for $^{2}\alpha_{SBW\text{-}AW}$. However, variations of fractionation factors are negligible in the natural temperature range from 10°C to 35°C, but a salt correction is principally required for $^{2}\alpha_{SBW\text{-}AW}$. Salt concentrations of paleo-waters may be inferred from fluid inclusions (Evans et al., 2015). However, investigations of fluid inclusions were beyond the scope of this study. Since tests with different salinities showed that the effect of salinity on the model results is generally low, the salinity effect was neglected in this study. Throughout this study, we used the equilibrium fractionation factors of $^{2}\alpha_{SBW\text{-}AW} = 0.9812$ and $^{18}\alpha_{SBW\text{-}AW} = 1.0035$ published by Gázquez et al. (2017). The fractionation factor for ^{17}O is related to $^{18}\alpha_{SBW\text{-}AW}$: $^{17}\alpha_{SBW\text{-}AW} = {}^{18}\alpha_{SBW\text{-}AW}$. The triple oxygen isotope exponent θ was determined to be $\theta_{SBW\text{-}AW} = 0.5297 \pm 0.0012$ yielding $^{17}\alpha_{SBW\text{-}AW} = 1.00186$ (Gázquez et al., 2017).

Assuming that all gypsum crystals within one stratigraphic unit precipitate under similar environmental conditions but at variable degree of evaporation, the isotopic composition of paleo-lake water derived from SBW of gypsum should plot along a characteristic evaporation trend line. Monte Carlo simulations were performed to determine the range of possible model solutions that fit the calculated paleo-lake compositions within the error. A set of model inputs is defined based on the environmental setting of the deposits, their modern ranges and their variability in the past. The sum of minimum distances between the modeled trajectory and each data point (incl. 1-sigma standard deviation (1 SD)) is determined in both ^{17}O-excess vs $\delta^{18}O$ space and d-excess vs $\delta^{18}O$ space. The best fitting model solution corresponds to the modeled trajectory with the lowest combined sum of distances of both ^{17}O-excess vs $\delta^{18}O$ and d-excess vs $\delta^{18}O$. The uncertainty of the best fit model solution is determined by modelling the best fit solutions for 100 arrays of data points that are normally distributed within 1 SD of the measured isotopic composition.

6.4 Applicability of the C-G model to reconstruct (paleo-) humidity

Fitting the C-G function to the isotopic composition of paleo-lake water can provide quantitative information on climatic conditions during gypsum formation. The applicability of this tool depends

on the resolution of evaporation trajectories for different relative humidity in triple oxygen isotope space, which is mainly determined by the relative isotopic difference between inflowing water R_{WI} and atmospheric vapor R_V (Surma et al., 2018).

A recent study at Lake Estanya, Spain, demonstrated the potential of combined analyses of hydrogen and triple oxygen isotopes of SBW of gypsum to quantify past changes in relative humidity (Gázquez et al., 2018). Evaporation trajectories for different relative humidity are well distinguishable at the boundary conditions at Lake Estanya (Fig. 6.2a). For this site, model results are quite reasonable suggesting h ~75 % (similar to today) over the Holocene period and dry climatic conditions (h = 40-45 %) during the Younger Dryas (Gázquez et al., 2018). The modeled humidity values coincide well with results obtained from other lake sediment proxies and regional paleoclimate archives demonstrating the principal applicability of the C-G equation and isotopes of SBW of gypsum to reconstruct paleo-humidity (Gázquez et al., 2018).

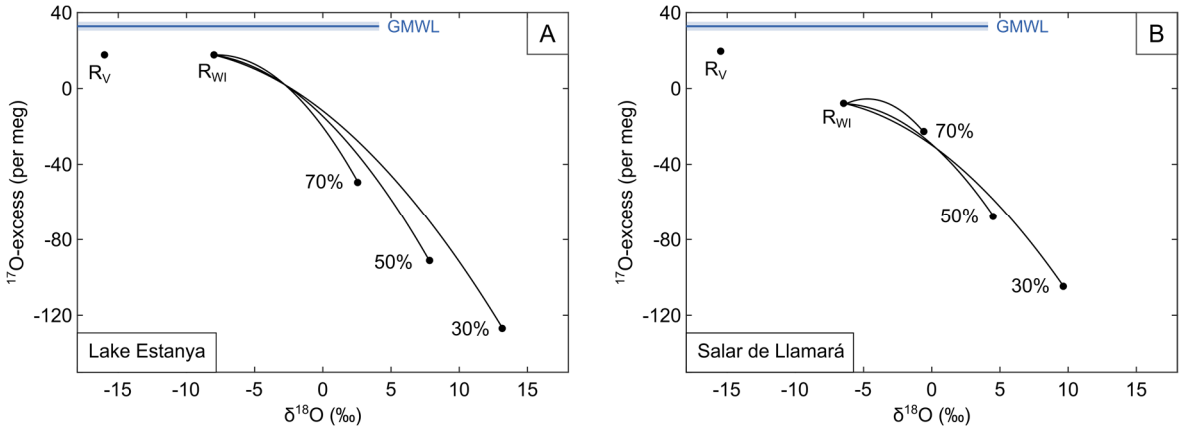

Figure 6.2: Sensitivity of evaporation trajectories in ^{17}O-excess vs δ^{18}O space to changes in relative humidity for Lake Estanya (A) and Salar de Llamará (B). Model input parameters were selected based on environmental conditions at the respective sites (see Gázquez et al. (2018) for Lake Estanya and Surma et al. for Salar de Llamará). Evaporation trajectories were modeled for different relative humidities (30 %, 50 % and 70 %), keeping other parameters constant.

Surma et al. (2018) investigated the isotopic composition of a series of shallow groundwater-fed saline ponds at the Salar de Llamará located in the central part of the Atacama Desert. The isotopic composition of recharging groundwater and atmospheric vapor at Salar de Llamará are almost in line with the common evaporation trend in triple oxygen isotope space (Fig. 6.2b). This leads to the fact that evaporation trajectories for different humidities are difficult to discriminate (Fig. 6.2b; Surma et al., 2018). Fitting the C-G function to isotopic data of ponds from the Salar de Llamará results in best fit model solutions (grey lines in Fig. 6.3) that plot close to the expected recharged evaporation trend for local average h = 43 % weighted for the diurnal distribution of evaporation

rates. However, model results imply a lower humidity of h = 24.4 ± 3.3 % (Fig. 6.3). Thus, accurate and precise modelling of the relative humidity seems quite difficult at this site.

The above evaluation indicates that modelling results can be accurate, especially if evaporation trajectories for different humidities are well resolvable in triple oxygen isotope space. Modelling of evaporation trajectories for different humidity for boundary conditions at the Mejillones Peninsula principally allow sufficiently large resolution to quantify changes in relative humidity (Fig. A2.3). For Tiliviche, however, evaporation trajectories for different humidity cannot be well discriminated for the selected set of model input parameters (Fig. A2.4). Hence, accurate and precise determination of relative humidity may be challenging at this site.

Table 6.1: Model input parameters for Salar de Llamará.

variable	input	output
rH (%)	0 – 100	24.4 ± 3.3
T (°C)	0 – 40	18.4 ± 1.5
wind	0.5	-
$\delta^{18}O_{WI}$ (‰)	-6.295	-
$^{17}O\text{-excess}_{WI}$ (per meg)	7	-
$d\text{-excess}_{WI}$ (‰)	0.8	-
$\delta^{18}O_{V}$ (‰)	-15.3	-
$^{17}O\text{-excess}_{V}$ (per meg)	33	-
$d\text{-excess}_{V}$ (‰)	10	-
E/I_{max}	1.2	-

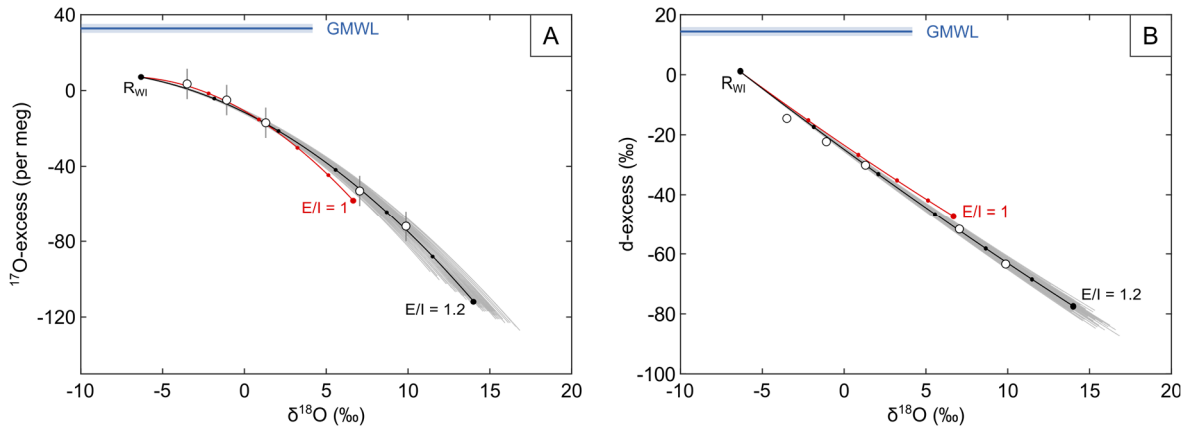

Figure 6.3: Testing the C-G model to quantify humidity at Salar de Llamará based on isotopic data of pond waters (white circles; data from Surma et al., 2018). Note that only ponds were used, for which hydrogen and triple oxygen data were available. The red curve represents the recharge evaporation trajectory using local climatic conditions (h = 43 %, T = 19°C, n = 0.5, $\delta^{18}O_{WI}$ = -6.295 ‰, $^{17}O\text{-excess}_{WI}$ = 7 per meg, $d\text{-excess}_{WI}$ = 0.8 ‰, $\delta^{18}O_{V}$ = -15.3 ‰, $^{17}O\text{-excess}_{V}$ = 33 per meg, $d\text{-excess}_{V}$ = 10 ‰, ρ = 1.1 g·cm^{-3}). The black curve shows the mean of best fit model solutions (grey lines) that satisfy both ^{17}O-excess vs δ^{18}O and d-excess vs δ^{18}O. Model input parameters are summarized in Table 6.1. Small dots along the lines indicate steady states for different E/I in steps of 0.2.

6.5 Methods

6.5.1 Extraction of structurally bonded water (SBW) of gypsum

SBW of gypsum is extracted by *in vacuo* heating to 200°C and cryogenically trapping of liberated water. We developed an extraction line that allows simultaneous extraction of six samples. In each extraction run, a gypsum standard that was produced by rehydration of synthetic anhydrite in 0.5 M Na_2SO_4 solution, is extracted along with five natural samples.

To obtain sufficient water for both hydrogen and triple oxygen isotope measurements, about 1 g of crushed, grinded and homogenized gypsum powder is loaded into 12 mm OD Pyrex tubes. The tubes are capped with 1 cm quartz wool to avoid gypsum powder contaminating the line during the extraction process. The samples are pre-evacuated under low vacuum ($< 5 \cdot 10^{-3}$ mbar) over night to remove adsorbed water (Playà et al., 2005). Before each extraction run, the vacuum is checked by pressure leak tests. Leakages occur due to the deterioration of the Viton O-rings, which therefore must be replaced regularly. Subsequently, the line gets isolated from vacuum. Glass tubes immersed in liquid nitrogen are used as cold traps, while the sample tube is heated to 200°C with a constant heating rate of $3°C \cdot min^{-1}$. Dehydration of pure gypsum mainly occurs between 70°C and 120°C (Voigt et al., 2020). To fully recover the extracted water, the maximum temperature of 200°C is held constant for at least 80 min. Finally, non-condensable gases are pumped, and the glass tubes are flame sealed. Besides pressure control, the sample tubes are weighted before and after the extraction run to ensure complete liberation and trapping of water. Since natural gypsum samples may not be fully hydrated or may contain minor amounts of detritic material, extraction amounts do not necessarily reach the maximum value of 20.9 wt-%. For natural gypsum crystals amounts > 19.5 wt-% are obtained.

6.5.2 Triple oxygen isotope analysis

High precision $\delta^{17}O$ and $\delta^{18}O$ analysis of extracted waters are achieved by fluorination and dual-inlet isotope ratio mass spectrometry (IRMS) on a *Thermo Scientific MAT 253*. The water fluorination line is set up after Barkan and Luz (2005). Details are in given in Surma et al. (2015). In brief, 2.7 µl of water are injected in a CoF_3 reactor heated to 370°C. The liberated gas is carried in a He gas stream with a flow rate of $30 \text{ ml} \cdot \text{min}^{-1}$ through a double cold trap to remove HF. The O_2 gas is trapped in a second trap filled with 150 mg of 5 Å molecular sieve. Heating and refreezing of this trap are performed to purify the O_2 gas. Finally, the O_2 gas is transferred to one of twelve sample

tubes of a manifold. Each sample tube is filled with 30 mg of 5 Å molecular sieve. Both traps and the manifold are immersed in liquid nitrogen.

Each extraction sequence allows the extraction of 12 water samples. Typically, two laboratory working standards are measured along with five samples. The standards are extracted in duplicate bracketing the samples from which three are also extracted in duplicate.

The manifold is connected to the IRMS (*Thermo Scientific MAT 253*) and placed in a water bath to adjust to room temperature. Subsequently, the sample gas is expanded in the sample bellow and measured against a laboratory working reference gas in dual inlet mode. Every measurement consists of 22 sample-reference comparison cycles with 19 s idle time. The internal reproducibility is better than ± 0.020 ‰ ($\delta^{17}O$), ± 0.035 ‰ ($\delta^{18}O$) and ± 7 per meg (^{17}O-excess).

6.5.3 Hydrogen isotope analysis

The analyses of δ^2H is carried out by carbon reduction of the extracted waters and continuous flow isotope ratio mass spectrometry on the *Thermo Scientific MAT 253*. In a silicon carbide tube filled with granulated carbon (*Hekatech*, Wegberg, Germany), 2.0 µl of injected water are reduced to H_2 and CO at a temperature of 1450°C. The gases are transported in a He carrier gas stream with a flow rate of about 135 ± 5 ml·min^{-1}. The gas is filtered to remove trace gases. Subsequently, the H_2 and CO gases are separated in a gas chromatography column, diluted using a *Thermo Conflo IV* device and introduced into the mass spectrometer (*Thermo Scientific MAT 253)*. Sample gas is measured versus reference gas in continuous flow mode. Systematic drifts of isotopic values observed within measurement sequences are linearly corrected using internal laboratory working standards analysed after every 5 to 10 samples. The internal reproducibility of δ^2H is 0.6 ‰.

In principle, the method allows the determination of both δ^2H and $\delta^{18}O$. However, peak tailing of CO sample gas results in large uncertainties for $\delta^{18}O$. Therefore, δ^2H values derived from carbon reduction were combined with high-precision $\delta^{18}O$ values of the triple oxygen isotope analyses to calculate d-excess.

6.5.4 Data treatment

The mean reproducibility of natural samples that were measured two or three times, is ± 0.18 ‰ for $\delta^{17}O$, ± 0.34 ‰ for $\delta^{18}O$, ± 1.6 ‰ for δ^2H, ± 1.9 ‰ for d-excess, and ± 7 per meg for ^{17}O-excess and similar to the external reproducibility of SBW of gypsum previously observed by Herwartz et

al. (2017). Since only a few natural samples were measured multiple times, we adopted the long-term external reproducibility of 0.15 ‰ for $\delta^{17}O$, ± 0.28 ‰ for $\delta^{18}O$ and ± 10 per meg for ^{17}O-excess from Herwartz et al. (2017). For $\delta^{2}H$ and d-excess, we used the reproducibility of natural samples from this study yielding ± 1.6 ‰ and ± 1.9 ‰, respectively. The external reproducibility of gypsum standard samples measured along with each extraction sequence is ± 0.24 ‰ in $\delta^{17}O$, ± 0.46 ‰ in $\delta^{18}O$, ± 2.8 ‰ in $\delta^{2}H$, ± 3.2 ‰ in d-excess, and ± 17 per meg in ^{17}O-excess. These significantly larger standard deviations for both hydrogen and oxygen point towards sample inhomogeneity and/or leakage problems during individual extractions of water from gypsum. Using these larger errors does not affect any conclusions of this study. All data reported herein are calibrated to SMOW-SLAP scale (Schoenemann et al., 2013).

6.6 Results

Ten gypsum samples from the Mejillones site and eight gypsum samples from the Tiliviche site were analysed for the stable isotope composition of their SBW (Fig. 6.4).

Gypsum samples from the Mejillones site comprise evaporitic isotopic composition with variations of $\delta^{17}O_{SBW}$ from 4.0 to 5.7 ‰, $\delta^{18}O_{SBW}$ from 7.7 to 11.0 ‰ and $\delta^{2}H_{SBW}$ from -1.3 to 9.5 ‰. Isotopic values of gypsum samples from the Tiliviche site are significantly lower varying between -1.4 and 0.1 ‰ for $\delta^{17}O_{SBW}$, -2.6 and 0.1 ‰ for $\delta^{18}O_{SBW}$, and -74.7 and -65.4 ‰ for $\delta^{2}H_{SBW}$.

The stable isotope composition of the ambient gypsum mother water from which the gypsum crystals precipitated, is calculated using $^{17}\alpha_{SBW\text{-}AW} = 1.00186$, $^{18}\alpha_{SBW\text{-}AW} = 1.00351$, and $^{2}\alpha_{SBW\text{-}AW} = 0.98024$ at 20°C (Gázquez et al., 2017), which is close to modern mean annual temperatures of 16°C at both sites. Using fractionation factors of ± 10°C results in insignificant changes of the calculated ambient water of ± 0.05 ‰ in $\delta^{17}O_{AW}$, ± 0.1 ‰ in $\delta^{18}O_{AW}$ and ± 1.0 ‰ in $\delta^{2}H_{AW}$.

The calculated isotopic composition of ambient water during the formation of gypsum at the Mejillones site ranges from 4.2 to 7.4 ‰ in $\delta^{18}O_{AW}$ and shows low $^{17}O\text{-excess}_{AW}$ and d-excess_{AW} values varying from -32 to -83 per meg and -14 to -34 ‰, respectively. Less enriched values are determined for ambient water at the Tiliviche site with variations in $\delta^{18}O_{AW}$ from -6.1 to -3.4 ‰, in $^{17}O\text{-excess}_{AW}$ from 3 to -20 per meg and in d-excess from -4 to -20 ‰.

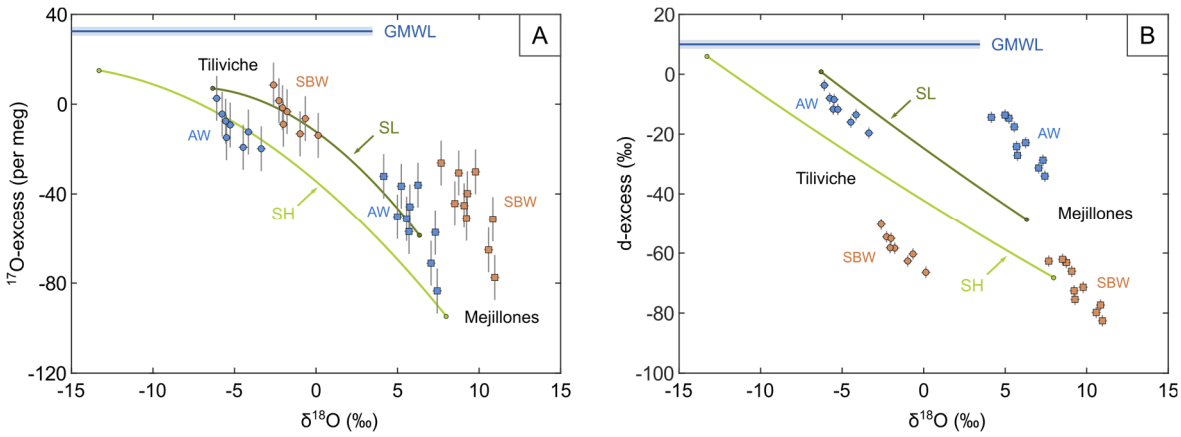

Figure 6.4: Oxygen (A) and hydrogen (B) isotope data of ambient water (AW, blue) and structurally bonded water (SBW, brown) of gypsum deposits from Mejillones (squares) and Tiliviche (circles). The solid lines represent evaporation trajectories for recent salt lake systems in northern Chile in the central hyperarid part of the Atacama Desert – Salar de Llamará (SL, dark green) – and in the semiarid high-altitude Altiplano region – Salar del Huasco (SH, light green). Model input parameters are: Salar de Llamará: T = 23°C, h = 43 %, n = 0.5, $\delta^{18}O_{WI}$ = -6.295 ‰, ^{17}O-excess$_{WI}$ = 7 per meg, d-excess$_{WI}$ = 0.8 ‰, $\delta^{18}O_V$ = -15.3 ‰, ^{17}O-excess$_V$ = 7 per meg, d-excess$_V$ = 0.8 ‰; Salar del Huasco: T = 6°C, h = 23 %, n = 0.5, $\delta^{18}O_{WI}$ = -13.284 ‰, ^{17}O-excess$_{WI}$ = 15 per meg, d-excess$_{WI}$ = 6.0 ‰, $\delta^{18}O_V$ = -19.6 ‰, ^{17}O-excess$_V$ = 18 per meg, d-excess$_V$ = 30 ‰. The Global Meteoric Water Line (GMWL) is shown as reference.

6.7 Discussion

6.7.1 Preservation of primary isotope signatures in SBW of gypsum

The isotopic composition of paleo-lake water determined from SBW of gypsum from Mejillones and Tiliviche follow distinct trends of increasing $\delta^{18}O_{AW}$ with decreasing d-excess$_{AW}$ and ^{17}O-excess$_{AW}$ as it is expected for water undergoing evaporation (Fig. 6.4). The evaporation trends in samples from Mejillones and Tiliviche are clearly distinguishable and strongly differ from that observed in presently active salt lake systems in northern Chile (Fig. 6.4) indicating the preservation of the primary isotope signature of the paleo-lake in SBW of gypsum. Post-formation alteration by isotopic exchange reactions as it is evident for recrystallized gypsum (Sofer, 1978) seems unlikely considering the large cm-sized and well preserved gypsum crystals studied herein.

The different shape of evaporation trend lines reflects hydrologic ($\delta^{18}O_{WI}$) and environmental conditions (mainly h) during evaporation that are specific for each individual site. The isotopic composition of inflow water defines the starting point of the evaporation trajectory. Both the *Salar de Llamará* and the *Salar del Huasco* are mainly fed by groundwater. The isotopic composition of groundwater ($\delta^{18}O_{WI}$) at Salar del Huasco is more depleted compared to Salar de Llamará mainly due to its location at greater distance from the coast and at higher altitude (cf. Fig 6.1). For Tiliviche, the isotopic composition of paleo-lake water supports meteoric origin of inflow water with $\delta^{18}O_{WI}$

between -10 and -6 ‰ (Fig. 6.4). This range is comparable to modern groundwaters and rivers in the northern part of the Atacama Desert (Aravena, 1995) and coincides well with the present-day isotopic composition of *Quebrada Tiliviche* ($\delta^{18}O$= -9.0 ‰) and *Quebrada Aroma* ($\delta^{18}O$ = -7.3 ‰), whose proto-streams probably contributed to the Tiliviche paleo-lake. In contrast, $\delta^{18}O_{AW}$ values > 0 ‰ observed in samples from Mejillones (Fig. 6.4) indicate that these gypsum crystals precipitated from evaporated seawater. This is consistent with the coastal position of the site (130 m asl) and the proposed marine origin of gypsum deposits on the Mejillones Peninsula (Di Celma et al., 2014).

Prevailing arid conditions at both *Salar de Llamará* (mean annual h = 56 %) and *Salar del Huasco* (mean annual h = 34 %) cause a relatively flat shape of local evaporation trajectories in triple oxygen isotope space (Fig. 6.4a). In comparison, the triple oxygen evaporation trends captured in SBW of lacustrine gypsum of both Tiliviche and Mejillones are relatively steep (Fig. 6.4a). Since, in triple oxygen isotppe space, the curvature of the trajectory increases with increasing humidity, this may be a first indication of more humid conditions during gypsum formation at both sites. High humidity is reasonable for the coastal Mejillones site, which is today characterized by mean annual relative humidity of 70 % with low diurnal variability between 60 and 80 %. Due to the proximity to the sea, broadly similar or even higher relative humidity is reasonable for the presumed time of gypsum precipitation. The Tiliviche site is also located close to coast (10 km distance) but at higher altitude (900 m asl) in the westernmost part of the Central Depression. Humidity in austral summer (~ 20 %) is comparable to present conditions in the hyperarid core of the Atacama Desert. In austral winter, fog is frequently advected from the Pacific Ocean (Schween et al., 2020) providing moisture to the site. However, mean annual humidity is still 50 %, much lower than at Mejillones. Thus, the steep isotopic evaporation trend in the plot of ^{17}O-excess over $\delta^{18}O$ (Fig. 6.4a) may indicate that the climatic conditions at the time of gypsum formation at Tiliviche had been more humid compared to present climate. To investigate these hypotheses, past changes in relative humidity are quantitatively modeled by fitting the isotopic data to the C-G equation.

6.7.2 Paleo-humidity reconstruction in the Atacama Desert

The range of model inputs for Mejillones and Tiliviche was defined based on the location of the deposits (coastal/continental, low/high altitude, etc.), modern ranges of input variables and their potential to change in the past (Table 6.2 and 6.3). A detailed description on how individual input parameters are approximated is provided as supplementary material (see appendix 2). Relative humidity and temperature were considered as free variables.

6.7.2.1 Mejillones

Modelling isotopic data from Mejillones with parameters as defined in Table 6.2 implies h = 65.5 ± 1.2 % and T = 20.0 ± 1.4°C (Fig. 6.5). Today, the relative humidity at Mejillones is mainly controlled by the nearby Pacific Ocean. As the gypsum deposits on the Mejillones Peninsula precipitated from evaporated seawater (Di Celma et al., 2014), it is likely that humid conditions will also have prevailed at the time of gypsum formation (roughly between 5.3–0.8 Ma; Di Celma et al., 2014). Hence, a model output h of 65 % seems reasonable. The model output temperature is slightly higher than the present mean annual temperature of 16°C at Mejillones. However, the modeled temperature may be more representative of the conditions during active gypsum precipitation. In the afternoon hours between 14:00 and 18:00, when evaporation is strongest, modern mean annual temperatures average to 18 ± 3°C, which agrees well with the model results. Thus, the climatic conditions at Mejillones during gypsum formation in the Plio-Pleistocene were probably similar to present climate.

Table 6.2: Model input parameters for Mejillones.

variable	input	output
rH (%)	0 – 100	65.5 ± 1.2
T (°C)	0 – 40	20.0 ± 1.4
wind	0.4 – 0.6	0.6 ± 0.0
$\delta^{18}O_{WI}$ (‰)	-1 – 1	1.0 ± 0.0
$^{17}O\text{-excess}_{WI}$ (per meg)	-5	-
$d\text{-excess}_{WI}$ (‰)	0	-
$\delta^{18}O_{V}$ (‰)	-12.5 – -9.5	-12.5 ± 0.1
$^{17}O\text{-excess}_{V}$ (per meg)	-5 – 15	-5 ± 0
$d\text{-excess}_{V}$ (‰)	0 – 10	10 ± 0
E/I_{max}	1.2	-

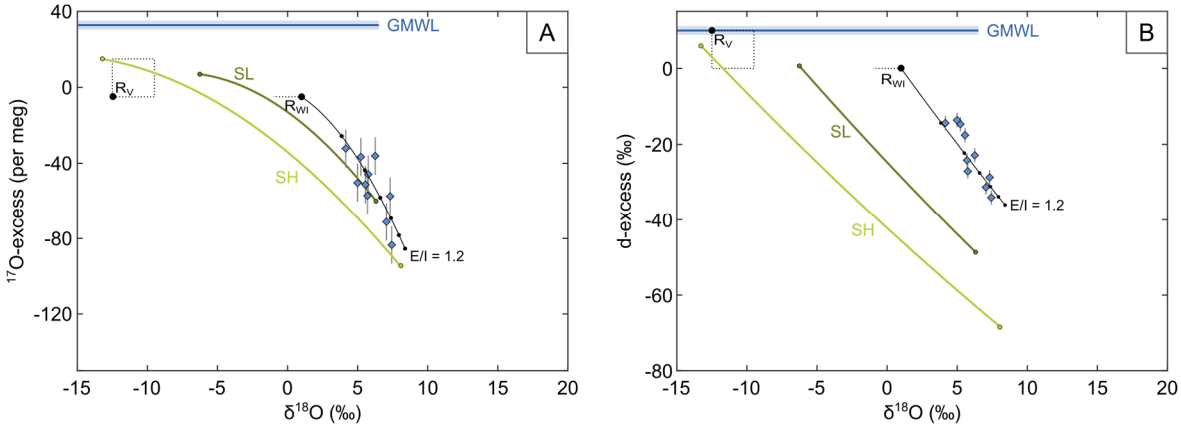

Figure 6.5: Model results for Mejillones in ^{17}O-excess vs δ^{18}O (A) and d-excess vs δ^{18}O (B). Blue diamonds represent the isotopic composition of paleo-lake water derived from SBW of gypsum crystals from Mejillones. The solid line shows best fit model solution for input parameters as defined in Table 6.1. Black dots along the black line indicated steady states for different E/I in steps of 0.2. R_V and R_{WI} represent model outputs for the isotopic composition of atmospheric vapor and inflowing water within the defined input range (dashed line/rectangle). Evaporation trajectories in recent lake systems of Salar de Llamará (SL; dark green) and Salar del Huasco (SH, light green) are shown for comparison.

6.7.2.2 Tiliviche

Modelling isotopic data from Tiliviche implies a relative humidity between 66 and 81 % and warmer than present climate (see Table 6.3). More humid conditions compared to today seem reasonable considering that gypsum deposition in the Tiliviche paleo-lake occurred during the Pliocene warm period around 3.5 Ma ago – a time that is generally assumed to be characterized by wetter than present climate (Salzmann et al., 2011). Higher sea surface temperatures in the eastern Pacific and a weaker Walker circulation associated with permanent El-Niño like conditions may have led to a weakening of the temperature inversion layer over the Pacific Ocean (Wara et al., 2005; de Wet et al., 2015). This may have increased moisture uptake from the Pacific Ocean and its transport over the Coastal Cordillera, leading to increased precipitation in the Central Depression of the Atacama Desert.

However, all of the four modelling scenarios for Tiliviche generate some unexpected output. When input parameters are restricted in a reasonable range, the model gives unreasonably high temperatures at its upper limit 40°C (scenario 1 in Table 6.3; black curve in Fig. 6.6). Certain combinations of fixed input parameters (e.g. with lower T and higher $\delta^{18}O_{WI}$) generate flatter curves that do not seem to match the measured data (scenario 2 + 3 in Table 6.3, red curves in Fig. 6.6).

The general flatness of modeled evaporation trajectories is caused by the low isotopic difference between inflowing water and atmospheric vapor. Tolerating lower $\delta^{18}O_V$ values up to -20 ‰ results

in a better fit to isotopic data (scenario 4 in Table 6.3, grey curve in Fig. 6.6). The model output humidity of h = 69.4 ± 5.0 % is within the range of previous scenarios, however, the temperature of T = 29.5 ± 5.9°C is still relatively high. We could speculate that such low $\delta^{18}O_V$ values (or even lower) may be achieved if easterly air masses that were transported a long way from the Atlantic Ocean over the Andes to the Atacama Desert have dominated atmospheric vapor at the Tiliviche site during gypsum formation. However, there is no evidence for this. Hence, other hydrological processes that may have influenced the isotopic composition of the paleo-lake need to be investigated.

Table 6.3: Model input parameters for Tiliviche.

	scenario 1		**scenario 2**		**scenario 3**		**scenario 4**	
variable	**Input**	**Output**	**Input**	**Output**	**Input**	**Output**	**Input**	**Output**
rH (%)	0 – 100	82 ± 1	0 – 100	66 ± 5	0 – 100	77 ± 1	0 – 100	69 ± 5
T (°C)	0 – 40	40 ± 0	15 – 25	25 ± 0	15 – 25	25 ± 0	0 – 40	30 ± 6
wind	0.4 - 0.6	0.6 ± 0	0.4 -0.6	0.6 ± 0	0.4 -0.6	0.6 ± 0	0.4 – 0.6	0.5 ± 0.0
$\delta^{18}O_{WI}$ (‰)	-12 – -6	-11.2 ± 0.6	-12 – -6	-12 ± 0.0	-8.5	-	-12 – -6	-8.6 ± 0.5
^{17}O-excess$_{WI}$ (per meg)	20	-	20	-	20	-	20	-
d-excess$_{WI}$ (‰)	10	-	10	-	10	-	10	-
$\delta^{18}O_V$ (‰)	-15 – -12	-15 ± 0	-15 – -12	-15 ± 0	-15 – -12	-15 ± 0	-20 – -12	-20 ± 0
^{17}O-excess$_V$ (per meg)	5 – 25	5 ± 0	5 – 25	5 ± 0	5 – 25	5 ± 0	5 – 25	16 ± 6
d-excess$_V$ (‰)	10 – 20	10 ± 2	10 – 20	17 ± 4	10 – 20	10 ± 0	10 – 20	16 ± 4
E/I_{max}	1.2	-	1.2	-	1.2	-	1.2	-

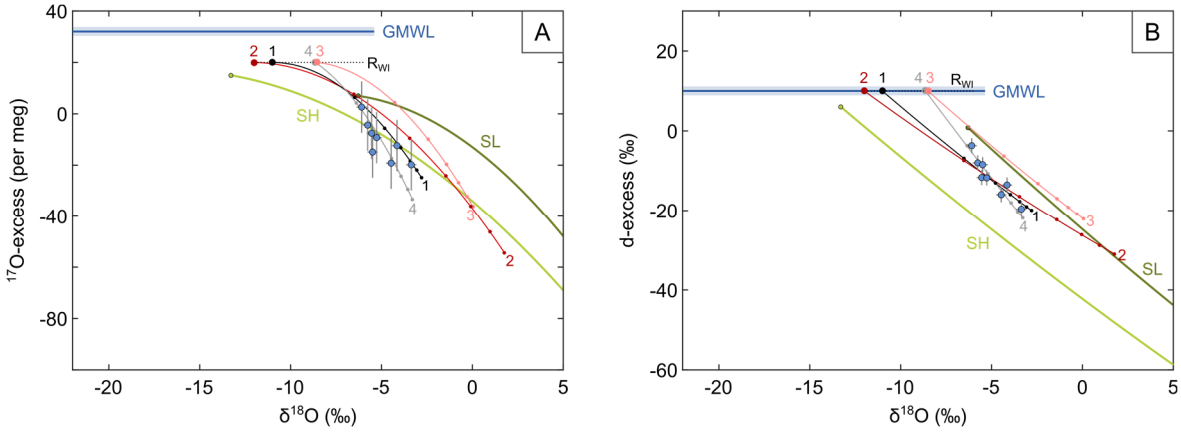

Figure 6.6: Model results for Tiliviche in ^{17}O-excess vs $\delta^{18}O$ (A) and d-excess vs $\delta^{18}O$ (B). Blue circles represent the isotopic composition of paleo-lake water determined from SBW of gypsum crystals from Tiliviche. Solid lines show best fit model solutions for different input scenarios indicated by small numbers (Table 6.3). Evaporation trajectories in recent lake systems of Salar de Llamará (SL; dark green) and Salar del Huasco (SH, light green) are shown for comparison.

Table 6.4: Model input parameters for Salar del Huasco.

variable	input	output
rH (%)	0 – 100	44.9 ± 1.6
T (°C)	0 – 40	9.1 ± 1.4
wind	0.4 – 0.6	0.60 ± 0.02
$\delta^{18}O_{WI}$ (‰)	-13.284	-
$^{17}O\text{-excess}_{WI}$ (per meg)	15	-
$d\text{-excess}_{WI}$ (‰)	6.0	-
$\delta^{18}O_{V}$ (‰)	-21 – -19	-21 ± 0.0
$^{17}O\text{-excess}_{V}$ (per meg)	30	-
$d\text{-excess}_{V}$ (‰)	10	-
E/I_{max}	1.2	-

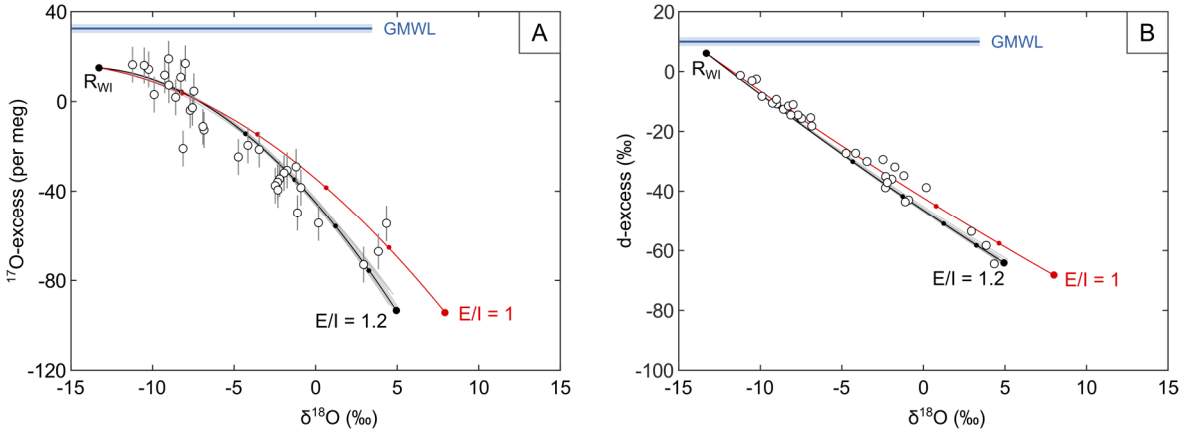

Figure 6.7: Fitting the C-G model to quantify humidity at Salar del Huasco based on isotopic data of pond waters (white circles; for data see Chapter 5). The red curve represents the modeled recharge evaporation trajectory using seasonal average climatic conditions (h = 23 %, T = 6°C, n = 0.54, $\delta^{18}O_{WI}$ = -13.284 ‰, $^{17}O\text{-excess}_{WI}$ = 15 per meg, $d\text{-excess}_{WI}$ = 6.0 ‰, $\delta^{18}O_{V}$ = -19.6 ‰, $^{17}O\text{-excess}_{V}$ = 18 per meg, $d\text{-excess}_{V}$ = 30 ‰). The black curve shows the mean of best fit model solutions (grey lines) that satisfy both ^{17}O-excess vs δ^{18}O and d-excess vs δ^{18}O. Model input parameters are summarized in Table 6.2. Small dots along the lines indicate steady states for different E/I in steps of 0.2.

As shown in the previous study of this thesis at the Salar del Huasco (Chapter 5), mixing processes associated with flooding events can temporarily shift the isotopic composition of lakes below modeled recharge evaporation trajectories in triple oxygen isotope space. Episodic flooding, e.g. due to a frequent occurrence of precipitation in the catchment area during more humid periods in the past, may result in an apparently permanent shift of the lake's isotopic composition below the predicted evaporation trajectory. Modelling the isotopic composition of ponds and lakes from the Salar del Huasco results in a trajectory that principally fits the measured pond data (Fig. 6.7) but the modeled relative humidity of h = 44.9 ± 1.6 % is too high compared to the observed mean of 23 % for the Salar del Huasco site. Modeled pond data from Salar del Huasco imply that such mixing

processes could bias model output results by at least 20 % to higher values. Similarly, humidity values for the Tiliviche site may be overestimated due to potential mixing processes in the Tiliviche paleo-lake that are not accounted for in the model.

6.7.3 Limitations of the C -G model to reconstruct paleo-humidity

The modeled relative humidity is relatively insensitive to changes in $\delta^{18}O_{WI}$ or to changes in temperature (Fig. A2.3 and A2.4). A slight dependence is observed between the model output humidity and $\delta^{18}O_V$. The model tends to produce lower relative humidity with decreasing $\delta^{18}O_V$. Furthermore, changes in the turbulence coefficient n and restrictions of the E/I ratio can significantly affect the modeled relative humidity. Both the turbulence coefficient n and E/I have a major impact on the length of the curvature (Fig. 6.8). Lowering n and E/I reduces the length of the trajectory (Fig. 6.8). As the length of the trajectory increases with decreasing humidity (Fig. 6.8), the model gives lower relative humidity when n and E/I are restricted to lower values. In preliminary models $E/I_{max} = 1$ was employed together with a turbulence coefficient n = 0.5. Using these parameters for Mejillones results in unreasonably low humidity of 53.0 ± 2.5 % and unrealistic high temperatures of T = 37.5 ± 2.8°C. The modeled trajectory does not fit the measured isotopic data in triple oxygen isotope space implying that the model input parameters for E/I_{max} and n need to be relaxed to some degree. For Tiliviche as well as for Salar de Llamará, strictly restricting E/I_{max} to 1 and n to 0.5 do not significantly affect the model output.

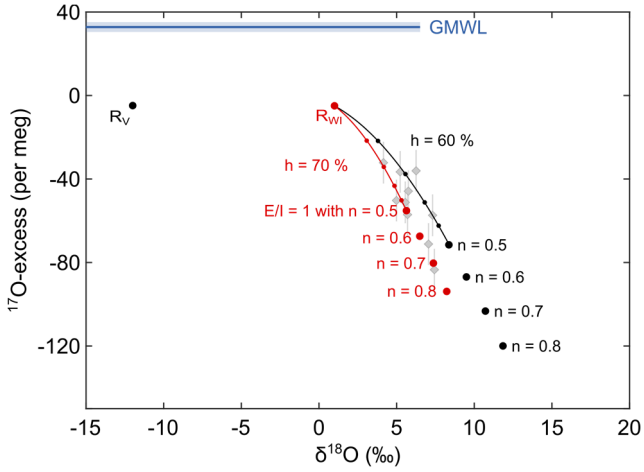

Figure 6.8: Sensitivity of evaporation trajectories in triple oxygen isotope space to relative humidity, E/I and the turbulence coefficient. Solid lines represent evaporation trajectories modeled for relative humidity of 60 % (black) and 70 % (red) with $E/I_{max} = 1$. Small circles on the line indicate different hydrologically steady-states at variable E/I (0.2, 0.4, 0.6 and 0.8). Large circles represent the isotopic composition of a terminal lake (E/I = 1) at variable turbulence coefficient n as indicated by numbers. Shaded symbols indicate the isotopic composition of paleo-water determined from gypsum deposits at Mejillones.

6.8 Conclusion

In this study, we investigated the potential of isotope analyses of SBW of lacustrine gypsum to quantify past changes in relative humidity in the Atacama Desert. Hydrogen and triple oxygen isotopes of SBW of gypsum fall on characteristic evaporation trends confirming the principal applicability of the C-G model to quantify paleo-humidity conditions. The model output humidity is less affected by changes in the isotopic composition of source water δ_{WI} and atmospheric vapor δ_V, but can strongly depend on the selected turbulence coefficient n and the limitations of E/I. The uncertainty in the derived paleo-humidity is limited by the discrimination of evaporation trajectories for different humidity that mainly depends on the isotopic difference between source water δ_{WI} and atmospheric vapor δ_V.

Modelling of gypsum deposits of Pliocene to Mid-Pleistocene age from the Mejillones Peninsula located close to coast in the southern part of the Atacama Desert results in relative humidities around 65 %, which is comparable to present climate. The isotopic composition of paleo-lake water derived from gypsum deposits from the northern part of Atacama Desert (Tiliviche) indicate humid conditions in Pliocene times with relative humidity between 65-80 %. Gypsum deposition occurred about 3.5 Ma ago coinciding with the Early Pliocene warm period (4.5–3.0 Ma ago), where permanent El Niño-like conditions may have contributed to the frequent occurrence of precipitation events not only in the adjacent Altiplano but also in presently hyperarid regions of the Atacama Desert. However, the model did not satisfy both ^{17}O-excess and d-excess for any reasonable set of input parameters implying that the paleo-lake may have been affected by mixing processes, e.g. due to the frequent occurrence of precipitation and flooding. In this case, the estimates of 65-80 % represent maximum values.

7 The spatial distribution of soluble salts in Atacama Desert soils and their relationship to hyperaridity

Voigt, C., Klipsch, S., Herwartz, D., Chong, G., and Staubwasser, M., 2020. The spatial distribution of soluble salts in the surface soil of the Atacama Desert and their relationship to hyperaridity. Glob. Planet. Change, 184, 103077. https://doi.org/10.1016/j.gloplacha.2019.103077.

7.1 Introduction

The Atacama Desert is one of the driest and oldest deserts on Earth (McKay et al., 2003; Dunai et al., 2005; Evenstar et al., 2017). Running from west to east the major tectonic provinces are the Coastal Cordillera, the Central Depression, the Precordillera and the Western Cordillera of the high Andes (Fig. 7.1). The long distance to eastern moisture sources (Amazonia, Atlantic), the rain shadow effect cast by both Cordilleras and the combination of the cold coast-parallel Humboldt Current along with subtropical subsidence of air induced by the Hadley circulation severely restrict moisture transport to the Atacama (Hartley and Chong, 2002; Houston and Hartley, 2003). Aridity broadly increases northwards between 25 and 19°S and eastwards to the Precordillera – which receives some moisture because of its altitude – and to the Coastal Cordillera in the West (Fig. 7.1). Under hyperarid conditions, common soil formation through biologic activity and silicate weathering ceases, and the deposition of dust and atmospheric salts become the dominant processes (Rech et al., 2003; Ewing et al., 2006). Hyperarid "desert" soil deposits of the Atacama primarily consist of gypsum and anhydrite, with variable content of unweathered silicates and highly soluble salts such as chlorides and nitrates (Ericksen, 1983; Rech et al., 2003; Michalski et al., 2004; Ewing et al., 2006; Wang et al., 2014). The nitrate deposits in the Atacama represent the largest accumulation of such salts worldwide (Ericksen, 1981, 1983). The preservation of highly soluble salts requires long-term hyperarid conditions. However, despite having been investigated for over a century for mining purposes, the spatial distribution of the main salts in the Atacama Desert soil has not been documented in the scientific literature. Equally, the relationship between salt accumulation and hyperaridity is commonly presumed but remains underdefined, particularly in relationship to the regional tectonic and geomorphologic setting.

The sources of soluble salts in Atacama soils have been debated for more than a century (e.g. Darwin, 1839; Ericksen, 1983; Chong, 1994; Bao et al., 2004; Michalski et al., 2004; Wang et al., 2014; Reich and Bao, 2018). The principal sources include: (1) sea spray from the Pacific Ocean, (2) weathering of Andean volcanic rocks, (3) direct deposition from local volcanic emissions, (4) erosion and redeposition from playas and salars, and – particularly important for nitrates – (5) photochemical reactions in the atmosphere and subsequent deposition (Ericksen, 1981, 1983; Rech et al., 2003; Bao et al., 2004; Michalski et al., 2004; Wang et al., 2014).

After > 200 years of nitrate mining, only a few pristine near surface deposits are preserved. An idealized soil profile for the nitrate mining regions of the Atacama Desert consists of five distinct layers (Ericksen, 1981). The surface horizon, *chuca*, is 10 to 30 cm thick and primarily formed by powdery to poorly cemented gypsum and anhydrite with variable amounts of silt, sand, and gravels. Often, *chuca* is covered by a thin gypsiferous crust. At the base of this layer, an up to a few tens of cm thick white saline horizon of highly soluble sulfate minerals such as thenardite (Na_2SO_4), bloedite ($Na_2Mg[SO_4]_2 \cdot 4H_2O$), epsomite ($MgSO_4 \cdot 7H_2O$), and humberstonite ($K_3Na_7Mg_2[NO_3(SO_4)_3]_2 \cdot 6H_2O$) may occur locally (Ericksen, 1981, 1983). The *chuca* changes gradually downward into the *costra*, a 0.5–2 m thick layer of moderately to firmly cemented gypsum and anhydrite, generally with a nodular texture at the transition. Underneath the *costra* follows the *caliche*, an up to 5 m thick layer of firmly cemented halite and, in some areas, with up to 0.5 m thick lateral veins of nitratine. Beneath the *caliche* follows either salt-cemented (*conjelo*) or loose unconsolidated (*coba*) regolith. In the Central Depression in particular, but also in local basins with past or present groundwater near the surface, playa deposits (*salars*) with salt-cemented crusts and halite nodules may cover large areas (Ericksen, 1981, 1983). When active, these *salars* continue to grow by evaporation and salt precipitation from the subsurface water table, thereby concentrating the most soluble salts at the surface (Finstad et al., 2016). The *salar*-deposits are, however, not the object of this investigation.

The objective of this study is to systematically investigate the spatial distribution and abundance of soluble salts in surface and near-surface soil deposits of the Atacama Desert. We seek to document the interplay between sources, deposition, and preservation of main salts in order to identify long-term gradients of hyperaridity. For that purpose, we analyzed soil samples of poorly cemented thin surface crusts, powdery *chuca*, and subsurface concretions from the transition to the *costra* along latitudinal and longitudinal transects between 19–25°S and 68.5–70.5°W. The results presented

here identify the regions between approximately 19 and 22°S as the hyperarid core of the Atacama Desert and highlight moisture-related processes of redistribution and post-depositional phase transformation of the main salts in Atacama Desert soils.

7.2 Study Area

The Atacama Desert is characterized by four major N-S trending morphotectonic units (from west to east): The Coastal Cordillera with altitudes generally below 2000 m, the Central Depression at an average altitude around 1000 m, followed eastwards by the Precordillera and the Western Cordillera with altitudes in excess of 4000 m and some peaks over 6000 m (Fig. 7.1; Ericksen, 1981). The Coastal Cordillera consists of Jurassic-Cretaceous andesitic volcanic rocks, Jurassic-Cretaceous marine sediments and some continental conglomerates (Allmendinger and González, 2010). The western margin of this mountain range forms a prominent coastal cliff with heights up to 1000 m. The Central Depression is a tectonic forearc basin with a base of Paleogene volcanics.

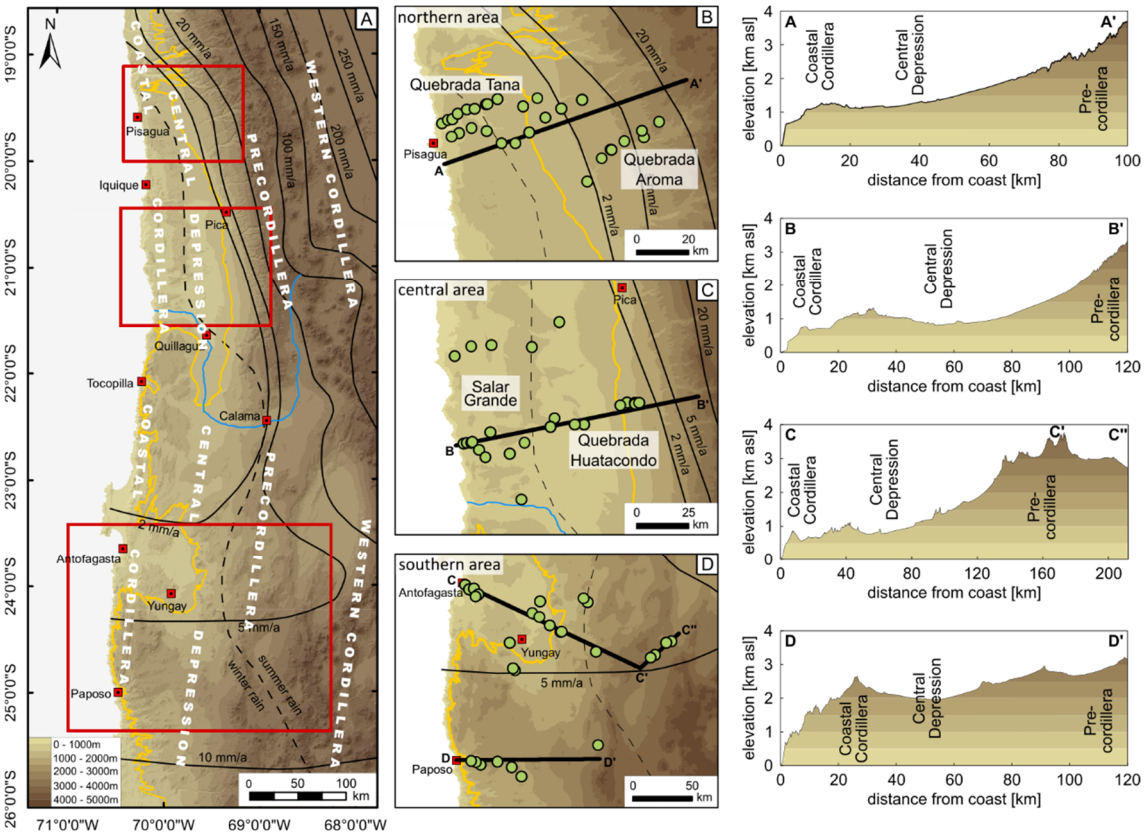

Figure 7.1: Color-shaded digital elevation model (derived from SRTM data, created using ArcGIS 10.5.1) with isohyets (solid black lines; Houston, 2006). Dashed black line marks the border between areas dominated by summer and winter rainfall (Houston, 2006). The maximum extension of fog penetrating inland is approximately equal to 1200 m (solid yellow line; Cereceda et al., 2008). Red frames indicate the southern, central and northern focus areas shown in detail in panels B-D. Green dots mark sampling sites. Topographic profiles A-D indicated in panel B-D are shown to the right.

The basin is filled with a few hundred meters of late Cenozoic fluvial and lacustrine sediments (Hartley et al., 2000; Hartley and Evenstar, 2010; Jordan et al., 2014). Alluvial fan deposits derived from mountain catchments in the Precordillera cover wide areas of the Central Depression (Jordan et al., 2014). The Precordillera consists of uplifted sediments and volcanic intrusion dating back to the Middle Paleozoic, folded into a series of monoclines and westward propagating thrust fronts (Garcia and Hérail, 2005). The Western Cordillera represents the presently active volcanic arc, with rhyolithic volcanics dating back to the Miocene (Karátson et al., 2012).

The Atacama Desert (18–27°S, 0–3500 m) is characterized by long-term arid climatic conditions with decades of absolute drought (e.g. Ericksen, 1981; Rech et al., 2003; Dunai et al., 2005; Houston, 2006; Evenstar et al., 2017). Mean annual precipitation over the Precordillera, the Central Depression and the Coastal Cordillera is <10 $mm \cdot a^{-1}$ (Fig. 7.1; Houston and Hartley, 2003). Hyperaridity with < 2 $mm \cdot a^{-1}$ mean annual precipitation occurs between 19 and 23.5°S, including most parts of the Central Depression (Houston, 2006). This zone of hyperaridity is associated with the boundary between summer and winter rainfall provided by two sources (Houston, 2006). Summer precipitation originates from easterly airflow out of the Amazon basin, but downstream behind the Andes a rain shadow develops westwards of the Western Cordillera, covering the Precordillera, the Central Depression, and the Coastal Cordillera. Along the western slope of the Precordillera mean annual precipitation decreases from 120 $mm \cdot a^{-1}$ at 4000 m to < 0.5 $mm \cdot a^{-1}$ at 1000 m (Houston and Hartley, 2003). During winter, (south)westerly airflows from the Pacific Ocean may cause frontal precipitation from extratropical cyclone systems in coastal areas and the southern part of the Atacama Desert (south of 24°S; Houston, 2006). Rainfall in the Central Depression from these sources is extremely rare, but flooding may result from sporadic rainfall in the Western Cordillera and the Precordillera, as has been mentioned in mining companies' reports since the late 19th century (Ericksen, 1981). In most recent times, unusual heavy rainfall events occurred in parts of the (hyper)arid Atacama Desert that may be associated with El Niño conditions, cold-front winter storms and anomalous warm equatorial Pacific Ocean temperatures (Jordan et al., 2019).

Besides rare precipitation, coastal areas sporadically receive moisture by fog (*camanchaca*) from low stratocumulus clouds expanding from the Pacific Ocean (Cereceda et al., 2002, 2008). Advection of fog further inland may occur locally through valleys in the Coastal Cordillera. Fog typically occurs between 650 and 1200 m based on cloud height data of stratocumulus clouds at the

coast and the presence of *Tillandsia sp.* vegetation (Cereceda et al., 2008). In the Central Depression, fog may also occur due to condensation of atmospheric vapor as a result of the strong temperature decrease at night (Cereceda et al., 2008).

7.3 Sampling and methods

7.3.1 Sample locations

About 150 soil samples were collected between 2017 and 2019 along several W-E transects between 19 and 25°S from three focus areas, generally covering the Coastal Cordillera, the Central Depression, and the Precordillera (Fig. 7.1).

The northern focus area is located between 19°20′ and 19°50′S (Fig. 7.1a). In the southern part of the area (south of 19°35′S), the Central Depression is endorheic, collecting all runoff and sediment from the Precordillera. To the north, most water from the Precordillera flows into the Pacific Ocean through a series of deep canyons (*quebradas*) intersecting the Central Depression and the Coastal Cordillera. Alluvial fans form the western slope of the Precordillera and cover large parts of the Central Depression. Samples were taken in the Coastal Cordillera along the canyon rim of *Quebrada Tana* ranging between 900 and 1000 m in elevation (Fig. 7.1b). The sample transect extends onto alluvial fan surfaces in the Central Depression. A second transect from the Central Depression into the Precordillera was sampled along Quebrada Aroma (Fig. 7.1b). These samples range between 1400 and 2700 m with increasing mean annual precipitation from < 0.5 $mm \cdot a^{-1}$ to 25 $mm \cdot a^{-1}$ with increasing elevation (Houston and Hartley, 2003). Sparse vegetation occurs in the highest parts of the transect (Jordan et al., 2014).

The central focus area is located between 20°30′ and 21°30′S (Fig. 7.1a). Here, the Central Depression is endorheic except in the southernmost part, where the Rio Loa river incised a deep canyon through the Coastal Cordillera to the Pacific Ocean. Like in the northern area, large parts of the Central Depression are covered by alluvial fans extending from the western flank of the Precordillera. In the western part of the Central Depression, just north of the *Rio Loa* river, there is an active salt lake system – the *Salar de Llamará*. Further to the west lies the uplifted, fossil *Salar Grande*. Samples were collected along two transects south and north of *Salar Grande* (Fig. 7.1c). Samples from the southern transect range between 375 and 900 m, while sampling sites along the northern transect are located between 500 and 1000 m (Fig. 7.1c). The southern transect extends towards the Precordillera on alluvial fan surfaces along *Quebrada Huatacondo* to 1640 m.

The southern focus area is located between 23°30′ and 25°10′S (Fig. 7.1a). The Central Depression is largely missing in this area. There are no valleys connecting the Precordillera and the Pacific Ocean. Some catchments originating in the Coastal Cordillera incise deep into the hinterland. A few large endorheic basins are situated in local tectonic basins between the Precordillera and the Altiplano (e.g. *Salar de Atacama* and *Salar Punta Negra*). Samples were collected along a transect starting south of Antofagasta and reaching over 200 km inland (Fig. 7.1d). Here, the majority of the Coastal Cordillera does not exceed 950 m and fog may penetrate far into the hinterland. Elevations above 1200 m, which mark the maximum extension of the advective fog zone (Cereceda et al., 2008), are reached at about 90 km distance from the coast. The transect extends into the Precordillera to elevations of up to 3100 m (Fig. 7.1d). Mean annual precipitation increases with elevation to about 40 $mm \cdot a^{-1}$ at 3000 m (Houston and Hartley, 2003). A second transect was collected south of Paposo in the southern part of the southern focus area (Fig. 7.1d). This region receives slightly higher mean annual precipitation of 5–10 $mm \cdot a^{-1}$ (Houston, 2006). Samples were taken on hillslopes along fluvial channels between elevations of 1200 and 2100 m. At lower altitudes (900–1200 m) no surface crusts and gypsic subsurface horizons were found.

7.3.2 Sampling strategy

Gypsic soils were sampled along shallow depth profiles from ridges or some form of geomorphic elevation to minimize unwanted sampling of material redistributed by flowing water. Sampling from elevated locations could not always be enacted strictly within the Central Depression, particularly on the gently sloping distal fans protruding from the Precordillera. Salars, old playa lake surfaces, and channel beds were not sampled. Even though the generalized profile (Ericksen, 1981) may not represent the entirety of our profile sampling in this study, the *chuca* and the gradient into the uppermost *costra* is a reasonably accurate template for the majority of our sample profiles. When present, thin gypsiferous surface crusts with maximum thickness of about 0.5 cm were sampled separately. These crusts typically cover the powdery and uncemented *chuca* layer and are generally very friable. Where the thin surface crust was absent, we sampled the powdery *chuca*. These crusts and *chuca* samples are referred to as "surface samples" throughout this study.

The subsurface sample set consists of concretions and gypsic layers collected from the uppermost *costra* between 10 and 40 cm soil depth. These concretions may be only slightly consolidated, consist of intergrown crystals or be massive and hard. Their formation is related to leaching and

reprecipitation processes within the soil (Ericksen, 1981; Rech et al., 2003). These samples are referred to as "subsurface concretions" throughout the study.

In some places, hard and spheroidal concretions very similar to that described above, crop out at the surface. They are sometimes embedded in residual *chuca* material and thus, were probably formed initially in the *costra*, but brought to the surface by deflation or local fluvial erosion of the overlying uncemented *chuca*. Throughout this study, these are referred to as "surface concretions". Detailed pictures of the different sample types are shown in the appendix (Fig. A3.1).

7.3.3 Analytical methods

Soil samples were characterized chemically and mineralogically by total soil chemical analysis (ICP-OES and spectrophotometric analysis) complemented by XRD and thermogravimetric analysis (TGA).

7.3.3.1 Mineral composition

Forty-eight representative samples were analyzed for their main mineral phases by powder X-ray diffraction at the University of Bonn. Samples were homogenized by grinding with mortar and pestle to a grain size of about 10 µm. X-ray diffraction patterns were obtained using a *Siemens D5000* diffractometer (Siemens AG, Munich, Germany) equipped with a 40-position sample holder, a coupled theta-theta goniometer and a scintillation detector. A *Siemens Kristalloflex 710D* X-ray generator was used, operating at a voltage of 40 kV and a filament current of 40 mA. The diffraction pattern was recorded between 4° and 70° theta angles with a step size of 0.02° per second at room temperature. The patterns were evaluated semi-quantitatively using the software package TOPAS (Bruker AXS GmbH, Karlsruhe, Germany).

7.3.3.2 Soluble salt ion concentration

Soluble salts were leached over 14 days with 10 ml of deionized water (18.2MΩ·cm) at 25°C from 100 mg of sediment. An additional time series leaching experiment of synthetic and natural gypsum and anhydrite confirmed full dissolution equilibrium after three days (see appendix, Fig. A3.2). The leaching solutions were analyzed by spectrophotometry for nitrate concentration following the method of Miranda et al. (2001). In brief, 180 µl of the leached sample solutions were loaded in a 96-well microplate (greiner bio-one). A 150 µl mixture of saturated VCl_3-solution (10 ml) and

Griess reagents, Sulfanilamide (1 ml) and N-(1-Naphtyl)ethylenediaminedihydro-chloride (1 ml), were added to each well. Following an incubation time of 60 min at 46°C the absorbance at 540 nm was measured with a *Thermo Scientific Multiskan GO* plate reader. The absence of matrix effects from dissolved major ions was confirmed with artificial solution mixtures. Accuracy and precision of measurements were controlled by a certified reference material (nitrate standard solution, Certipur, Merck) that reveals a long-term external reproducibility of about 5 $\mu mol \cdot l^{-1}$ (0.03 $mg \cdot g^{-1}$). Concentrations of Na, K, Mg, and Cl were analyzed in the leachate solution using a *SPECTRO ARCOS* ICP-OES with axial plasma observation (*SPECTRO Analytical Instruments*, Kleve, Germany). The operating parameters are specified in Table 7.1. Because calcium sulfate phases are dissolved to saturation in the leachates, Ca and S concentrations were not considered.

Table 7.1: Operating parameters for ICP-OES analyses.

Parameter	Setting
RF power	1400 W
Pump speed	30 rpm
Coolant gas flow	14.5 $l \cdot min^{-1}$
Auxiliary gas flow	1.3 $l \cdot min^{-1}$
Nebulizer gas flow	0.7 $l \cdot min^{-1}$
Spray chamber	Scott double pass
Nebulizer	Cross-flow
Torch	Quartz for axial view
Sample uptake	0.2 $ml \cdot min^{-1}$

7.3.3.3 Total sulfate concentration

Calcium sulfates from 100 mg of sediment were dissolved by quantitative reprecipitation overnight as $CaCO_3$ in 10 ml of a 0.01 $mol \cdot l^{-1}$ sodium carbonate solution at room temperature (Breit et al., 1985). Sulfate concentration in the supernatant solution was measured as total S by ICP-OES. This includes all sulfate from initially present calcium sulfates as well as sulfate from other easily soluble sulfates. Total dissolution of sulfate was verified by dissolution of $CaCO_3$ precipitation in 0.5M HCl and subsequent Ca concentration measurement by ICP-OES. Results reveal a 1:1 correlation between Ca and S for most of the samples suggesting that sulfate concentrations largely represent calcium sulfate contents with little contribution from easily soluble sulfates (see appendix, Fig. A3.3).

7.3.3.4 Water content

We obtained another independent estimate for total gypsum contents indirectly from thermogravimetric analyses. Gypsum ($CaSO_4 \cdot 2H_2O$) contains 20.9 wt-% structurally bonded water, which is lost by dehydration above a specific temperature (Christensen et al., 2008). We measured water loss by dehydration under controlled temperature conditions in a *TG 209 F1 Libra* (Netzsch, Selb, Germany) thermogravimetric analyzer (TGA). About 30 mg bulk sediment was heated up to 400 °C with a constant heating rate of 5 $K \cdot min^{-1}$. The temperature window of the two-step dehydration of gypsum to bassanite ($CaSO_4 \cdot 0.5H_2O$) and anhydrite ($CaSO_4$) was determined using pure gypsum powder and found to be between 75 and 200°C at the above heating rate. Reproducibility of water loss measurements in gypsum standards and in gypsum dominated natural samples was 0.2 %. If water loss in the temperature window determined above is dominated by the gypsum to anhydrite transition, water loss is proportional to the amount of gypsum initially present in the sample. We found a well-defined dehydration window for gypsum in the majority of samples (Fig. 7.2). Samples with low gypsum abundance tended to show a more complex dehydration behavior, mostly associated with large amounts of water loss below 75°C – either surface adsorbed water or water associated with clays – and occasionally due to other minerals dehydrating near the upper end of the temperature window (Fig. 7.3). In these cases, the temperature window used to quantify gypsum dehydration had to be adjusted. This was done based on well-defined features in the first differential of the dehydration pattern. In some cases, the presence of hydrated salts other than gypsum cannot be easily corrected for, as shown by the complex dehydration pattern of two samples in which the presence of polyhalite and pentahydrite was confirmed by XRD (Fig. 7.4). A detailed account on how gypsum abundance was quantified from TGA water loss measurements is outlined in section 7.4.2.2.

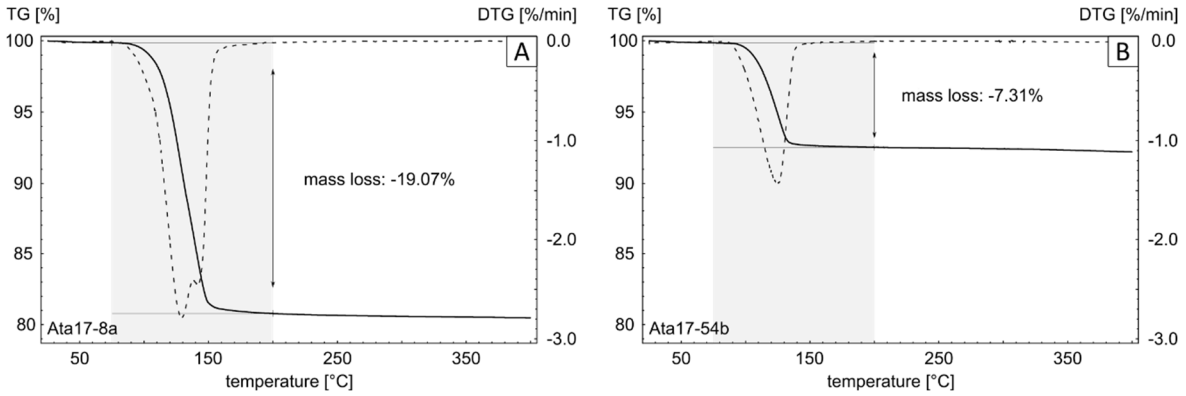

Figure 7.2: TGA profiles of selected bulk sediment samples. Mass loss determined between 75 and 200°C (grey bar) is only caused by the release of structurally bonded gypsum water. Solid line: mass loss, dashed line: first derivative function (change) of mass loss.

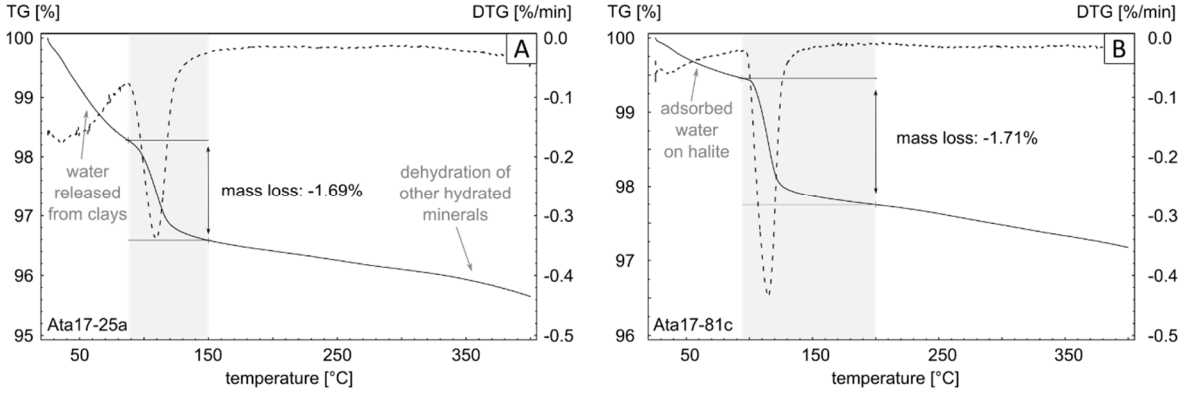

Figure 7.3: TGA profiles of selected bulk sediments. Temperature intervals were occasionally adjusted (grey bars) to minimize the contribution of water lost from other mineral phases than gypsum by minimizing overlap with the temperature window typical for loss of gypsum hydration water (75-200°C). When the window of mass loss from gypsum could not be clearly identified, samples were eliminated from the data set. A – Overlap of the temperature window typical for loss of gypsum hydration water with water released from clay minerals whose presence was identified by XRD analyses. B – The presence of about 40 wt-% halite, as indicated by XRD analyses, could account for the mass loss of adsorbed water below 100°C.

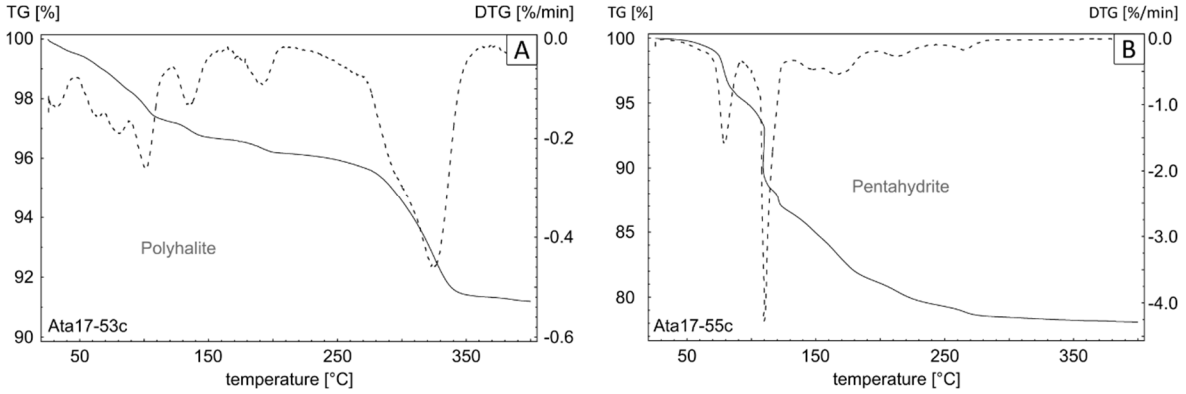

Figure 7.4: TGA profiles of polyhalite (A) and pentahydrite (B) as identified by XRD analyses. Both minerals show multi-phase water loss over the whole temperature range preventing the determination of water lost from gypsum.

7.3.3.5 Inorganic carbon content

Inorganic carbonate contents in soil samples were analyzed by a *LECO CS 225* C/N analyzer at the University of Cologne. Atacama Desert soils comprise very low inorganic carbonate contents, generally <1 $mg \cdot g^{-1}$. Only a few exceptions contain quantifiable amounts of up to 13 $mg \cdot g^{-1}$. From these analyses it can be concluded that $CaCO_3$ does not play a significant role in the salt budget of the Atacama Desert soil.

7.4 Results

7.4.1 Mineral composition

The majority of samples are dominated by gypsum, anhydrite, and halite. In a few samples, minor amounts (< 20 wt-%) of bassanite ($CaSO_4 \cdot 0.5H_2O$) and calcite (about 10 wt-%) are present. The highly soluble salts that could be identified in a few samples comprise thenardite (Na_2SO_4), glauberite ($CaNa_2[SO_4]_2$), bloedite ($Na_2Mg[SO_4]_2 \cdot 4H_2O$), nitratine ($NaNO_3$), polyhalite ($K_2Ca_2Mg[SO_4]_4$), and pentahydrate ($MgSO_4 \cdot 5H_2O$). The mineral suite is complemented by quartz, feldspars, and a low contribution of clay minerals. Silicates account for approximately 30 wt-% on average.

Gypsum is abundant in southern and coastal regions, while anhydrite becomes dominant towards the north and with increasing distance from the coast. Halite was identified in surface and subsurface samples in central and northern parts of the study area with generally low contents in surfaces (< 15 wt-%) but amounts as high as 82 wt-% in subsurface concretions. Clastic minerals – mainly feldspars and quartz – comprise low contents in subsurface concretions (~19 wt-%), while surface samples have distinctly higher clastic amounts (~45 wt-%).

Bassanite ($CaSO_4 \cdot 0.5H_2O$) and γ-anhydrite (soluble anhydrite, $CaSO_4$) are difficult to distinguish in XRD patterns due to their similar crystal structure. Both sulfate phases are formed by dehydration of gypsum (van Driessche et al., 2017), but formation temperatures of bassanite (45°C) and γ-anhydrite (> 100°C) (Seufert et al., 2009) suggest that the latter is not present in Atacama soil samples. While the formation temperature of bassanite may be reached in the uppermost *chuca* during daytime, daily average temperatures are well below.

7.4.2 Major ions

7.4.2.1 Sulfate

Atacama Desert soils are in most cases dominated by sulfate. Total sulfate contents vary between 0.3 and 562 $mg \cdot g^{-1}$. Most of the samples have sulfate concentrations > 200 $mg \cdot g^{-1}$. Sulfate concentrations of < 200 $mg \cdot g^{-1}$ are observed in surface samples on alluvial fans in the northern area and in high altitudes in the southern Precordillera (at ~3000 m). Subsurface concretions comprise low sulfate contents in samples along *Quebrada Tana* in the northern area. No distinct trend is visible in total sulfate with latitude or distance from coast. The spatial distribution of sulfate content in Atacama Desert soils is illustrated in the appendix (Fig. A3.4).

7.4.2.2 Water content and *gypsum/sulfate model ratios

Gypsum ($CaSO_4 \cdot 2H_2O$) has been identified as the most dominant hydrated evaporite mineral. Therefore, the amount of gypsum present may in principle be estimated from TGA water loss measurements. Here, *gypsum is 5 times the molar quantity of water loss measured by TGA in the defined temperature window. A comparison to XRD derived gypsum content shows a slight overestimation by TGA analysis (Fig. 7.5). Where gypsum/sulfate (XRD) approaches unity – i.e. anhydrite is largely absent – water loss becomes exceptionally high and cannot represent gypsum exclusively. Because of multiple evidence for the presence of other hydrated evaporite salts (see section 7.3.3.4), this is most likely the result of a small but significant contribution of extractable water from the present suite of other minerals with structurally bonded water. Consequently, the TGA-based gypsum content estimate represents a maximum concentration. To highlight this fact, we refer to the mass fraction as *gypsum/(total) sulfate. The occurrence of hydrated salts other than gypsum tends to exclude the presence of large anhydrite content. The spatial distribution of *gypsum/sulfate across the Atacama Desert shows a general trend in the Central Depression with high values in the southern focus area (~24–25°S) and low values in the central (~21°S) and northern focus area (~19°30′S) (Fig. 7.6). This confirms an earlier observation showing that soils along E–W transects at ~24°S (Antofagasta) and ~22°S (Tocopilla) are dominated by gypsum (Rech et al., 2003). With few exceptions, *gypsum/sulfate is high in the Coastal Cordillera.

Samples with *gypsum/sulfate in excess of one – i.e. those containing highly hydrated evaporite minerals other than gypsum – are concentrated in the southern focus area and in higher altitudes towards the Precordillera (Fig. 7.6). In the southern focus area, sulfates are clearly dominated by gypsum both in surface and subsurface samples with a mean *gypsum/sulfate of 0.92 (Fig. 7.6g-i).

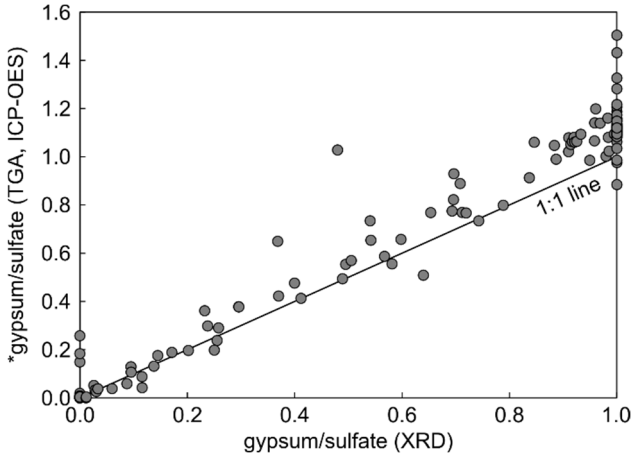

Figure 7.5: Comparison of *gypsum/sulfate determined by TGA and ICP-OES analyses with gypsum/sulfate values derived from semi-quantitative XRD. Total sulfate concentrations may be overestimated in XRD analysis due to disregarding of minor mineral phases. The solid black line represents a 1:1 relationship.

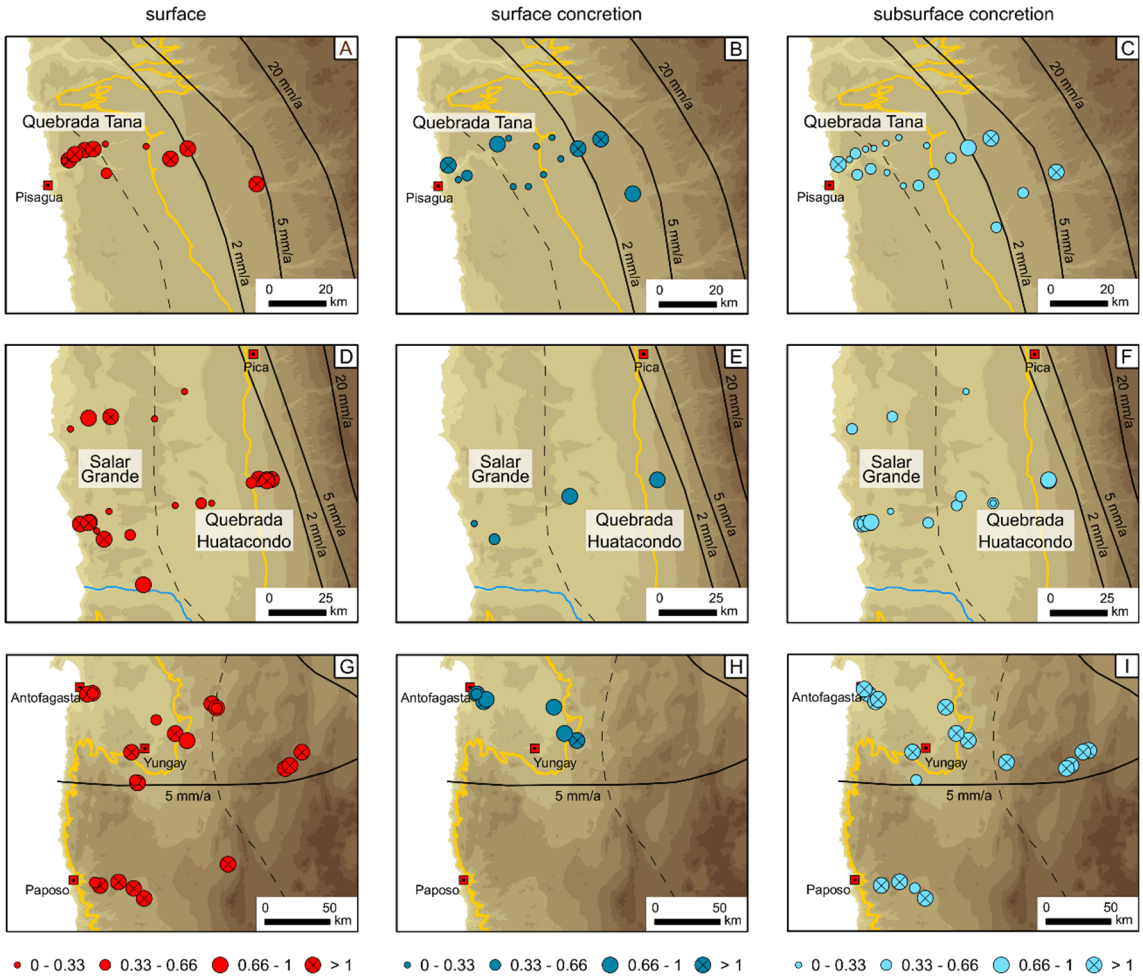

Figure 7.6: *gypsum/sulfate in surface samples (red), surface concretions from deflated/eroded surfaces (dark blue), and subsurface concretions (light blue). Samples with *gypsum/sulfate>1 are most likely the result of the presence of other evaporite minerals than gypsum that contain structurally bonded water. For map features cf. Fig. 7.1.

In the central focus area, surface samples close to the coast and towards the higher altitudes of the Precordillera generally show high *gypsum/sulfate with a mean value of 0.80 (Fig. 7.6d). Surface samples from the Central Depression have higher anhydrite contents, with average *gypsum/sulfate value of only 0.47. Surface samples from the Salar Grande region appear to have higher gypsum proportions than in the Central Depression (Fig. 7.6d). In the northern focus area, samples from the Central Depression have the highest proportions of anhydrite of the entire Atacama (Fig. 7.6a-c). Subsurface concretions in the western part of the Central Depression consist of nearly pure anhydrite. With increasing elevation towards the Precordillera gypsum abundances increase up to nearly pure gypsum at > 1700 m (Fig. 7.6c).

The Coastal Cordillera samples taken north of Quebrada Tana in the northern focus area show additional trends with soil depth that are not well resolved in Fig. 7.6. Surface samples show a high abundance of gypsum (mean *gypsum/sulfate of 0.85), while subsurface concretions are dominated by anhydrite (mean *gypsum/sulfate of 0.24) (Fig. 7.6a,c).

7.4.2.3 Chloride

Chloride concentrations in Atacama Desert soils vary between 1 and 488 $mg \cdot g^{-1}$ (Fig. 7.8). The average Na/Cl ratio is 0.83 (Fig. 7.7), almost identical to the global seawater ratio (Na/Cl = 0.86; Keene et al., 1986 and references therein). Hence, sea spray is the main natural source of Na and Cl for Atacama Desert soils. Even high-chloride concentration samples from the Atacama "desert" soil do not fall on the 1:1 relationship of Na and Cl representative of halite. This implies that erosion and redeposition from the salars – where halite dominates the surface (e.g. Finstad et al., 2016) – contributes little to overall deposition of Na and Cl on the "desert" soil. Subsequent evaporation of sea spray to complete dryness would eventually lead to the precipitation of Mg and K chlorides, e.g. Carnallite ($MgCl_2KCl \cdot 6H_2O$) (Hardie and Eugster, 1980). These salts could balance the apparent Cl-excess with respect to Na, but we do not have any evidence of their presence. Because of the sea salt origin of Na and Cl, exceptionally high Na/Cl ratios in present day aerosol samples (Fig. 7.7; Wang et al., 2014; Li et al., 2019) can be confirmed to represent a large impact of anthropogenic emissions.

A few soil samples show an equally strong enrichment in Na with respect to Cl. These samples also show an enrichment of S relative to Ca, which suggests the presence of sodium sulfate in these samples. Thenardite (Na_2SO_4) is a commonly present mineral phase in the Atacama Desert soil

that often co-occurs with nitrates (Ericksen, 1981, 1983). Strip mining emits large quantities of dust and may thus be a likely cause for these elevated Na/Cl ratios.

The spatial distribution of chloride shows a number of easily detectable trends (Fig. 7.8). In the southern focus area, concentrations are generally very low (~3 $mg \cdot g^{-1}$ on average) in all surface and subsurface samples (Fig. 7.8g–i). In the central focus area, chloride concentrations in surface samples are generally moderate or high (Fig. 7.8d). Chloride concentrations in samples from the surface sample set (surface crust and powdery chuca) fall between 0 and 28 $mg \cdot g^{-1}$. Subsurface concretions are relatively enriched with concentrations between 0.1 and 488 $mg \cdot g^{-1}$. Values below 5 $mg \cdot g^{-1}$ are observed near the coast and at higher altitudes along the western slope of the Precordillera (Fig. 7.8f). Surface concretions consistently show chloride concentrations below 5 $mg \cdot g^{-1}$, but the sample number is small. In the northern focus area, surface samples tend to show low chloride concentrations of < 5 $mg \cdot g^{-1}$ with few exceptions (Fig. 7.8a). In contrast, subsurface concretions are again characterized by high chloride concentrations varying between 160 and 410 $mg \cdot g^{-1}$ in the Coastal Cordillera (Fig. 7.8c). Both in the northern and central focus area, chloride concentrations drop below 5 $mg \cdot g^{-1}$ eastwards at altitudes approaching and above 1200 m, which broadly coincides with the maximum spread of coastal fog advection (Fig. 7.8a-f; Cereceda et al., 2008).

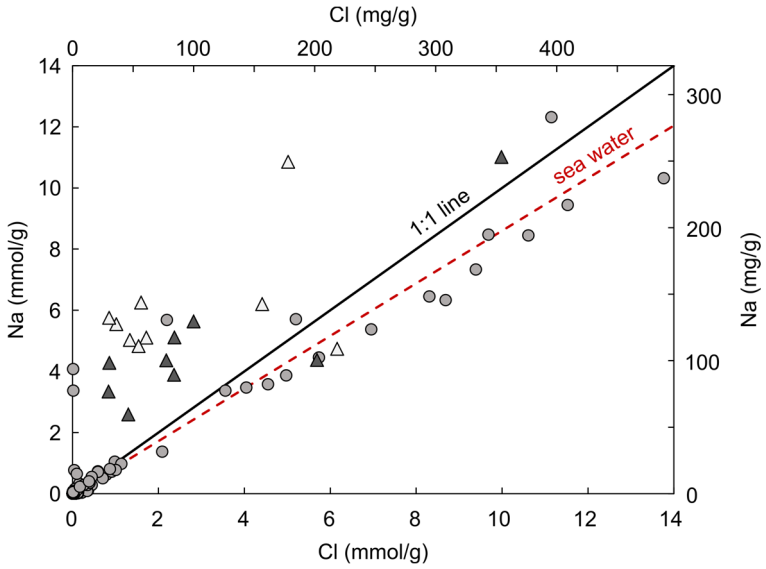

Figure 7.7: Na vs Cl molar concentrations in bulk sediment samples. Circles indicate sediment samples investigated in this study. The modern Na/Cl ratio in seawater (slope: 0.86) is shown as reference (dashed red line; Keene et al., 1986). The solid black line represents a 1:1 relationship. Open and filled triangles symbolize Na/Cl ratios in modern atmospheric dust analyzed by Wang et al. (2014) and Li et al. (2019), respectively, that are probably affected by anthropogenic emissions.

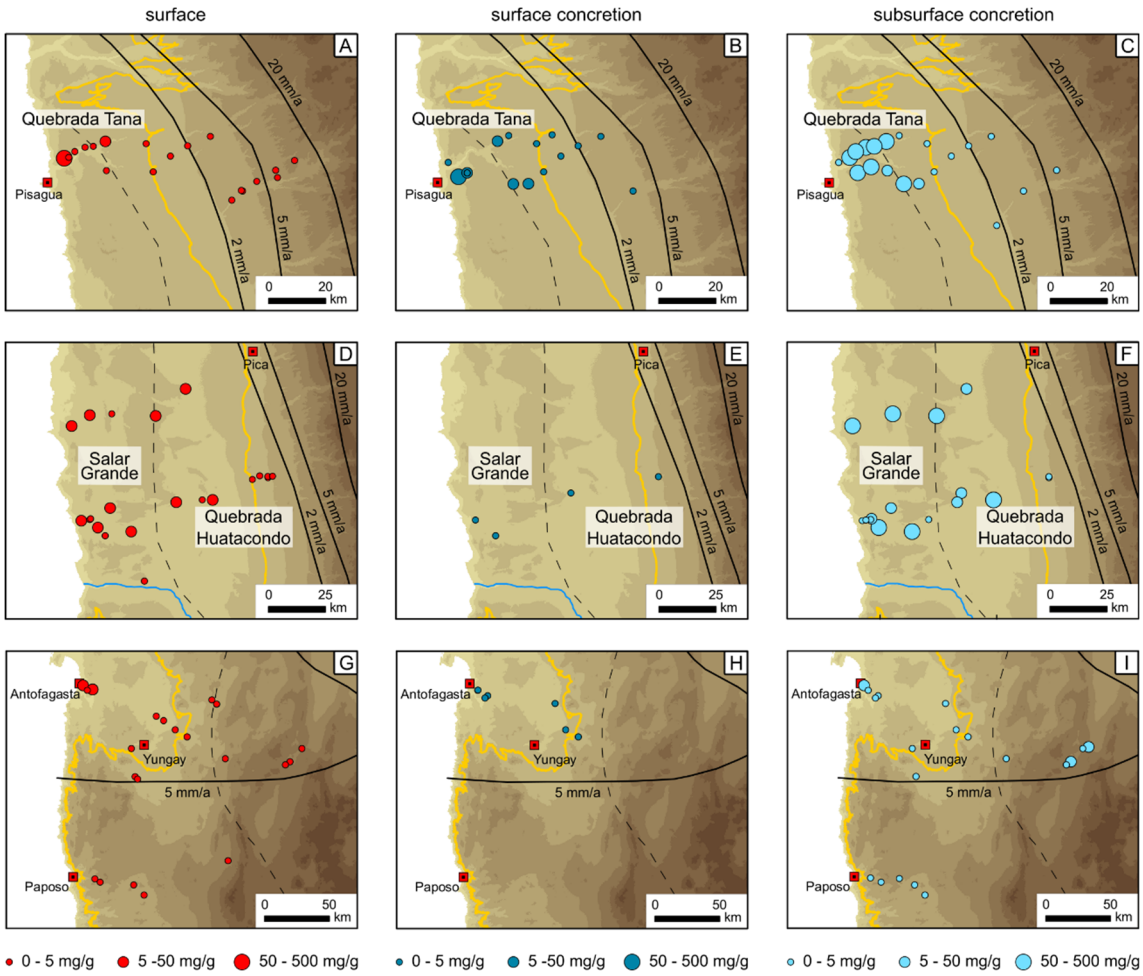

Figure 7.8: Chloride concentrations in surface samples (red), surface concretions from deflated/eroded surfaces (dark blue), and subsurface concretions (light blue) divided in three categories: low (0–5 mg·g^{-1}), moderate (5–50 mg·g^{-1}), and high (50–500 mg·g^{-1}). The white line defines the 1200 m elevation line. For map features cf. Fig. 7.1.

7.4.3 Minor ions

7.4.3.1 Nitrate

Sodium nitrate contents in Atacama soils from our XRD data are generally below 1 wt-%, if present. The spatial distribution shows a general concentration increase from south to north (Fig. 7.9). Highest values are found in subsurface concretions.

In the southern focus area, surface and subsurface samples show nitrate concentrations below 0.3 mg·g^{-1}, with few local exceptions (Fig. 7.9g-i). In the central focus area, nitrate concentrations range between 0.1 and 1.5 mg·g^{-1} (Fig. 7.9d-f). Nitrate concentrations in subsurface concretions mostly range in the moderate category above 0.3 mg·g^{-1}, but with exceptions of up to 30 mg·g^{-1}. There may be a weak trend towards low values close to the coast (Fig. 7.9c). In the northern focus area, surface samples show low to moderate nitrate concentrations. Towards the east,

concentrations drop below 0.3 mg·g^{-1} (Fig. 7.9a). Surface and subsurface concretions show moderate to occasionally elevated nitrate concentrations with respect to the surface crusts and powdery *chuca*. Concretions do not reproduce the eastward concentration drop seen at the surface (Fig. 7.9b-c).

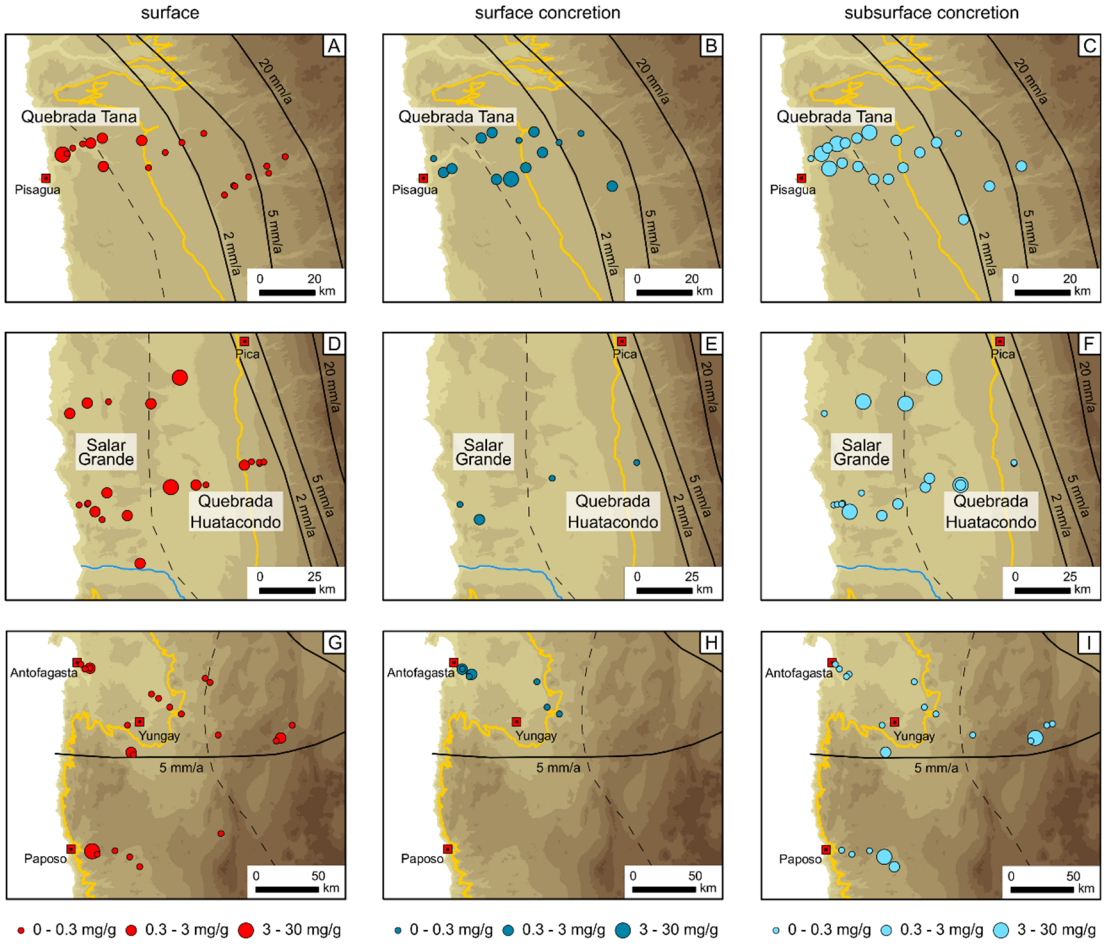

Figure 7.9: Nitrate concentrations in surface samples (red), surface concretions form deflated/eroded surfaces (dark blue) and subsurface concretions (light blue) divided in three categories: low (0–0.3 mg·g^{-1}), moderate (0.3–3 mg·g^{-1}), and high (3–30 mg·g^{-1}). For map features cf. Fig. 7.1.

7.4.3.2 Other minor evaporite mineral phases

X-ray diffraction analyses of our sample set occasionally confirm the presence of various hydrated sulfate minerals of Na, Mg, K, and Ca in Atacama Desert soils (see section 7.4.1). In addition, local presence of Ca-chlorides has been reported (Ericksen, 1981; Pfeiffer et al., 2019). K and Mg are present throughout in the water leachable extracts in small quantities (< 1.3 mg·g^{-1}). These elements are not components of major salts but must be balanced by major anions to form minor salts. Considering this and the indirect evidence for rare hydrated minerals (see section 7.4.2.2), these rare salts may be present more widespread throughout the Atacama Desert in minor quantities than the sporadic detection by our XRD-analyses suggest.

7.5 Discussion

Nitrate concentrations in upper soil parts increase from south to north in agreement with prevailing mean annual precipitation gradients in the Atacama Desert (cf. Fig. 7.1). Such a simple relationship between nitrate concentrations in Atacama Desert soils and water availability most likely reflects the fact that highly soluble nitrates are better preserved under more arid conditions. Rain experiments conducted in the Atacama Desert reveal that precipitation amounts of at least 2 mm are necessary to form free soil water and generate capillary movement into subsurface (Davis et al., 2010). More frequent rain and/or fog events in the southern focus area may lead to the dissolution and removal of nitrates out of the investigated soil depth. Such downward remobilization is evident in many Atacama Desert soil profiles (Ericksen, 1981; Rech et al., 2003). In the central and northern focus areas, the overall subsurface enrichment of nitrate is in agreement with limited downward remobilization at more extreme water limitation.

In the northern focus area, nitrate concentrations at the surface drop eastwards towards the Precordillera, whereas no such concentration gradient occurs in the subsurface concretions. The land surfaces in this part are formed by alluvial fans caused by runoff from the Precordillera. Sedimentologic studies and cosmogenic nuclide dating suggest that some of these fan surfaces were inactive over prolonged episodes of surface stability since the Miocene (Evenstar et al., 2009, 2017; Jordan et al., 2014). Sporadic rain and low volume runoff, however, would still dissolve nitrates at the soil surface, but water amounts may be too low to penetrate deeper into soil, thus leading to shallow subsurface reprecipitation on subsequent evaporation (Fig. 7.9).

Besides of preservation related to water limitation, the nitrate distribution could be related to source effects. Based on the observed seawater relationship between Na and Cl (cf. section 7.4.2.3, Fig. 7.7), and a Cl/NO_3 molar ratio in surface seawater of >200,000, the contribution of marine nitrate deposits is negligible – < 3% with a few local exceptions. Significant amounts of nitrates are formed by photochemical reactions in the atmosphere as indicated by observation of mass-independent fractionation of O-isotopes in nitrate (Böhlke et al., 1997; Michalski et al., 2004; Ewing et al., 2007). Direct atmospheric deposition depends on the OH radical production rate in the atmosphere, which is controlled by total solar insolation showing a largescale latitudinal gradient with an equatorial maximum (Seinfeld and Pandis, 2006). Since the latitudinal band covered in this study is only 6°, this effect on our samples is probably small. However, secular

variations in the OH radical abundance and the unknown but probably different time spans covered in individual samples might cause some scatter in our data.

On the other hand, the giant nitrate ore deposits, are interpreted to form from capillary migration of groundwater and evaporation (Ericksen, 1983), much like the present active salar surface (Finstad et al., 2016). Stable chromium ($\delta^{53}Cr$) and cosmogenic iodine (^{129}I) isotopic studies support a formation of nitrate ore in association with groundwater transport (Pérez-Fodich et al., 2014). Active and fossil salar systems in all focus areas are proof of the at least temporal presence of a shallow groundwater table of meteoric or hydrothermal origin in this area (Magaritz et al., 1990). However, our sample set only consists of soil samples from well outside the salar depositional basins and were mostly taken on geomorphic elevated sites. Nonetheless, availability of groundwater and subsequent capillary suction and evaporation may have changed over time and thus cannot entirely be ruled out over time at our sample sites. For a few single locations, capillary suction could be important and may be responsible for some outliers in the general pattern. However, nitrate ore deposits occur in all our three focus areas, but the general depletion of nitrate in shallow soil depths in the South – except of a few single locations – does not support a major role of groundwater evaporation for nitrate accumulation in the Atacama Desert soil. In general, high nitrate concentrations in our sample set are not related to source effects but rather indicative of long-term hyperarid conditions.

The distribution of chlorides in Atacama Desert soils is generally similar to that of nitrates (cf. Figs. 7.8, 7.9) as may be expected by their respective high solubility and similar solute transport behavior (Walvoord et al., 2003; Ewing et al., 2006; Graham et al., 2008; Al-Taani and Al-Qudah, 2013). However, in contrast to nitrates, chloride concentrations at the surface and subsurface in the central and northern focus areas rapidly decrease above an elevation of 1200 m, which is the average maximum altitude of fog occurrence at the present day (Fig.7.10; Cereceda et al., 2008). Together with the observed seawater relationship of the Na/Cl molar ratio (cf. section 7.4.2.3, Fig. 7.7), this illustrates that the distribution of chloride is the result of a combination of a well-defined single source (sea salt), aerosol transport restricted to the altitude-band of fog advection defined by the inversion layer (650–1200 m). At low elevation along the coast, moisture supply is sufficient to wash out most of the chloride from the upper soil. Besides sea spray, other sources may principally contribute to the total chloride budget in Atacama Desert soils.

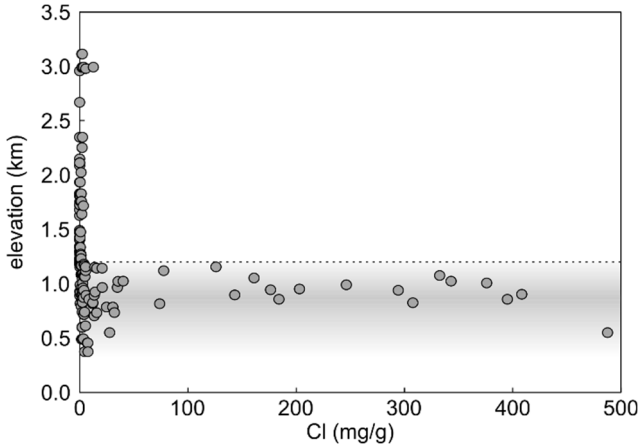

Figure 7.10: Elevation vs Cl concentration in bulk sediment samples. The shaded area indicates the altitudes that are frequently affected by fog, where the dashed black line marks its average maximum altitude (Cereceda et al., 2008). High-chloride concentration samples are only observed within the area of frequent fog occurrence.

Redistributed salts from playas and salar surfaces may cause an enrichment of chlorides in surrounding soils, a process that has been suggested to take place for sulfates (Rech et al., 2003). However, if redeposition from salar halite is a major source of chloride, the Na/Cl ratio in samples with large chloride content should show a molar Na/Cl ratio of 1 (cf. Fig. 7.7), or at the additional presence of thenardite – indicated in a few samples – a Na/Cl ratio in excess of one. Because that is generally not the case, redistribution of halite from salar flats to the surrounding soils can only play a minor role at the present day or is restricted to the very local scale. That may suggest some degree of decoupling from sulfate redeposition (Rech et al., 2003), perhaps reflecting changing conditions in the Atacama Desert over long timescales (see below).

Locally, chlorides may be derived from interactions between hydrothermal brines and sediments (Hardie, 1990; Lowenstein and Risacher, 2009). Hydrothermal brines typically lead to the formation of calcium-, potassium- and magnesium-rich chlorides (e.g. $CaCl_2{\cdot}6H_2O$, $CaMg_2Cl_6{\cdot}12H_2O$, $KCl{\cdot}MgCl_2{\cdot}6H_2O$, $MgCl_2{\cdot}6H_2O$; Warren, 2010). Pfeiffer et al. (2019) described the occurrence of calcium chloride-rich soils in the western part of the Central Depression near *Salar de Llamará* and discussed the potential role of hydrothermal and meteoric sources. However, the occurrence of hydrothermal brines is locally restricted and unlikely to cause chloride enrichment over the entire study area. Minor amounts of chloride could originate from weathering of Andean volcanic rocks (Ericksen, 1981; Berger and Cooke, 1997). However, there is no marked increase with altitude towards the currently volcanic active Western Cordillera (Fig. 7.10). Thus, at least the present data set does not provide any evidence for a significant deposition of volcanic chloride beyond the local scale.

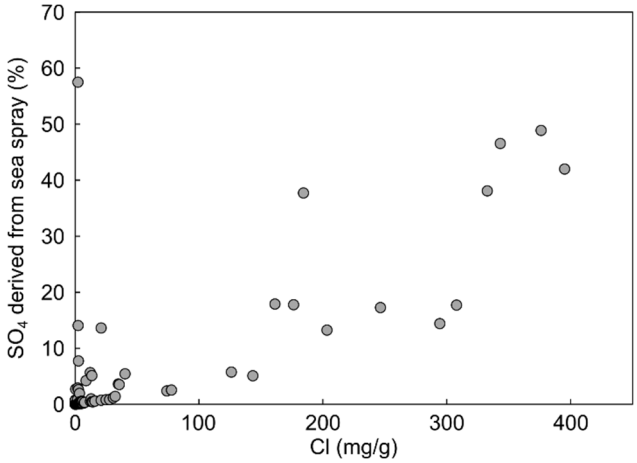

Figure 7.11: Minimum proportion of total sulfate derived from sea spray vs chloride concentration in Atacama Desert soils. Proportions of sulfate derived from sea spray were calculated from chloride concentrations assuming that chloride completely derives from sea spray. Because sulfates are well preserved in Atacama Desert soils and chlorides are dissolved and removed during occasional precipitation events, calculated sulfate proportions represent minimum values. In this approach it is assumed that post-depositional capillary enrichment of chloride is unimportant, which seems reasonable for our sample set (see text).

Sulfates are the most common salts in the soils of the Atacama Desert. In comparison to chlorides and nitrates, calcium sulfates are moderately soluble and generally better preserved. Consequently, they may accumulate near the surface over time relative to halite and nitrates that are washed out quicker. Marine aerosols are one of the sources of sulfate (Ericksen, 1981; Chong, 1988; Rech et al., 2003). Based on the observed seawater relationship of Na and Cl in Atacama Desert soils, and the marine Cl^-/SO_4^{2-} ratio (approximately 19.35 M ratio), the average seawater contribution over the mean residence time of Cl in the Atacama soil surface is 5–50 % for the high chloride samples (50–500 $mg \cdot g^{-1}$) (Fig. 7.11). These estimates represent minimum values, because sulfates accumulate over longer time scales, while chlorides are washed out of investigated soil depths. Stable sulfur isotopes show that the marine source dominates along the coast but disappears inland (Rech et al., 2003). This observation and the suggested relationship to transport of fog is in good agreement with both the chloride distribution discussed above (Fig. 7.8) and the trend of increasing proportion of total sulfate directly derived from sea spray, which may be calculated from chloride concentration (Fig. 7.11). Atmospheric deposition contributes 10–40% to the total sulfate budget in Atacama soils as indicated by triple oxygen isotope analyses of sulfates (Bao et al., 2004; Sun et al., 2018).

Due to a longer residence time, relatively large amounts of calcium sulfates may accumulate in the upper soil profile with respect to other more soluble salts. Redistribution of calcium sulfates from playa deposits has been identified as another contributor to the sulfate inventory (Rech et al., 2003).

In the light of apparently limited chlorine redistribution from the generally halite covered playa/salar surfaces today, redistribution of sulfates may have mostly occurred at a time of higher water availability known from defined intervals in the past (Hartley and Chong, 2002; Evenstar et al., 2009; Jordan et al., 2014), where salars and playa lakes were more active, and where conditions for halite precipitation were not reached. At the present day, redistribution of sulfate may be limited to debris fans. Hydrothermal sulfates and weathering of andesitic and basaltic rocks are alternative sources for sulfate that are potentially important in Atacama Desert soils on local scales.

The spatial distribution of (hydrated) gypsum vs (non-hydrated) anhydrite along a N–S gradient in the Central Depression seems to reflect the overall N–S aridity trend in principle, and – at least in the east – the increasing moisture availability with altitude (cf. Fig. 7.6). Lower anhydrite presence along the coast might be explained by the frequent occurrence of fog that limits anhydrite formation. However, any potential relationship of the gypsum vs anhydrite distribution with water availability is not as straight forward as with the chlorides and nitrates. Anhydrite only forms very late in the evaporation sequence of seawater and crystallization proceeds very slowly (Hardie and Eugster, 1980; Freyer and Voigt, 2003). Therefore, precipitation of anhydrite directly from sea spray seems less likely than a secondary formation process. Our own field observations tentatively suggest such a transformation (see appendix, Fig. A3.5). Secondary anhydrite formation may take place by either dehydration of gypsum to bassanite and γ-anhydrite, phase transformation to β-anhydrite (Christensen et al., 2008; Seufert et al., 2009), or dissolution of gypsum and reprecipitation of β-anhydrite. Experimental dehydration of gypsum to anhydrite generally requires high temperatures (to γ-anhydrite at > 165°C and to β-anhydrite at > 280°C; Christensen et al., 2008). However, long-term isothermal experiments by Seufert et al. (2009) demonstrated that the dehydration process to β- and γ-anhydrite simultaneously proceeds slowly at lower temperatures (> 85°C for 5 days). One may speculate that the time scale of stable surface conditions in the day-night temperature range of approximately 0–40°C in the Atacama Desert over millions of years may be sufficient for gypsum transformation to anhydrite even at slow rates. However, y-anhydrite and/or bassanite is very rare. The most common form of anhydrite by far is β-anhydrite. Therefore, dehydration may not be the most likely process.

Direct precipitation of β-anhydrite from a pure calcium sulfate solution becomes thermodynamically favorable over precipitation of gypsum at temperatures above 42°C (Charola et al., 2007 and references therein). The precipitation of anhydrite proceeds very slowly because

the formation process from sulfate-enriched solutions is kinetically hindered (Freyer and Voigt, 2003). However, the high chloride and nitrate concentrations in the solution may induce primary precipitation of anhydrite at lower temperature (Hardie and Eugster, 1980; Charola et al., 2007). The respective transition temperature decreases to 18°C for saturated NaCl solutions (Hardie, 1967). This temperature shift is the result of a lower thermodynamic activity of water in a concentrated NaCl solution (Raju and Atkinson, 1990; Freyer and Voigt, 2003). Chlorides and nitrates are generally enriched in the surface and near-surface soils in the Central Depression of the central and northern focus area (cf. Figs. 7.8, 7.9). Any type of rare moisture event (fog, rain, runoff flood) that forms a temporary wet environment, either with connate water in the subsurface soil after a fog or rain event, or a shallow remnant pond from a runoff flood, would lead to dissolution of relatively abundant chlorides and nitrates in addition to some gypsum. If conditions allow for a relatively slow precipitation from a solution of high chloride and nitrate concentration, the reprecipitation of calcium sulfate as β-anhydrite is favored over the reprecipitation as gypsum.

7.6 Conclusion

The spatial distribution of gypsum, anhydrite, halite, and nitrates in Atacama Desert soils reflect long-term aridity gradients, sources, and secondary dissolution processes in the top soil. Hyperaridity is most developed in the North between 19 and 22°S. That does not exclude, however, the possibility of hyperaridity in local basins further south, e.g. Yungay (McKay et al., 2003). Nitrates and chlorides are best preserved, where hyperaridity is most intense. The chloride distribution reflects its main source, the Pacific Ocean, and the air flow condition that determine the inland advection of fog. Fog, rain, and runoff redistribute these salts downwards from the soil surface. Calcium sulfates are the dominant salt in the Atacama Desert soil throughout, and the increasing proportion of anhydrite to the north within the Central Depression follows the N–S aridity gradient. However, the formation of anhydrite is probably the result of secondary dissolution of gypsum and reprecipitation that perhaps is enabled by high concentration of other soluble salts under current environmental conditions. Anhydrite formation in the North may thus reflect the preservation and remobilization capacity of halite and nitrates in Atacama Desert soils. The apparently exclusive presence of large anhydrite contents in the Central Depression, however, suggest an additional, yet unknown geomorphologic/topographic parameter important for anhydrite formation.

8 Conclusion

This thesis evaluated the potential of combined analyses of hydrogen and triple oxygen isotopes of structurally bonded water of lacustrine gypsum to quantitatively reconstruct past changes in humidity.

The first study examined fundamental hydrological processes governing the isotopic composition of lakes in the complex and highly dynamic system of the Salar del Huasco, an endorheic salt flat located in the semiarid high-altitude Altiplano, N-Chile. Principle processes in hydrological systems – evaporation, recharge and mixing – can be identified by triple oxygen isotope analysis. The isotopic composition of ponds and lakes from the Salar del Huasco principally follows the recharge evaporation trendline predicted by the classic Craig-Gordon evaporation model. Considerable dynamics in the isotopic composition of ponds and lakes occur due to inflow from multiple sources and episodic flooding after thunderstorms that can lead to the formation of non-recharged ephemeral lakes and may induce mixing processes. In-situ pan evaporation experiments demonstrated that freezing and thawing processes may have significant effects on the isotopic composition of lake water. All these effects are either of transient nature or may be averaged out over timescales of gypsum precipitation. Thus, the Craig-Gordon model can principally serve as a useful tool to reconstruct past changes in humidity even in complex and highly dynamic hydrological systems.

The second study investigated the isotopic composition of structurally bonded water of lacustrine gypsum deposits from two different sites in the Atacama Desert to evaluate its potential to quantify paleo-humidity conditions. Derived isotopic compositions of paleo-lake water follow distinct evaporation trends of increasing $\delta^{18}O$ with decreasing ^{17}O-excess and d-excess. For a defined set of input parameters (δ_{WI}, δ_V, n, E/I, T), fitting the Craig-Gordon function to the isotopic composition of paleo-lake water provides reasonable humidity values demonstrating the principal applicability of the combined analysis of hydrogen and triple oxygen isotopes of structurally bonded water of gypsum to quantitatively estimate past changes in relative humidity. The model output humidity is less affected by changes in the isotopic composition of source water δ_{WI} and atmospheric vapor δ_V, but can strongly depend on the selected turbulence coefficient n and the restrictions of the evaporation-to-inflow ratio E/I. The uncertainty in the derived paleo-humidity is limited by the

discrimination of evaporation trajectories for different humidity that mainly depends on the isotopic difference between source water δ_{WI} and atmospheric vapor δ_V.

The method was applied to gypsum deposits of Late Miocene to Mid-Pleistocene age from the Mejillones Peninsula located in close proximity to the coast in the southern part of the Atacama Desert. Values of $\delta^{18}O$ of paleo-lake water in excess of 0 ‰ confirm the proposed marine origin of these gypsum deposits. Constraining other input parameters in a reasonable range, the model gives relative humidities between 60 and 70 %, which are comparable to present climate conditions at the Mejillones site.

Furthermore, Pliocene gypsum deposits from the Tiliviche formation located in the westernmost part of the Central Depression in the northern Atacama Desert were investigated. The isotopic composition of derived paleo-lake water indicates that the Pliocene climate in the northern Atacama Desert might have been more humid compared to today. Wetter than present climate may have been triggered by permanent El Niño-like conditions in the Early Pliocene that may have led to the frequent occurrence of precipitation events not only in the adjacent Altiplano but also in presently hyperarid regions of the Atacama Desert. However, the model results indicate that the paleo-lake may have been affected by mixing processes, e.g. due to the frequent occurrence of precipitation and flooding events. Thus, estimated humidity values of 65-80 % represent maximum values and must be verified by further investigations.

An essential part of this thesis was to improve the understanding of soil formation and secondary redistribution and transformation processes of evaporites, which is crucial to correctly interpret the isotopic composition of structurally bonded water of pedogenic gypsum. Systematic investigation of the spatial distribution of highly soluble salts – chlorides and nitrates – as well as gypsum and anhydrite in Atacama Desert soils revealed their relation to long-term aridity gradients, sources and secondary dissolution processes. Nitrate is deposited uniformly and best preserved in central and northern parts of the Atacama Desert suggesting that hyperaridity is most persistent between 19-22°S. The distribution of chloride principally follows the same aridity gradient but is modified by its primary source – sea spray. Exceptionally high chloride contents were observed at altitudes < 1200 m indicating that the atmospheric temperature inversion layer forms an effective barrier to upward mixing of air masses derived from the Pacific Ocean. Calcium sulfate is the dominant desert soil mineral in the Atacama Desert. Abundances of gypsum and anhydrite principally follow the N-S aridity gradient within the Central Depression. The co-occurrence of high abundances of anhydrite

with high chloride and nitrate concentrations points to a secondary formation of anhydrite by dissolution and reprecipitation in highly saline fluids. However, the N-S aridity gradient is not reflected in the Coastal Cordillera and the western slopes of the Andes suggesting an additional geomorphologic or topographic factor favoring anhydrite formation.

9 Outlook

The results of this thesis demonstrated that analysis of hydrogen ($^{2}H/^{1}H$) and triple oxygen ($^{18}O/^{17}O/^{16}O$) isotopes of water structurally bonded in gypsum can be a suitable tool to quantitatively estimate (paleo-) humidity conditions. However, further investigations are necessary to improve the understanding of the dynamics in the isotopic composition of lakes and their impact on the isotopic composition of structurally bonded water of gypsum.

To reconstruct paleo-humidity using the Craig-Gordon model the range of model inputs for variables like the isotopic composition of atmospheric vapor and the turbulence coefficient must be estimated. A better understanding of the relationship between the turbulence coefficient and wind speed and processes controlling the isotopic composition of atmospheric vapor would contribute to more accurate model results. In chapter 5 we demonstrated that the turbulence coefficient can be precisely determined from pan evaporation experiment data without accurate knowledge of the isotopic composition of atmospheric vapor. Detailed monitoring of pan evaporation experiments in different environmental settings can be used to investigate the variability of the turbulence coefficient in natural environments and may eventually allow to calibrate the turbulence coefficient to wind speed.

The isotopic composition of atmospheric vapor may be estimated from precipitation. However, as shown in chapter 5, this approach may not be suitable in arid environments, where precipitation is generally rare, and in settings with seasonal variability in atmospheric moisture sources. Monitoring of atmospheric vapor in such environments would provide information on the variability of the isotopic composition of atmospheric vapor on daily, monthly and seasonal timescales. Furthermore, the understanding of processes that control d-excess and ^{17}O-excess of atmospheric vapor could be improved. However, traditional methods often require liquid nitrogen, dry ice/ethanol slurry or other cooling baths to cryogenically trap atmospheric vapor and are thus not suitable for field work. Recent advances in laser spectroscopy enabled high-resolution monitoring of $\delta^{2}H$, $\delta^{17}O$, and $\delta^{18}O$ in vapor but their suitability for large-scale field campaigns is limited (Steig et al., 2014; Gázquez et al., 2015; Schauer et al., 2016; Pierchala et al., 2019). We built a Stirling-cooler based vapor sampler after Peters and Yakir (2010), which provides a simple and highly portable system that is easy to operate in the field. First applications of this vapor sampling system

in the Atacama Desert were successful, but the method still needs to be improved to accurately determine d-excess and ^{17}O-excess in atmospheric vapor. Preliminary measurements of atmospheric vapor in the Atacama Desert revealed a systematic decrease of $\delta^{18}O_V$ with increasing distance from the coast (Fig. A1.6). The process leading to this systematic trend is yet not fully understood but may be related to radiative cooling and condensation at night and re-evaporation during the day. Further vapor measurements are required to verify this trend and to identify processes that control the isotopic composition of atmospheric vapor in the Atacama Desert.

Isotope analyses of natural waters from the Salar del Huasco (chapter 5) revealed substantial dynamics in the isotopic composition of springs, rivers and lakes, which were attributed to the seasonality of precipitation, seasonal and diurnal variability of temperature and relative humidity as well as mixing processes induced by the sporadic occurrence of flooding events. Our results demonstrated that changes in the environmental parameters and mixing processes can be identified by triple oxygen isotope analyses. However, it remains unsolved, which mean temperature and humidity values best reflect the average isotopic composition of lakes and how much time it takes to re-establish steady state conditions after a mixing event. This probably depends on the surface-to-volume ratio of the lake as well as the evaporation and the recharge rate. Detailed monitoring of the isotopic composition of lakes, evaporation rates, hydrological parameters and climatic conditions can contribute to a better understanding of the interplay of these variables.

Furthermore, freezing and thawing can significantly impact the isotopic composition of evaporating water as demonstrated by pan evaporation experiments carried out at the Salar del Huasco (Chapter 5). Freezing and thawing may also affect the isotopic composition of shallow ponds and lakes in the Salar del Huasco and other evaporative environments where temperatures drop below 0°C and lakes froze over. Possible effects of freezing and thawing on the isotopic composition of evaporating water bodies should be investigated in future studies.

Modelling the isotopic composition of structurally bonded water of gypsum from samples of the Tiliviche formation implies the prevalence of humid conditions in the northern Atacama Desert about 3.5 Ma ago (Chapter 6). However, model results indicate that the paleo-lake may have been affected by mixing processes, e.g. due to frequent occurrence of precipitation in the catchment area. Investigation of isotope systematics during evaporation in humid regions may help to disentangle potential effects of frequent precipitation and flooding on the isotopic composition of lake water

and improve the understanding of processes controlling the isotopic composition of lakes in past humid phases.

This thesis demonstrated the potential of isotope analyses of lacustrine gypsum to quantitatively reconstruct paleo-humidity conditions (Chapter 6). Future work aims to expand the methodology to pedogenic gypsum. For this purpose, processes of gypsum formation and transformation in Atacama Desert soils must be better understood. Additionally, hydrogen and triple isotope systematics during evaporation from soils as well as isotope fractionation effects and possible isotope exchange reactions between soil water and structurally bonded water of gypsum need to be investigated. First insights in soil processes provides the third study of this thesis (Chapter 7). Results of this study point to primary formation of gypsum by evaporation and secondary transformation to anhydrite by dissolution and reprecipitation in highly saline fluids. However, the environmental conditions required for that transformation must be the result of a complex interplay of molecular level processes, water and salt availability aspects, as well as geomorphologic and topographic factors. The combined analyses of trace elements (Sr, Mg, P, Na, Ba, REE) and isotopes ($^{16}O/^{17}O/^{18}O$, $^{34}S/^{32}S$, $^{87}Sr/^{86}Sr$) may help to unravel the gradual interplay of all these factors. Once soil evaporation, isotope fractionation during gypsum formation in soils as well as secondary transformation and isotope exchange reactions are better understood, the method to reconstruct paleo-humidity by isotope analyses of structurally bonded water of gypsum can be applied to the widespread pedogenic gypsum deposits in the Atacama Desert. The combination of isotope analyses of lacustrine and pedogenic gypsum may allow to achieve a quantitative reconstruction of past humidity conditions in the Atacama Desert.

References

Acosta, O., Custodio, E., 2008. Impactos ambientales de las extracciones de agua subterránea en el Salar del Huasco (norte de Chile). Bol. Geol. y Min. 119, 33–50.

Al-Taani, A.A., Al-Qudah, K.A., 2013. Investigation of desert subsoil nitrate in Northeastern Badia of Jordan. Sci. Total Environ. 442, 111–115.

Alexandre, A., Landais, A., Vallet-Coulomb, C., Piel, C., Devidal, S., Pauchet, S., Sonzogni, C., Couapel, M., Pasturel, M., Cornuault, P., Xin, J., Mazur, J.-C., Prié, F., Bentaleb, I., Webb, E., Chalié, F., Roy, J., 2018. The triple oxygen isotope composition of phytoliths as a proxy of continental atmospheric humidity: insights from climate chamber and climate transect calibrations. Biogeosciences 15, 3223–3241.

Alexandre, A., Webb, E., Landais, A., Piel, C., Devidal, S., Sonzogni, C., Couapel, M., Mazur, J., Pierre, M., Prié, F., Vallet-coulomb, C., Outrequin, C., Roy, J., 2019. Effects of leaf length and development stage on the triple oxygen isotope signature of grass leaf water and phytoliths: insights for a proxy of continental atmospheric humidity. Biogeosciences 16, 4613–4625.

Allmendinger, R.W., González, G., 2010. Invited review paper: Neogene to Quaternary tectonics of the coastal Cordillera, northern Chile. Tectonophysics 495, 93–110.

Alpers, C.N., Brimhall, G.H., 1988. Middle Miocene climatic change in the Atacama Desert, northern Chile: Evidence from supergene mineralization at La Escondida. Bull. Geol. Soc. Am. 100, 1640–1656.

Angert, A., Cappa, C.D., DePaolo, D.J., 2004. Kinetic ^{17}O effects in the hydrologic cycle: Indirect evidence and implications. Geochim. Cosmochim. Acta 68, 3487–3495.

Aravena, R., 1995. Isotope hydrology and geochemistry of northern Chile groundwaters. Bull. l'Institut Fr. d'études Andin. 24, 495–503.

Aravena, R., Suzuki, O., Peña, H., Pollastri, A., Fuenzalida, H., Grilli, A., 1999. Isotopic composition and origin of the precipitation in Northern Chile. Appl. Geochemistry 14, 411–422.

Armijo, R., Thiele, R., 1990. Active faulting in northern Chile: ramp stacking and lateral decoupling along a subduction plate boundary? Earth Planet. Sci. Lett. 98, 40–61.

Baertschi, P., 1953. Über die relativen Unterschiede im H218O-Gehalt natürlicher Wässer. Helv. Chim. Acta 36, 1352–1369.

Baker, L., Franchi, I.A., Maynard, J., Wright, I.P., Pillinger, C.T., 2002. A Technique for the Determination of $^{18}O/^{16}O$ and $^{17}O/^{16}O$ Isotopic Ratios in Water from Small Liquid and Solid Samples. Anal. Chem. 74, 1665–1673.

Bao, H., Jenkins, K.A., Khachaturyan, M., Díaz, G.C., 2004. Different sulfate sources and their post-depositional migration in Atacama soils. Earth Planet. Sci. Lett. 224, 577–587.

Barkan, E., Luz, B., 2007. Diffusivity fractionations of $H_2{}^{16}O/H_2{}^{17}O$ and $H_2{}^{16}O/H_2{}^{18}O$ in air and their implications for isotope hydrology. Rapid Commun. Mass Spectrom. 21, 2999–3005.

Barkan, E., Luz, B., 2005. High precision measurements of $^{17}O/^{16}O$ and $^{18}O/^{16}O$ ratios in H_2O. Rapid Commun. Mass Spectrom. 19, 3737–3742.

Barker, P.F., Burrell, J., 1977. The opening of Drake Passage. Mar. Geol. 25, 15–34.

Berger, I.A., Cooke, R.U., 1997. The Origin and Distribution of Salts on Alluvial Fans in The Atacama Desert, Northern Chile. Earth Surf. Process. Landforms 22, 581–600.

Berner, E.K., Berner, R.A., 2012. Global Environment: Water, Air, and Geochemical Cycles, 2nd ed. Princeton University Press, New Jersey.

Betancourt, J.L., Latorre, C., Rech, J.A., Quade, J., Rylander, K.A., 2000. A 22,000-Year Record of Monsoonal Precipitation from Northern Chile's Atacama Desert. Science . 289, 1542–1546.

Binnie, S.A., Reicherter, K.R., Victor, P., González, G., Binnie, A., Niemann, K., Stuart, F.M., Lenting, C., Heinze, S., Freeman, S.P.H.T., Dunai, T.J., 2020. The origins and implications of paleochannels in hyperarid, tectonically active regions: The northern Atacama Desert, Chile. Glob. Planet. Change 185, 103083.

Bobst, A.L., Lowenstein, T.K., Jordan, T.E., Godfrey, L. V., Ku, T.-L., Luo, S., 2001. A 106 ka paleoclimate record from the Salar de Atacama, northern Chile. Paleogeography, Palaeoclimatol. Palaeoecol. 173, 21–42.

Böhlke, J.K., Ericksen, G.E., Revesz, K., 1997. Stable isotope evidence for an atmospheric origin of desert nitrate deposits in northern Chile and southern California, U.S.A. Chem. Geol. 136, 135–152.

Bouis, P.A., 2006. Reagent chemicals: Specifications and procedures. Oxford University Press.

Bowen, G.J., Wassenaar, L.I., Hobson, K.A., 2005. Global application of stable hydrogen and oxygen isotopes to wildlife forensics. Oecologia 143, 337–348.

Breit, G.N., Simmons, E.C., Goldhaber, M.B., 1985. Dissolution of barite for the analysis of strontium isotopes and other chemical and isotopic variations using aqueous sodium carbonate. Chem. Geol. Isot. Geosci. Sect. 52, 333–336.

CEAZA, (Centro de Estudios Avanzados en Zonas Áridas), 2019. Estación Salar de Huasco. [http://www.ceazamet.cl] (accessed 6.11.18).

Cereceda, P., Larrain, H., Osses, P., Farías, M., Egaña, I., 2008. The spatial and temporal variability of fog and its relation to fog oases in the Atacama Desert, Chile. Atmos. Res. 87, 312–323.

Cereceda, P., Osses, P., Larrain, H., Farías, M., Lagos, M., Pinto, R., Schemenauer, R.S., 2002. Advective, orographic and radiation fog in the Tarapacá region, Chile. Atmos. Res. 64, 261–271.

Charola, A.E., Pühringer, J., Steiger, M., 2007. Gypsum: A review of its role in the deterioration of building materials. Environ. Geol. 52, 207–220.

Chong, G., 1994. The Nitrate Deposits of Chile, in: Reutter KJ., Scheuber E., W.P.J. (Ed.), Tectonics of the Southern Central Andes. Springer, Berlin, Heidelberg, pp. 303–316.

Chong, G., 1988. The cenozoic saline deposits of the chilean andes between 18°00′ and 27°00′ south latitude, in: Bahlburg, H., Breitkreuz, C., Giese, P. (Eds.), The Southern Central Andes. Springer, Berlin, Heidelberg, pp. 137–151.

Christensen, A.N., Olesen, M., Cerenius, Y., Jensen, T.R., 2008. Formation and Transformation of Five Different Phases in the $CaSO_4$-H_2O System: Crystal Structure of the Subhydrate beta-$CaSO_4{\cdot}0.5H_2O$ and Soluble Anhydrite $CaSO_4$. Chem. Mater. 20, 2124–2132.

Cosentino, N.J., Jordan, T.E., 2017. $^{87}Sr/^{86}Sr$ of calcium sulfate in ancient soils of hyperarid settings as a paleoaltitude proxy: Pliocene to Quaternary constraints for northern Chile (19.5–21.7°S). Tectonics 36, 137–162.

Coudurier-Curveur, A., Lacassin, R., Armijo, R., 2015. Andean growth and monsoon winds drive landscape evolution at SW margin of South America. Earth Planet. Sci. Lett. 414, 87–99.

Craig, H., 1961. Isotopic Variations in Meteoric Waters. Science. 133, 1702–1703.

Craig, H., Gordon, L.I., 1965. Deuterium and oxygen 18 variations in the ocean and the marine atmosphere, in: Stable Isotopes in Oceanographic Studies and Paleotemperatures. 9–130.

Criss, R.E., 1999. Principles of Stable Isotope Distribution. Oxford University Press.

Dansgaard, W., 1964. Stable isotopes in precipitation. Tellus 16, 436–468.

Darwin, C., 1839. The voyage of HMS Beagle. Colburn, H., London.

Davis, W.L., de Pater, I., McKay, C.P., 2010. Rain infiltration and crust formation in the extreme arid zone of the Atacama Desert, Chile. Planet. Space Sci. 58, 616–622.

de Wet, C.B., Godfrey, L., de Wet, A.P., 2015. Sedimentology and stable isotopes from a lacustrine-to-palustrine limestone deposited in an arid setting, climatic and tectonic factors: Miocene-Pliocene Opache Formation, Atacama Desert, Chile. Palaeogeogr. Palaeoclimatol. Palaeoecol. 426, 46–67.

Dekens, P.S., Ravelo, A.C., McCarthy, M.D., 2007. Warm upwelling regions in the Pliocene warm period. Paleoceanography 22, 1–12.

Di Celma, C., Pierantoni, P.P., Cantalamessa, G., 2014. Geological map of the Miocene-Pleistocene successions of the Mejillones Peninsula, Northern Chile. J. Maps 10, 350–363.

Dirección Meteorológica de Chile, 2020. Meteorological and climatic data of weather stations in the Atacama Desert, Chile. [https://climatologia.meteochile.gob.cl/] (accessed 18.1.20).

Dongmann, G., Nürnberg, H.W., Förstel, H., Wagener, K., 1974. On the enrichment of $H_2{}^{18}O$ in the leaves of transpiring plants. Radiat. Environ. Biophys. 11, 41–52.

Dunai, T.J., González López, G.A., Juez-Larré, J., 2005. Oligocene-Miocene age of aridity in the Atacama Desert revealed by exposure dating of erosion-sensitive landforms. Geology 33, 321–324.

Epstein, S., Mayeda, T., 1953. Variation of O^{18} content of waters from natural sources. Geochim. Cosmochim. Acta 4, 213–224.

Ericksen, G.E., 1983. The Chilean Nitrate Deposits. Am. Sci. 71, 366–374.

Ericksen, G.E., 1981. Geology and Origin of the Chilean Nitrate Deposits. Geol. Surv. Prof. Pap. 42.

Evans, N.P., Bauska, T.K., Gázquez, F., Brenner, M., Curtis, J.H., Hodell, D.A., 2018. Quantification of drought during the collapse of the classic Maya civilization. Science. 501, 498–501.

Evans, N.P., Turchyn, A. V., Gázquez, F., Bontognali, T.R.R., Chapman, H.J., Hodell, D.A., 2015. Coupled measurements of $\delta^{18}O$ and δD of hydration water and salinity of fluid inclusions in gypsum from the Messinian Yesares Member, Sorbas Basin (SE Spain). Earth Planet. Sci. Lett. 430, 499–510.

Evenstar, L.A., Hartley, A.J., Stuart, F.M., Mather, A.E., Rice, C.M., Chong, G., 2009. Multiphase development of the Atacama Planation Surface recorded by cosmogenic ^{3}He exposure ages: Implications for uplift and Cenozoic climate change in Western South America. Geology 37, 27–30.

Evenstar, L.A., Mather, A.E., Hartley, A.J., Stuart, F.M., Sparks, R.S.J., Cooper, F.J., 2017. Geomorphology on geologic timescales: Evolution of the late Cenozoic Pacific paleosurface in Northern Chile and Southern Peru. Earth-Science Rev. 171, 1–27.

Evenstar, L.A., Stuart, F.M., Hartley, A.J., Tattitch, B., 2015. Slow Cenozoic uplift of the western Andean Cordillera indicated by cosmogenic ^{3}He in alluvial boulders from the Pacific Planation Surface. Geophys. Res. Lett. 42, 1–8.

Ewing, S.A., Michalski, G., Thiemens, M., Quinn, R.C., Macalady, J.L., Kohl, S., Wankel, S.D., Kendall, C., Mckay, C.P., Amundson, R., 2007. Rainfall limit of the N cycle on Earth. Global Biogeochem. Cycles 21, 1–12.

Ewing, S.A., Sutter, B., Owen, J., Nishiizumi, K., Sharp, W., Cliff, S.S., Perry, K., Dietrich, W., McKay, C.P., Amundson, R., 2006. A threshold in soil formation at Earth's arid-hyperarid transition. Geochim. Cosmochim. Acta 70, 5293–5322.

Farías, M., Charrier, R., Comte, D., Martinod, J., Hérail, G., 2005. Late Cenozoic deformation and uplift of the western flank of the Altiplano: Evidence from the depositional, tectonic, and geomorphologic evolution and shallow seismic activity (northern Chile at 19°30′S). Tectonics 24, 1–27.

Farpoor, M.H., Khademi, H., Eghbal, M.K., Krouse, H.R., 2004. Mode of gypsum deposition in southeastern Iranian soils as revealed by isotopic composition of crystallization water. Geoderma 121, 233–242.

Feitl, M., Kern, A.K., Jones, A., Fritz, S.C., Baker, P.A., Joeckel, R.M., Salenbien, W., Willard, D., 2019. Paleoclimate of the subtropical Andes during the latest Miocene, Lauca Basin, Chile. Palaeogeogr. Palaeoclimatol. Palaeoecol. 534, 109336.

Finstad, K., Pfeiffer, M., McNicol, G., Barnes, J., Demergasso, C., Chong, G., Amundson, R., 2016. Rates and geochemical processes of soil and salt crust formation in Salars of the Atacama Desert, Chile. Geoderma 284, 57–72.

Flores Grandez, V., 2010. Modelo conceptual hidrogeológico de la cuenca del Salar del Huasco. Thesis. Pontificia Universidad Catolica de Chile.

Freyer, D., Voigt, W., 2003. Crystallization and Phase Stability of $CaSO_4$ and $CaSO_4$- Based Salts. Monatshefte fur Chemie 134, 693–719.

Friedman, I., 1953. Deuterium content of natural waters and other substances. Geochim. Cosmochim. Acta 4, 89–103.

Fritz, P., Suzuki, O., Silva, C., Salati, E., 1981. Isotope hydrology of groundwaters in the Pampa del Tamarugal, Chile. J. Hydrol. 53, 161–184.

Garcia, M., Hérail, G., 2005. Fault-related folding, drainage network evolution and valley incision during the Neogene in the Andean Precordillera of Northern Chile. Geomorphology 65, 279–300.

Garcia, M., Riquelme, R., Farias, M., Herail, G., Charrier, R., 2011. Late Miocene-Holocene canyon incision in the western Altiplano, northern Chile: tectonic or climatic forcing? J. Geol. Soc. London. 168, 1047–1060.

Garreaud, R., Vuille, M., Clement, A.C., 2003. The climate of the Altiplano: Observed current conditions and mechanisms of past changes. Palaeogeogr. Palaeoclimatol. Palaeoecol. 194, 5–22.

Garreaud, R.D., Aceituno, P., 2001. Interannual Rainfall Variability over the South American Altiplano. J. Clim. 14, 2779–2789.

Garreaud, R.D., Molina, A., Farias, M., 2010. Andean uplift, ocean cooling and Atacama hyperaridity: A climate modeling perspective. Earth Planet. Sci. Lett. 292, 39–50.

Garzione, C.N., McQuarrie, N., Perez, N.D., Ehlers, T.A., Beck, S.L., Kar, N., Eichelberger, N., Chapman, A.D., Ward, K.M., Ducea, M.N., Lease, R.O., Poulsen, C.J., Wagner, L.S., Saylor, J.E., Zandt, G., Horton, B.K., 2017. Tectonic Evolution of the Central Andean Plateau and Implications for the Growth of Plateaus. Annu. Rev. Earth Planet. Sci. 45, 529–559.

Gat, J.R., 1996. Oxygen and Hydrogen Isotopes in the Hydrologic Cycle. Annu. Rev. Earth Planet. Sci. 24, 225–262.

Gaupp, R., Kött, A., Wörner, G., 1999. Palaeoclimatic implications of Mio-Pliocene sedimentation in the high-altitude intra-arc Lauca Basin of northern Chile. Palaeogeogr. Palaeoclimatol. Palaeoecol. 151, 79–100.

Gayo, E.M., Latorre, C., Jordan, T.E., Nester, P.L., Estay, S.A., Ojeda, K.F., Santoro, C.M., 2012. Late Quaternary hydrological and ecological changes in the hyperarid core of the northern Atacama Desert (~21°S). Earth-Science Rev. 113, 120–140.

Gázquez, F., Evans, N.P., Hodell, D.A., 2017. Precise and accurate isotope fractionation factors ($\alpha^{17}O$, $\alpha^{18}O$ and αD) for water and $CaSO_4{\cdot}2H_2O$ (gypsum). Geochim. Cosmochim. Acta 198, 259–270.

Gázquez, F., Mather, I., Rolfe, J., Evans, N.P., Herwartz, D., Staubwasser, M., Hodell, D.A., 2015. Simultaneous analysis of $^{17}O/^{16}O$, $^{18}O/^{16}O$ and $^{2}H/^{1}H$ of gypsum hydration water by cavity ring-down laser spectroscopy. Rapid Commun. Mass Spectrom. 29, 1997–2006.

Gázquez, F., Morellón, M., Bauska, T., Herwartz, D., Surma, J., Moreno, A., Staubwasser, M., Valero-Garcés, B., Delgado-Huertas, A., Hodell, D.A., 2018. Triple oxygen and hydrogen isotopes of gypsum hydration water for quantitative paleo-humidity reconstruction. Earth Planet. Sci. Lett. 481, 177–188.

Gibson, J.J., 2002. Short-term evaporation and water budget comparisons in shallow Arctic lakes using non-steady isotope mass balance. J. Hydrol. 264, 242–261.

Gibson, J.J., Birks, S.J., Yi, Y., 2016. Stable isotope mass balance of lakes: A contemporary perspective. Quat. Sci. Rev. 131, 316–328.

Gibson, J.J., Reid, R., 2010. Stable isotope fingerprint of open-water evaporation losses and effective drainage area fluctuations in a subarctic shield watershed. J. Hydrol. 381, 142–150.

Gibson, J.J., Reid, R., 2014. Water balance along a chain of tundra lakes: A 20-year isotopic perspective. J. Hydrol. 519, 2148–2164.

Gonfiantini, R., 1986. Environmental isotopes in lake studies, in: Fontes, D., Fritz, P. (Eds.), Handbook of Environmental Isotope Geochemistry. Elsevier Science, 119–168.

Gonfiantini, R., Fontes, J.C., 1963. Oxygen isotopic fractionation in the water of crystallization of gypsum. Nature 200, 644–646.

Gonfiantini, R., Wassenaar, L.I., Araguas-araguas, L., Aggarwal, P.K., 2018. A unified Craig-Gordon isotope model of stable hydrogen and oxygen isotope fractionation during fresh or saltwater evaporation. Geochim. Cosmochim. Acta 235, 224–236.

González, G., Cembrano, J., Carrizo, D., Macci, A., Schneider, H., 2003. The link between forearc tectonics and Pliocene-Quaternary deformation of the Coastal Cordillera, northern Chile. J. South Am. Earth Sci. 16, 321–342.

Graham, R.C., Hirmas, D.R., Wood, Y.A., Amrhein, C., 2008. Large near-surface nitrate pools in soils capped by desert pavement in the Mojave Desert, California. Geology 36, 259–262.

Grauel, A.L., Hodell, D.A., Bernasconi, S.M., 2016. Quantitative estimates of tropical temperature change in lowland Central America during the last 42 ka. Earth Planet. Sci. Lett. 438, 37–46.

Gregory-Wodzicki, K.M., 2000. Uplift history of the Central and Northern Andes: A review. Bull. Geol. Soc. Am. 112, 1091–1105.

Haese, B., Werner, M., Lohmann, G., 2013. Stable water isotopes in the coupled atmosphere – land surface model ECHAM5-JSBACH. Geosci. Model Dev. 6, 1463–1480.

Hałas, S., Krouse, H.R., 1982. Isotopic abundances of water of crystallization of gypsum from the Miocene evaporite formation, Carpathian Foredeep, Poland. Geochim. Cosmochim. Acta 46, 293–296.

Hardie, L.A., 1990. The roles of rifting and hydrothermal $CaCl_2$ brines in the origin of potash evaporites: an hypothesis. Am. J. Sci. 290, 43–106.

Hardie, L.A., 1967. The gypsum-anhydrite equilibrium at one atmosphere pressure. Am. Mineral. 52, 171–200.

Hardie, L.A., Eugster, H.P., 1980. Evaporation of Seawater: Calculated Mineral Sequences. Science. 208, 498–500.

Hartley, A.J., 2003. Andean uplift and climate change. J. Geol. Soc. London. 160, 7–10.

Hartley, A.J., Chong, G., 2002. Late Pliocene age for the Atacama Desert: Implications for the desertification of western South America. Geology 30, 43–46.

Hartley, A.J., Chong, G., Houston, J., Mather, A.E., 2005. 150 million years of climatic stability: evidence from the Atacama Desert, northern Chile. J. Geol. Soc. London. 162, 421–424.

Hartley, A.J., Evenstar, L., 2010. Cenozoic stratigraphic development in the north Chilean forearc: Implications for basin development and uplift history of the Central Andean margin. Tectonophysics 495, 67–77.

Hartley, A.J., Jolley, E.J., 1995. Tectonic implications of late Cenozoic sedimentation from the Coastal Cordillera of northern Chile (22-24°S). J. Geol. Soc. 152, 51–63.

Hartley, A.J., May, G., Chong, G., Turner, P., Kape, S.J., Jolley, E.J., 2000. Development of a continental forearc: A Cenozoic example from the Central Andes, northern Chile. Geology 28, 331–334.

Haschke, M., Siebel, W., Günther, A., Scheuber, E., 2002. Repeated crustal thickening and recycling during the Andean orogeny in north Chile (21°-26°S). J. Geophys. Res. Solid Earth 107.

Herwartz, D., Surma, J., Voigt, C., Assonov, S., Staubwasser, M., 2017. Triple oxygen isotope systematics of structurally bonded water in gypsum. Geochim. Cosmochim. Acta 209, 254–266.

Hodell, D.A., Turchyn, A. V., Wiseman, C.J., Escobar, J., Curtis, J.H., Brenner, M., Gilli, A., Mueller, A.D., Anselmetti, F., Ariztegui, D., Brown, E.T., 2012. Late Glacial temperature and precipitation changes in the lowland Neotropics by tandem measurement of $\delta^{18}O$ in biogenic carbonate and gypsum hydration water. Geochim. Cosmochim. Acta 77, 352–368.

Hoffmeister, D., 2018. Meteorological and soil measurements of the permanent weather stations in the Atacama desert, Chile. [https://doi.org/10.5880/CRC1211DB.1]. CRC1211 Database (CRC1211DB).

Hoke, G.D., Isacks, B.L., Jordan, T.E., Yu, J.S., 2004. Groundwater-sapping origin for the giant quebradas of northern Chile. Geology 32, 605–608.

Horita, J., 1989. Stable isotope fractionation factors of water in hydrated saline mineral-brine systems. Earth Planet. Sci. Lett. 95, 173–179.

Horita, J., 2005. Saline waters, in: Aggarwal, P.K., Gat, J.R., Froehlich, K.F.O., Isotopes in the Water Cycle: Past, Present and Future of a Developing Science. IEA, 271–287.

Horita, J., Cole, D.R., Wesolowski, D.J., 1993. The activity-composition relationship of oxygen and hydrogen isotopes in aqueous salt solutions: II. Vapor-liquid water equilibration of mixed salt solutions from 50 to 100°C and geochemical implications. Geochim. Cosmochim. Acta 57, 4703–4711.

Horita, J., Rozanski, K., Cohen, S., 2008. Isotope effects in the evaporation of water: a status report of the Craig-Gordon model. Isotopes Environ. Health Stud. 44, 23–49.

Horita, J., Wesolowski, D.J., 1994. Liquid-vapor fractionation of oxygen and hydrogen isotopes of water from the freezing to the critical temperature. Geochim. Cosmochim. Acta 58, 3425–3437.

Houston, J., 2006. Variability of precipitation in the Atacama Desert: Its causes and hydrological impact. Int. J. Climatol. 26, 2181–2198.

Houston, J., Hartley, A.J., 2003. The central andean west-slope rainshadow and its potential contribution to the origin of hyper-aridity in the Atacama Desert. Int. J. Climatol. 23, 1453–1464.

Jayne, R.S., Pollyea, R.M., Dodd, J.P., Olson, E.J., Swanson, S.K., 2016. Spatial and temporal constraints on regional-scale groundwater flow in the Pampa del Tamarugal Basin, Atacama Desert, Chile. Hydrogeol. J. 24, 1921–1937.

Jeffery, L.M., Poulsen, C.J., Ehlers, T.A., 2012. Impacts of Cenozoic global cooling, surface uplift, and an inland seaway on South American paleoclimate and precipitation $\delta^{18}O$. Bull. Geol. Soc. Am. 124, 335–351.

Jordan, T.E., Kirk-Lawlor, N.E., Nicolás Blanco, P., Rech, J.A., Cosentino, N.J., 2014. Landscape modification in response to repeated onset of hyperarid paleoclimate states since 14 Ma, Atacama Desert, Chile. Bull. Geol. Soc. Am. 126, 1016–1046.

Jordan, T.E., L, C.H., Godfrey, L. V, Colucci, S.J., P, C.G., M, J.U., L, G.G., Paul, J.F., 2019. Isotopic Characteristics and Paleoclimate Implications of the Extreme Precipitation Event of March 2015 in Northern Chile. Andean Geol. 46, 1–31.

Karátson, D., Telbisz, T., Wörner, G., 2012. Erosion rates and erosion patterns of Neogene to Quaternary stratovolcanoes in the Western Cordillera of the Central Andes: An SRTM DEM based analysis. Geomorphology 139–140, 122–135.

Keene, W.C., Pszenny, A.P., Galloway, N., Hawley, M.E., 1986. Sea-Salt Corrections and Interpretation of Constituent Ratios in Marine Precipitation. J. Geophys. Res. 91, 6647–6658.

Khademi, H., Mermut, A.R., Krouse, H.R., 1997. Isotopic composition of gypsum hydration water in selected landforms from central Iran. Chem. Geol. 138, 245–255.

Kirk-Lawlor, N.E., Jordan, T.E., Rech, J.A., Lehmann, S.B., 2013. Late Miocene to Early Pliocene paleohydrology and landscape evolution of Northern Chile, 19° to 20°S. Palaeogeogr. Palaeoclimatol. Palaeoecol. 387, 76–90.

Koehler, G., Wassenaar, L.I., Hendry, J., 2013. Measurement of stable isotope activities in saline aqueous solutions using optical spectroscopy methods. Isotopes Environ. Health Stud. 49, 378–386.

Lamb, S., Davis, P., 2003. Cenozoic climate change as a possible cause for the rise of the Andes. Nature 425, 792–797.

Lamy, F., Hebbeln, D., Wefer, G., 1998. Terrigenous sediment supply along the Chilean continental margin: Modern regional patterns of texture and composition. Geol. Rundschau 87, 477–494.

Lamy, Klump, Hebbeln, Wefer, 2000. Late Quaternary rapid climate change in northern Chile. Terra Nov. 12, 8–13.

Landais, A., Barkan, E., Yakir, D., Luz, B., 2006. The triple isotopic composition of oxygen in leaf water. Geochim. Cosmochim. Acta 70, 4105–4115.

Landais, A., Barkan, E., Luz, B., 2008. Record of $\delta^{18}O$ and ^{17}O-excess in ice from Vostok Antarctica during the last 150,000 years. Geophys. Res. Lett. 35, 1–5.

Landais, A., Risi, C., Bony, S., Vimeux, F., Descroix, L., Falourd, S., Bouygues, A., 2010. Combined measurements of $^{17}O_{excess}$ and d-excess in African monsoon precipitation: Implications for evaluating convective parameterizations. Earth Planet. Sci. Lett. 298, 104–112.

Latorre, C., Betancourt, J.L., Arroyo, M.T.K., 2006. Late Quaternary vegetation and climate history of a perennial river canyon in the Río Salado basin (22°S) of Northern Chile. Quat. Res. 65, 450–466.

Li, J., Li, M., Fang, X., Zhang, G., Zhang, W., Liu, X., 2017. Isotopic composition of gypsum hydration water in deep Core SG-1, western Qaidam basin (NE Tibetan Plateau), implications for paleoclimatic evolution. Glob. Planet. Change 155, 70–77.

Li, J., Wang, F., Michalski, G., Wilkins, B., 2019. Atmospheric deposition across the Atacama Desert, Chile: Compositions, source distributions, and interannual comparisons. Chem. Geol. 525, 435–446.

Li, S., Levin, N.E., Soderberg, K., Dennis, K.J., Caylor, K.K., 2017. Triple oxygen isotope composition of leaf waters in Mpala, central Kenya. Earth Planet. Sci. Lett. 468, 38–50.

Lowenstein, T.K., Risacher, F., 2009. Closed Basin Brine Evolution and the Influence of Ca-Cl Inflow Waters: Death Valley and Bristol Dry Lake California, Qaidam Basin, China, and Salar de Atacama, Chile. Aquat. Geochemistry 15, 71–94.

Luz, B., Barkan, E., 2010. Variations of $^{17}O/^{16}O$ and $^{18}O/^{16}O$ in meteoric waters. Geochim. Cosmochim. Acta 74, 6276–6286.

Magaritz, M., Aravena, R., Pena, H., Suzuki, O., Grilli, A., 1990. Source of Ground Water in the Deserts of Northern Chile: Evidence of Deep Circulation of Ground Water from the Andes. Groundwater 28, 513–517.

Mathieu, R., Bariac, T., 1996. A numerical model for the simulation of stable isotope profiles in drying soils. J. Geophys. Res. Atmos. 101, 12685–12696.

Matsubaya, O., 1971. Oxygen isotopic fractionation between the water of crystallization of gypsum and the mother solutions. Abstr. Pap. Annu. Meet. Geochem. Soc. Japan (in Japanese).

Matsubaya, O., Sakai, H., 1973. Oxygen and hydrogen isotopic study on the water of crystallization of gypsum from the Kuroko type mineralization. Geochem. J. 7, 153–165.

McKay, C.P., Friedmann, E.I., Gómez-Silva, B., Cáceres-Villanueva, L., Andersen, D.T., Landheim, R., 2003. Temperature and Moisture Conditions for Life in the Extreme Arid Region of the Atacama Desert: Four Years of Observations Including the El Niño of 1997–1998. Astrobiology 3, 393–406.

McKinney, C.R., McCrea, J.M., Epstein, S., Allen, H.A., Urey, H.C., 1950. Improvements in Mass Spectrometers for the Measurement of Small Differences in Isotope Abundance Ratios. Rev. Sci. Instrum. 21.

Merlivat, L., 1978. Molecular diffusivities of $H_2{}^{16}O$, $HD^{16}O$, and $H_2{}^{18}O$ in gases. J. Chem. Phys. 69.

Merlivat, L., Jouzel, J., 1979. Global climatic interpretation of the deuterium-oxygen 18 relationship for precipitation. J. Geophys. Res. 84, 5029–5033.

Michalski, G., Böhlke, J.K., Thiemens, M., 2004. Long term atmospheric deposition as the source of nitrate and other salts in the Atacama Desert, Chile: New evidence from mass-independent oxygen isotopic compositions. Geochim. Cosmochim. Acta 68, 4023–4038.

Miranda, K.M., Espey, M.G., Wink, D.A., 2001. A rapid, simple spectrophotometric method for simultaneous detection of nitrate and nitrite. Nitric Oxide Biol. Chem. 5, 62–71.

Mortimer, C., 1973. The Cenozoic history of the southern Atacama Desert, Chile. J. Geol. Soc. London. 129, 505–526.

Murray, R.C., 1964. Origin and diagenesis of gypsum and anhydrite. J. Sediment. Petrol. 34, 512–523.

Nester, P.L., Gayo, E., Latorre, C., Jordan, T.E., Blanco, N., 2007. Perennial stream discharge in the hyperarid Atacama Desert of northern Chile during the latest Pleistocene. Proc. Natl. Acad. Sci. 104, 19724–19729.

Nishiizumi, K., Caffee, M.W., Finkel, R.C., Brimhall, G., Mote, T., 2005. Remnants of a fossil alluvial fan landscape of Miocene age in the Atacama Desert of northern Chile using cosmogenic nuclide exposure age dating. Earth Planet. Sci. Lett. 237, 499–507.

Oerter, E.J., Singleton, M., Davisson, M.L., 2018. Hydrogen and oxygen stable isotope dynamics of hyper-saline and salt-saturated aqueous solutions. Geochim. Cosmochim. Acta 238, 316–328.

Oi, T., Morimoto, H., 2013. Oxygen and hydrogen isotopic preference in hydration spheres of chloride and sulfate ions. Zeitschrift fur Phys. Chemie 227, 807–819.

Palacio, S., Azorín, J., Montserrat-Martí, G., Ferrio, J.P., 2014. The crystallization water of gypsum rocks is a relevant water source for plants. Nat. Commun. 5, 1–7.

Passey, B.H., Ji, H., 2019. Triple oxygen isotope signatures of evaporation in lake waters and carbonates: A case study from the western United States. Earth Planet. Sci. Lett. 518, 1–12.

Pérez-Fodich, A., Reich, M., Álvarez, F., Snyder, G.T., Schoenberg, R., Vargas, G., Muramatsu, Y., Fehn, U., 2014. Climate change and tectonic uplift triggered the formation of the atacama desert's giant nitrate deposits. Geology 42, 251–254.

Peters, L.I., Yakir, D., 2010. A rapid method for the sampling of atmospheric water vapour for isotopic analysis. Rapid Commun. Mass Spectrom. 24, 103–108.

Pfeiffer, M., Latorre, C., Gayo, E., Amundson, R., 2019. Rare calcium chloride-rich soil and implications for the existence of liquid water in a hyperarid environment. Geology 47, 163–166.

Pfuhl, H.A., McCave, I.N., 2005. Evidence for late Oligocene establishment of the Antarctic Circumpolar Current. Earth Planet. Sci. Lett. 235, 715–728.

Pierchala, A., Rozanski, K., Dulinski, M., Gorczyca, Z., Marzec, M., Czub, R., 2019. High-precision measurements of $\delta^{2}H$, $\delta^{18}O$ and $\delta^{17}O$ in water with the aid of cavity ring-down laser spectroscopy. Isotopes Environ. Health Stud. 55, 290–307.

Placzek, C.J., Matmon, A., Granger, D.E., Quade, J., Niedermann, S., 2010. Evidence for active landscape evolution in the hyperarid Atacama from multiple terrestrial cosmogenic nuclides. Earth Planet. Sci. Lett. 295, 12–20.

Playà, E., Recio, C., Mitchell, J., 2005. Extraction of gypsum hydration water for oxygen isotopic analysis by the guanidine hydrochloride reaction method. Chem. Geol. 217, 89–96.

Raju, K.U.G., Atkinson, G., 1990. The Thermodynamics of "Scale" Mineral Solubilities: 3. Calcium Sulfate in Aqueous NaCI. J. Chem. Eng. Data 35, 361–367.

Rech, J.A., Currie, B.S., Jordan, T.E., Riquelme, R., Lehmann, S.B., Kirk-Lawlor, N.E., Li, S., Gooley, J.T., 2019. Massive middle Miocene gypsic paleosols in the Atacama Desert and the formation of the Central Andean rain-shadow. Earth Planet. Sci. Lett. 506, 184–194.

Rech, J.A., Currie, B.S., Michalski, G., Cowan, A.M., 2006. Neogene climate change and uplift in the Atacama Desert, Chile. Geology 34, 761–764.

Rech, J.A., Quade, J., Hart, W.S., 2003. Isotopic evidence for the source of Ca and S in soil gypsum, anhydrite and calcite in the Atacama Desert, Chile. Geochim. Cosmochim. Acta 67, 575–586.

Reich, M., Bao, H., 2018. Nitrate Deposits of the Atacama Desert: A Marker of Long-Term Hyperaridity. Elements 14, 251–256.

Risacher, F., Alonso, H., Salazar, C., 2003. The origin of brines and salts in Chilean salars: A hydrochemical review. Earth-Science Rev. 63, 249–293.

Ritter, B., Binnie, S.A., Stuart, F.M., Wennrich, V., Dunai, T.J., 2018a. Evidence for multiple Plio-Pleistocene lake episodes in the hyperarid Atacama Desert. Quat. Geochronol. 44, 1–12.

Ritter, B., Stuart, F.M., Binnie, S.A., Gerdes, A., Wennrich, V., Dunai, T.J., 2018b. Neogene fluvial landscape evolution in the hyperarid core of the Atacama Desert. Sci. Rep. 8, 1–16.

Rojas, M., Moreno, P., Kageyama, M., Crucifix, M., Hewitt, C., Abe-Ouchi, A., Ohgaito, R., Brady, E.C., Hope, P., 2009. The Southern Westerlies during the last glacial maximum in PMIP2 simulations. Clim. Dyn. 32, 525–548.

Rozanski, K., Froehlich, K., Mook, W.G., 2001. Surface Water. Tech. Doc. Hydrol. III, 1–115.

Sáez, A., Cabrera, L., Garcés, M., Bogaard, P. van den, Jensen, A., Gimeno, D., 2012. The stratigraphic record of changing hyperaridity in the Atacama desert over the last 10 Ma. Earth Planet. Sci. Lett. 355–356, 32–38.

Sáez, A., Cabrera, L., Jensen, A., Chong, G., 1999. Late Neogene lacustrine record and palaeogeography in the Quillagua – Llamara basin, Central Andean fore-arc (northern Chile). Palaeogeogr. Palaeoclimatol. Palaeoecol. 151, 5–37.

Schauer, A.J., Schoenemann, S.W., Steig, E.J., 2016. Routine high-precision analysis of triple water-isotope ratios using cavity ring-down spectroscopy. Rapid Commun. Mass Spectrom. 30, 2059–2069.

Scher, H.D., Whittaker, J.M., Williams, S.E., Latimer, J.C., Kordesch, W.E.C., Delaney, M.L., 2015. Onset of Antarctic Circumpolar Current 30 million years ago as Tasmanian Gateway aligned with westerlies. Nature 523, 580–583.

Schoenemann, S.W., Schauer, A.J., Steig, E.J., 2013. Measurement of SLAP2 and GISP $\delta^{17}O$ and proposed VSMOW-SLAP normalization for $\delta^{17}O$ and $^{17}O_{excess}$. Rapid Commun. Mass Spectrom. 27, 582–590.

Schrag, D.P., Adkins, J.F., McIntyre, K., Alexander, J.L., Hodell, D.A., Charles, C.D., McManus, J.F., 2002. The oxygen isotopic composition of seawater during the Last Glacial Maximum. Quat. Sci. Rev. 21, 331–342.

Schween, J.H., Hoffmeister, D., Löhnert, U., 2020. Filling the observational gap in the Atacama Desert with a new network of climate stations. Glob. Planet. Change 184, 103034.

Seinfeld, J.H., Pandis, S.N., 2006. Atmospheric Chemistry and Physics: Form Air Pollution to Climate Change. John Wiley & Sons. Inc., New York.

Sengupta, S., Pack, A., 2018. Triple oxygen isotope mass balance for the Earth's oceans with application to Archean cherts. Chem. Geol. 495, 18–26.

Seufert, S., Hesse, C., Goetz-Neunhoeffer, F., Neubauer, J., 2009. Quantitative determination of anhydrite III from dehydrated gypsum by XRD. Cem. Concr. Res. 39, 936–941.

Shackleton, N.J., Kennett, J.P., 1975. Paleotemperature history of the Cenozoic and the initiation of Antarctic glaciation; oxygen and carbon isotope analyses in DSDP sites 277, 279 and 281. Initial. Rep. Deep Sea Drill. Proj. 29, 743-755.

Sharp, Z., 2017. Principles of Stable Isotope Geochemistry, 2nd Edition. [https://doi.org/10.25844/h9q1-0p82]

Sillitoe, R.H., McKee, E.H., 1996. Age of supergene oxidation and enrichment in the Chilean porphyry copper province. Econ. Geol. 91, 164–179.

Sofer, Z., 1978. Isotopic composition of hydration water in gypsum. Geochim. Cosmochim. Acta 42, 1141–1149.

Sofer, Z., Gat, J.R., 1975. The isotope composition of evaporating brines: Effect of the isotopic activity ratio in saline solutions. Earth Planet. Sci. Lett. 26, 179–186.

Sofer, Z., Gat, J.R., 1972. Activities and concentrations of oxygen-18 in concentrated aqueous salt solutions: Analytical and geophysical implications. Earth Planet. Sci. Lett. 15, 232–238.

Steig, E.J., Gkinis, V., Schauer, A.J., Schoenemann, S.W., Samek, K., Hoffnagle, J., Dennis, K.J., Tan, S.M., 2014. Calibrated high-precision ^{17}O-excess measurements using cavity ring-down spectroscopy with laser-current-tuned cavity resonance. Atmos. Meas. Tech. 7, 2421–2435.

Stein, A.F., Draxler, R.R., Rolph, G.D., Stunder, B.J.B., Cohen, M.D., Ngan, F., 2015. NOAA's HYSPLIT atmospheric transport and dispersion modeling system. Bull. Am. Meteorol. Soc. 96, 2059–2077.

Stuut, J.B.W., Lamy, F., 2004. Climate variability at the southern boundaries of the Namib (southwestern Africa) and Atacama (northern Chile) coastal deserts during the last 120,000 yr. Quat. Res. 62, 301–309.

Sun, T., Bao, H., Reich, M., Hemming, S.R., 2018. More than ten million years of hyper-aridity recorded in the Atacama Gravels. Geochim. Cosmochim. Acta 227, 123–132.

Surma, J., Assonov, S., Bolourchi, M.J., Staubwasser, M., 2015. Triple oxygen isotope signatures in evaporated water bodies from the Sistan Oasis, Iran. Geophys. Res. Lett. 42, 8456–8462.

Surma, J., Assonov, S., Herwartz, D., Voigt, C., Staubwasser, M., 2018. The evolution of ^{17}O-excess in surface water of the arid environment during recharge and evaporation. Sci. Rep. 8, 1–10.

Tan, H.B., Huang, J.Z., Zhang, W.J., Liu, X.Q., Zhang, Y.F., Kong, N., Zhang, Q., 2014. Fractionation of hydrogen and oxygen isotopes of gypsum hydration water and assessment of its geochemical indications. Aust. J. Earth Sci. 61, 793–801.

Taube, H., 1954. Use of Oxygen Isotope Effects in Study of Hydration of Ions. J. Phys. Chem. 58, 523–528.

Trenberth, K.E., Fasullo, J.T., Kiehl, J., 2009. Earth's global energy budget. Bull. Am. Meteorol. Soc. 90, 311–323.

Uemura, R., Barkan, E., Abe, O., Luz, B., 2010. Triple isotope composition of oxygen in atmospheric water vapor. Geophys. Res. Lett. 37, 1–4

Uemura, R., Matsui, Y., Yoshimura, K., Motoyama, H., Yoshida, N., 2008. Evidence of deuterium excess in water vapor as an indicator of ocean surface conditions. J. Geophys. Res. Atmos. 113, 1–10.

Uribe, J., Muñoz, J.F., Gironás, J., Oyarzún, R., Aguirre, E., Aravena, R., 2015. Assessing groundwater recharge in an Andean closed basin using isotopic characterization and a rainfall-runoff model: Salar del Huasco basin, Chile. Hydrogeol. J. 23, 1535–1551.

van Driessche, A.E., Stawski, T.M., Benning, L.G., Kellermeier, M., 2017. Calcium sulfate precipitation throughout its phase diagram, in: van Driessche, A.E., Kellermeier, M., Benning, L.G., Gebauer, D. (Eds.), New Perspectives on Mineral Nucleation and Growth. Springer US, 227–256.

Victor, P., Sobiesiak, M., Glodny, J., Nielsen, S.N., Oncken, O., 2011. Long-term persistence of subduction earthquake segment boundaries: Evidence from Mejillones Peninsula, northern Chile. J. Geophys. Res. Solid Earth 116, 1–22.

Vuille, M., Bradley, R.S., Keimig, F., 2000. Climate variability in the Andes of Ecuador and its relation to tropical Pacific and Atlantic Sea Surface temperature anomalies. J. Clim. 13, 2520–2535.

Walvoord, M.A., Phillips, F.M., Stonestrom, D.A., Evans, D.R., Hartsough, P.C., Newman, B.D., Striegl, R.G., 2003. A Reservoir of Nitrate Beneath Desert Soils. Science. 302, 1021–1025.

Wang, F., Michalski, G., Seo, J. hye, Ge, W., 2014. Geochemical, isotopic, and mineralogical constraints on atmospheric deposition in the hyper-arid Atacama Desert, Chile. Geochim. Cosmochim. Acta 135, 29–48.

Wara, M.W., Ravelo, A.C., Delaney, M.L., 2005. Climate change: Permanent El Niño-like conditions during the Pliocene warm period. Science. 309, 758–761.

Warren, J.K., 2010. Evaporites through time: Tectonic, climatic and eustatic controls in marine and nonmarine deposits. Earth Sci. Rev. 98, 217–268.

Wörner, G., Uhlig, D., Kohler, I., Seyfried, H., 2002. Evolution of the West Andean Escarpment at 18°S (N. Chile) during the last 25 Ma: Uplift, erosion and collapse through time. Tectonophysics 345, 183–198.

Appendix

A.1 Supplementary material to Chapter 5

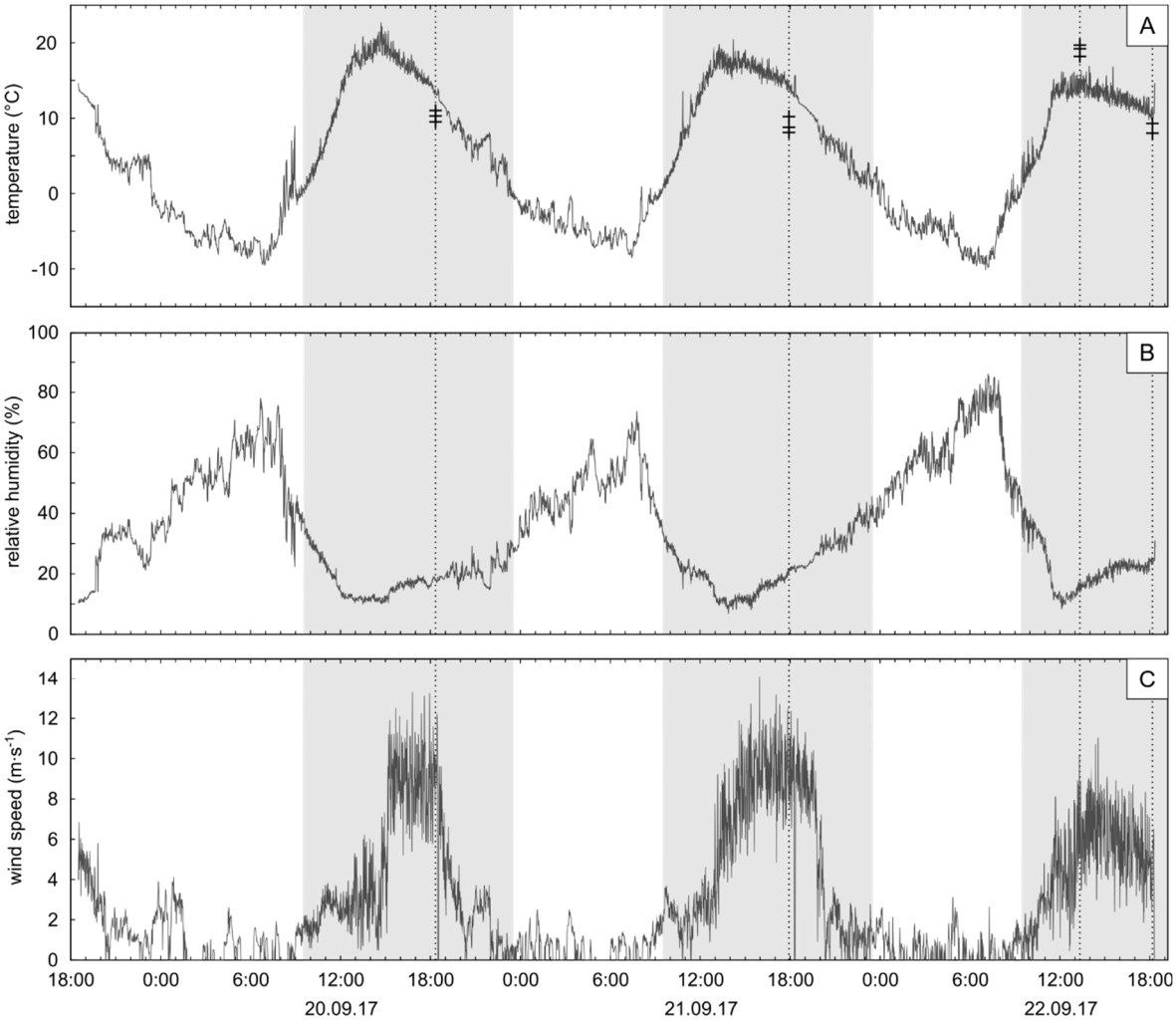

Figure A1.1: Temperature (A), relative humidity (B), and wind speed (C) over the period of the evaporation experiment. Shaded areas indicate time intervals, where temperatures exceed 0°C and waters are assumed to be not frozen. Dashed lines show time of sampling. Crosses in chart A represent water temperatures measured during sampling. While water temperatures are lower than air in the evening, they can exceed air temperatures during midday.

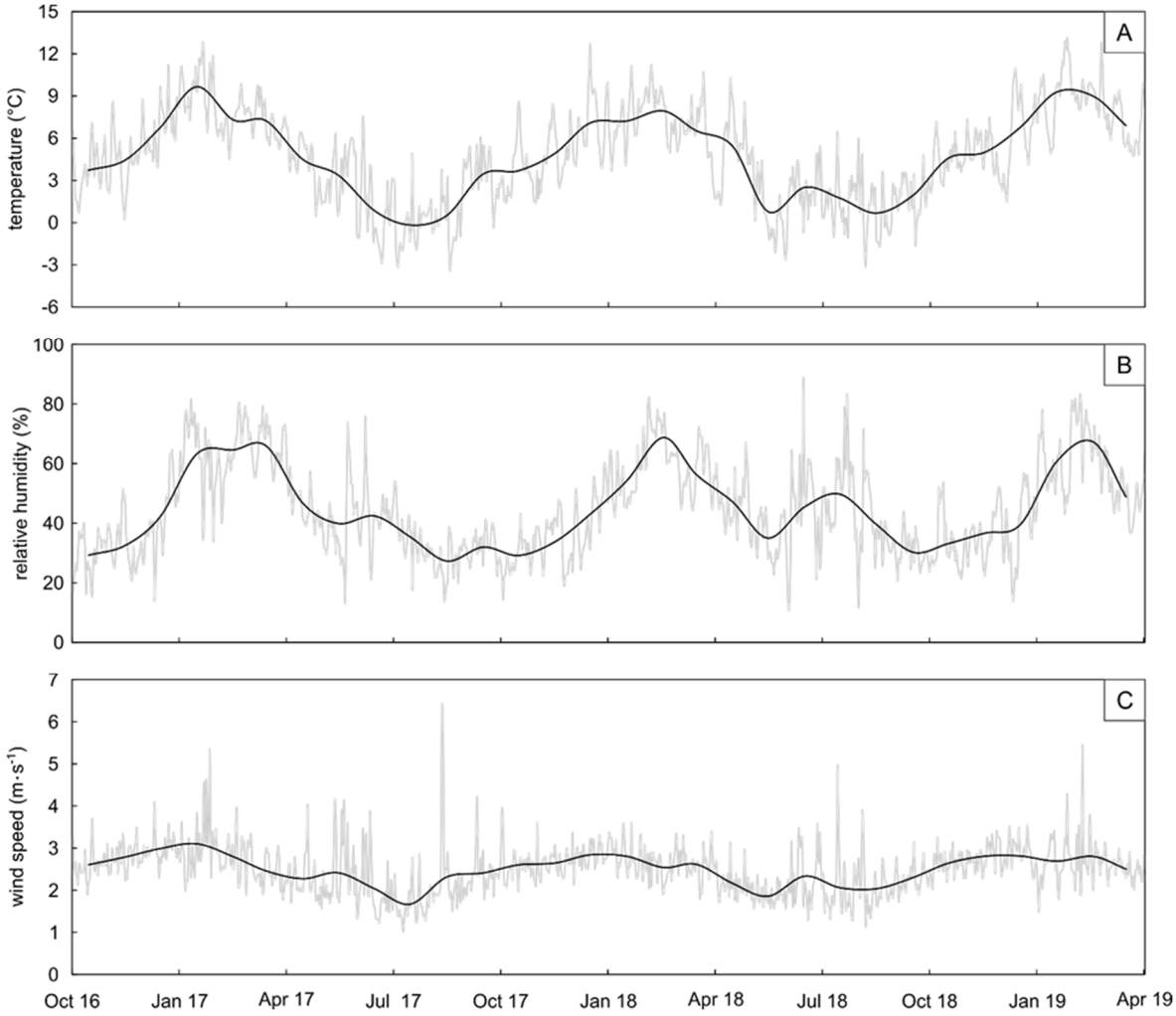

Figure A1.2: Temperature (A), relative humidity (B), and wind speed (C) conditions between October 2016 and March 2019 (data from CEAZA, 2019). Black lines mark monthly average conditions, while grey lines indicate daily variations.

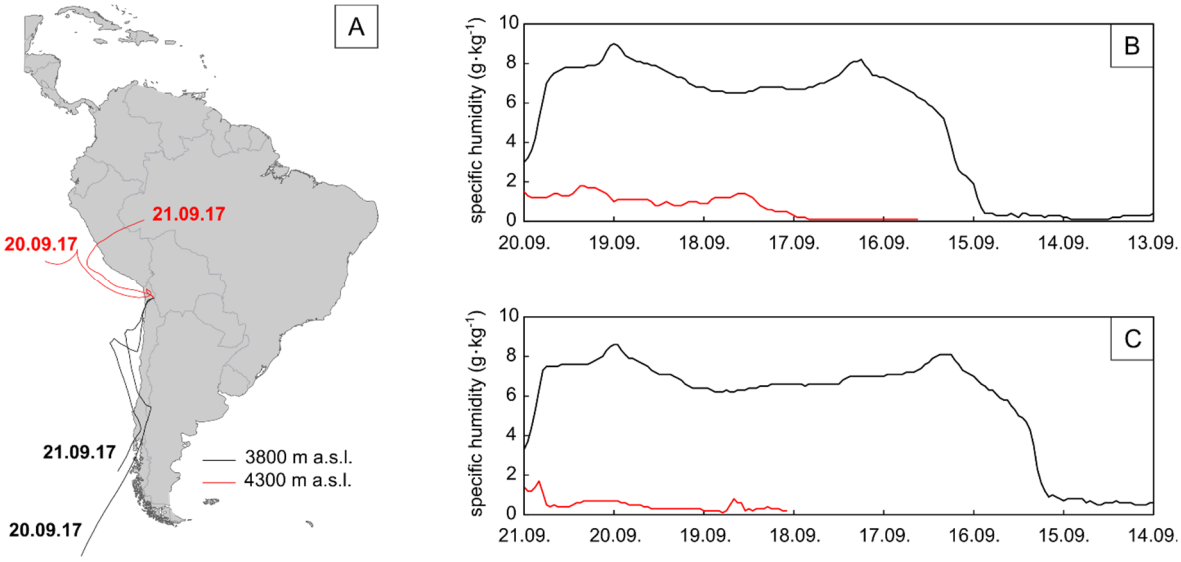

Figure A1.3: HYSPLIT 7-day air mass back trajectories (A) modeled for ground level (black) and 1500 m above ground level (red) at the Salar del Huasco for the start time of vapor extractions (18:00) on 20.09.17 and 21.09.2017. Panel B and C show the specific humidity of the respective air masses.

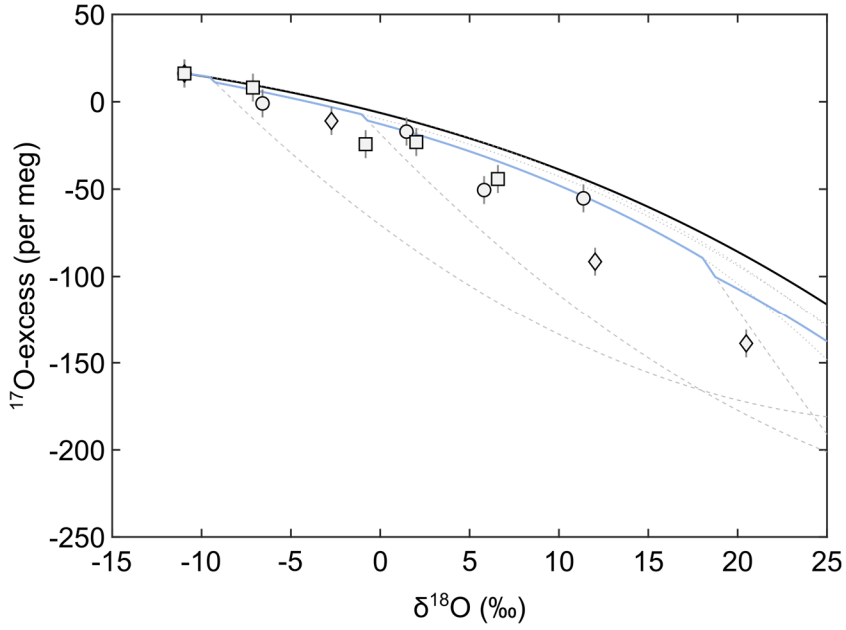

Figure A1.4: Example of isotope effects associated with mixing that might occur during thawing. The black curve indicates the mean evaporation trajectory without mixing. The blue curve shows the evaporation trajectory for the example of an initial volume of 600 ml with mixing. The curve is modeled using evaporation rates based on measured residual fractions and assuming that 30 ml of the ice thawed in the morning, evaporated to 90 % and mixed with the residual water. Mixing ratios are < 1% at the beginning of the experiment but become significant with decreasing volume of the residual water leading to an overall lowering of ^{17}O-excess of evaporated pan waters with respect to the predicted simple evaporation trendline.

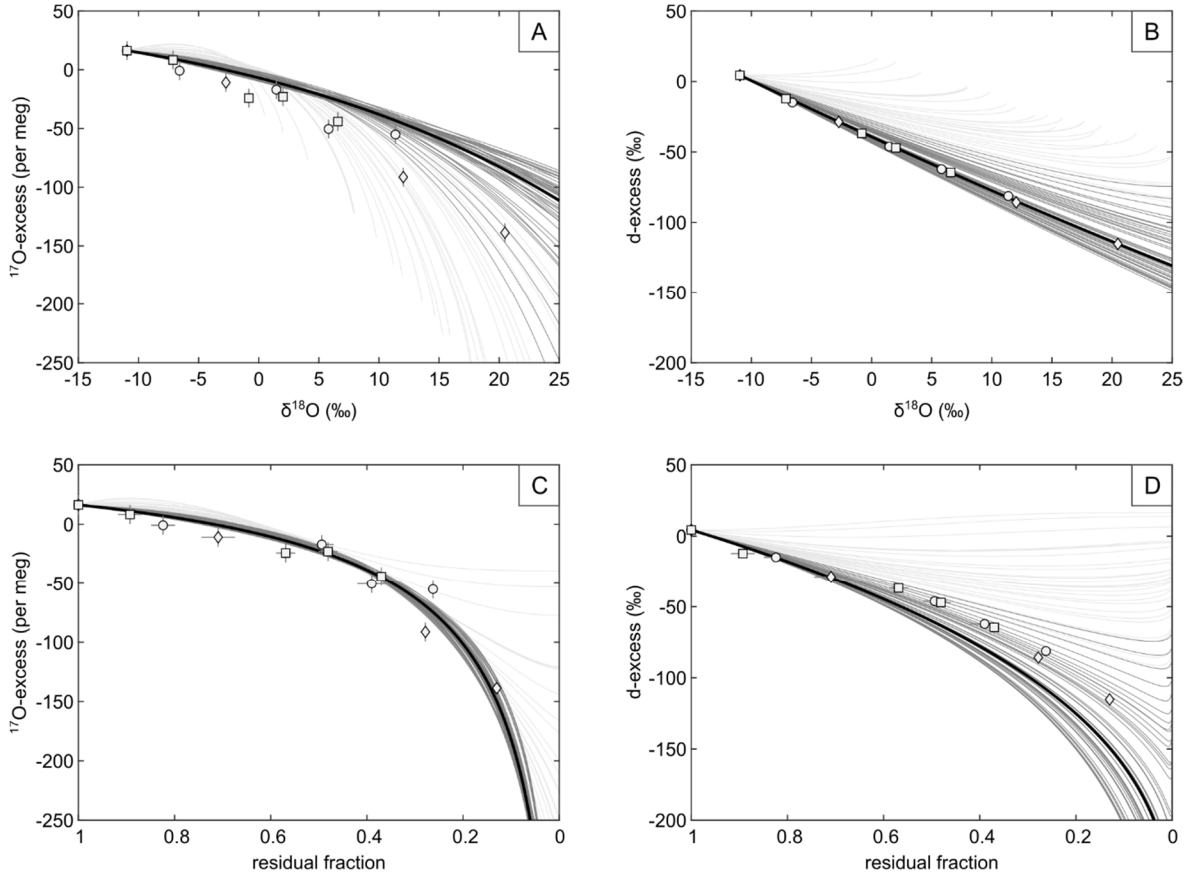

Figure A1.5: ^{17}O-excess and d-excess vs δ^{18}O (A,B) and residual fraction (C,D) for pan evaporation experiments with initial volume of 600 ml (diamonds), 800 ml (circles), 1000 ml (squares). The symbol size is larger than error bars. Simple evaporation trajectories were modeled in hourly resolution for the period of the evaporation experiment (dark grey lines for hourly average T > 0°C and light grey lines for hourly average T < 0°C). The solid line represents the mean simple evaporation trajectory for T > 0°C. The model input parameters are summarized in Table 5.1 in the main text.

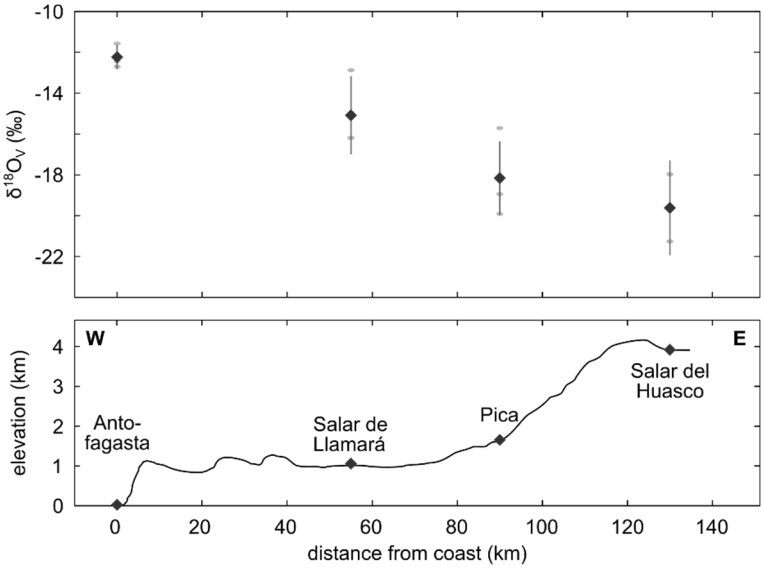

Figure A1.6: Variability of the isotopic composition of atmospheric vapor in the Atacama Desert with distance from the Pacific Coast. Atmospheric vapor was measured several times at different sites (from west to east): Antofagasta, Salar de Llamará, Pica and Salar de Huasco (grey dots). Black diamonds represent average values for the specific sites.

A1.1 Hydrogeochemical composition

Natural waters in the Salar del Huasco span a wide range in total dissolved solids (TDS) from 0.4 $g \cdot l^{-1}$ up to 343 $g \cdot l^{-1}$. Springs are fresh with an average TDS of 0.7 ± 0.5 $g \cdot l^{-1}$. Ponds in the SE and NW areas of the Salar del Huasco comprise generally low salinity in the range of brackish waters. Hypersaline waters are observed in the N area with most of the ponds having TDS values higher than 100 $g \cdot l^{-1}$.

Major ion analyses reveal that the waters originate from two source types (Fig. A1.7). All spring waters are dominated by calcium and sodium. However, springs at the western margin of the salar are of bicarbonate composition, while the spring at the south-eastern end of the salar classify as sulfate type. The difference in hydrogeochemical composition of spring waters is probably attributed to the aquifers. The calcium-sodium bicarbonate composition of western springs is associated with ignimbrite deposits in the north of the Salar del Huasco (Flores Grandez, 2010). The sulfate-rich composition of the south-eastern spring is linked to volcanic units in the east of the Salar del Huasco (Flores Grandez, 2010).

The hydrogeochemical composition of lakes and ponds is related to their source (Fig. A1.7). Evaporation leads to the enrichment of the dissolved ions in the waters, precipitation of carbonates, sodium sulfates and chlorides at the saturation limit, and the transition to sodium-chloride type waters. Furthermore, dissolution of older evaporitic units may contribute to the high sodium chloride concentrations especially in the northern area of the Salar del Huasco.

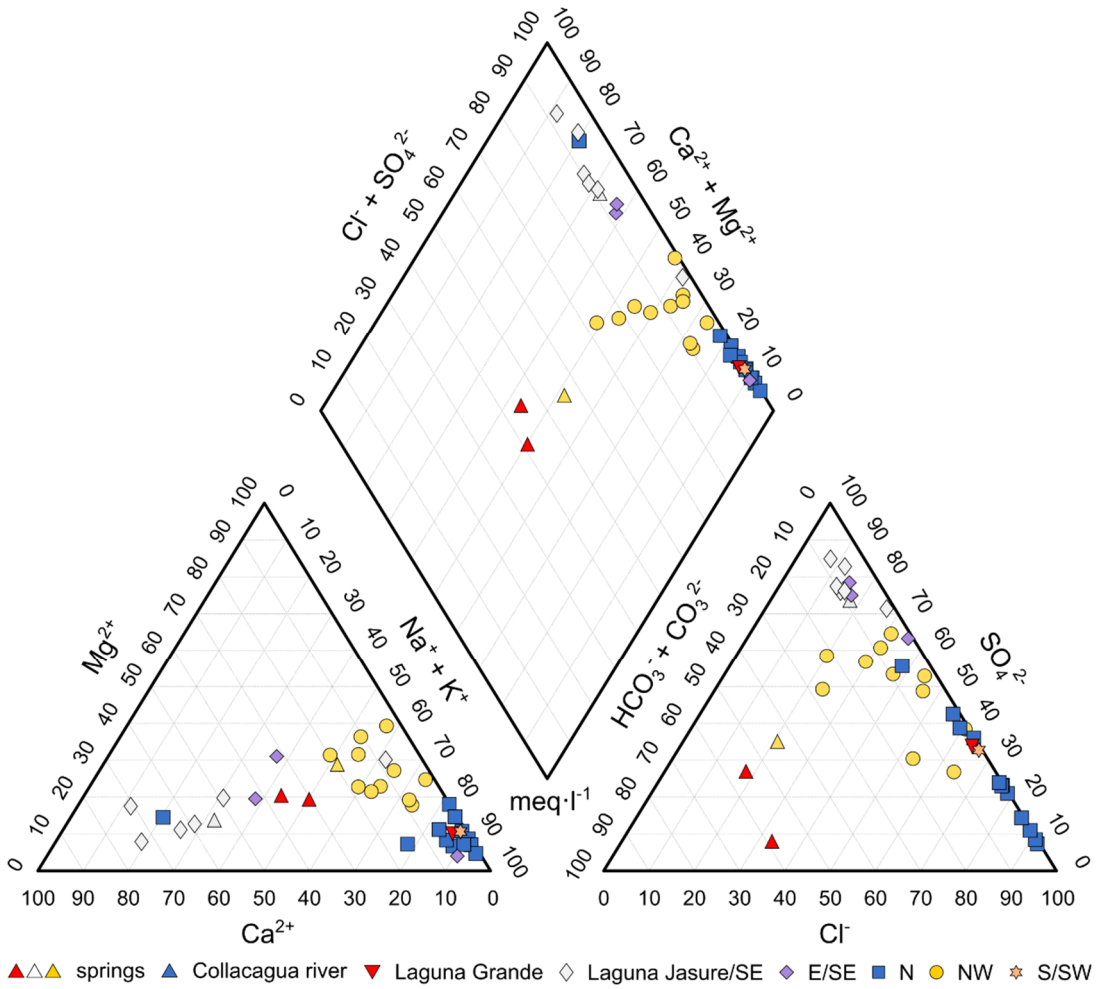

Figure A1.7: Hydrogeochemical composition of springs, ponds and lakes sampled in 09/17 at the Salar del Huasco. Symbology refers to sample type and the corresponding hydrological subsystem.

Table A1.1: Hydrogeochemical composition of sampled natural waters from the Salar del Huasco.

sample	latitude	longitude	elevation (m asl)	pH	TDS ($g \cdot l^{-1}$)	Na ($g \cdot l^{-1}$)	K ($g \cdot l^{-1}$)	Ca ($g \cdot l^{-1}$)	Mg ($g \cdot l^{-1}$)	Cl ($g \cdot l^{-1}$)	S ($g \cdot l^{-1}$)	HCO_3 ($g \cdot l^{-1}$)	CO_3 ($g \cdot l^{-1}$)
springs													
09/2017													
Ata17-192	20° 15.166' S	68° 52.116' W	3794	7.69	0.44	0.08	0.01	0.02	0.01	0.04	0.04	0.23	0.00
Ata17-212	20° 15.770' S	68° 52.527' W	3776	7.84	0.43	0.06	0.01	0.04	0.01	0.03	0.03	0.25	0.00
Ata17-214	20° 16.983' S	68° 53.366' W	3780	8.04	1.39	0.08	0.01	0.04	0.01	0.20	0.03	1.02	0.01
Ata17-216	20° 20.229' S	68° 48.937' W	3789	7.88	0.38	0.06	0.01	0.09	0.01	0.04	0.11	0.06	0.00
09/2018													
Ata18-044	20° 16.969' S	68° 53.374' W	3779	7.40	0.39	0.07	0.01	0.04	0.01	0.03	0.03	0.21	0.00
Ata18-048	20° 18.307' S	68° 53.273' W	3781	8.20	0.70	0.12	0.01	0.08	0.01	0.08	0.05	0.34	0.01
Ata18-050	20° 18.296' S	68° 53.234' W	3782	8.45	2.11	0.47	0.08	0.09	0.09	0.31	0.24	0.81	0.02
Ata18-063	20° 20.229' S	68° 48.937' W	3789	7.93	0.38	0.07	0.01	0.09	0.01	0.03	0.11	0.05	0.00
Ata18-066	20° 15.165' S	68° 52.114' W	3793	7.72	0.42	0.08	0.01	0.05	0.01	0.03	0.05	0.19	0.00
Ata18-069	20° 16.565' S	68° 53.210' W	3787	8.76	0.34	0.07	0.00	0.03	0.01	0.04	0.02	0.17	0.00
Ata18-070	20° 15.770' S	68° 52.527' W	3776	7.80	0.40	0.07	0.01	0.04	0.01	0.03	0.03	0.20	0.00
03/2019													
Ata19-024	20° 20.228' S	68° 48.939' W	3788	8.26	-	-	-	-	-	-	-	-	-
Ata19-035	20° 20.220' S	68° 50.299' W	3785	-	-	-	-	-	-	-	-	-	-
Ata19-116	20° 15.165' S	68° 52.115' W	3793	7.83	0.55	0.11	0.02	0.05	0.01	0.08	0.06	0.20	0.00
Ata19-123	20° 15.745' S	68° 52.556' W	3793	8.12	-	-	-	-	-	-	-	-	-
Ata19-126	20° 16.986' S	68° 53.358' W	3782	8.02	0.38	0.07	0.01	0.04	0.01	0.04	0.03	0.19	0.00
Rio Collacagua													
09/2018													
Ata18-065	20° 06.175' S	68° 50.603' W	3855	8.35	0.48	0.07	0.01	0.04	0.02	0.03	0.02	0.28	0.01
03/2019													
Ata19-021	20° 06.171' S	68° 50.603' W	3850	8.28	0.51	0.07	0.01	0.05	0.02	0.03	0.03	0.29	0.00

(continued)

sample	latitude	longitude	elevation (m asl)	pH	TDS ($g \cdot l^{-1}$)	Na ($g \cdot l^{-1}$)	K ($g \cdot l^{-1}$)	Ca ($g \cdot l^{-1}$)	Mg ($g \cdot l^{-1}$)	Cl ($g \cdot l^{-1}$)	S ($g \cdot l^{-1}$)	HCO_3 ($g \cdot l^{-1}$)	CO_3 ($g \cdot l^{-1}$)
Laguna Grande													
09/2017													
Ata17-213	20° 16.422' S	68° 52.974' W	3777	8.74	19.75	6.92	1.24	0.21	0.24	7.95	2.59	0.59	0.01
09/2018													
Ata18-089	20° 16.433' S	68° 53.034' W	3785	8.42	-	-	-	-	-	-	-	-	-
03/2019													
Ata19-124	20° 16.427' S	68° 53.047' W	3784	8.73	36.23	13.24	2.28	0.60	0.33	13.24	5.90	0.64	0.01
NW area													
03/2017													
Ata17-181a	20° 15.510' S	68° 52.122' W	2788	8.87	0.63	0.14	0.02	0.05	0.03	0.07	0.09	0.23	0.00
Ata17-182	20° 15.533' S	68° 51.971' W	3787	8.67	6.34	2.15	0.23	0.34	0.22	1.27	1.62	0.50	0.00
Ata17-183	20° 15.472' S	68° 51.905' W	3786	8.92	2.74	0.94	0.15	0.09	0.07	0.57	0.51	0.41	0.00
Ata17-184	20° 15.454' S	68° 51.963' W	3788	8.44	3.20	0.92	0.07	0.21	0.10	0.53	0.64	0.72	0.00
Ata17-185	20° 15.516' S	68° 51.966' W	3789	8.71	3.40	1.06	0.10	0.21	0.10	0.64	0.78	0.51	0.00
Ata17-186	20° 15.398' S	68° 51.968' W	3789	8.36	3.52	1.09	0.05	0.10	0.08	1.30	0.34	0.56	0.00
Ata17-187	20° 15.301' S	68° 52.007' W	3790	8.81	1.12	0.30	0.04	0.05	0.06	0.11	0.21	0.35	0.00
Ata17-188	20° 15.191' S	68° 51.996' W	3792	8.49	39.78	11.83	2.53	0.55	2.40	15.64	6.15	0.68	0.00
Ata17-189a	20° 15.188' S	68° 51.972' W	3791	8.58	8.32	2.65	0.27	0.24	0.32	2.45	1.61	0.78	0.00
Ata17-190	20° 15.159' S	68° 52.010' W	3794	8.64	24.66	8.97	1.35	0.20	0.88	6.95	5.12	1.18	0.01
Ata17-191	20° 15.180' S	68° 52.102' W	3793	8.48	1.11	0.22	0.05	0.04	0.04	0.34	0.12	0.30	0.00
N area													
03/2017													
Ata17-194	20° 17.814' S	68° 49.605' W	3796	7.39	343.11	95.64	38.40	0.07	6.65	189.87	9.34	3.14	0.00
Ata17-195	20° 17.795' S	68° 49.600' W	3797	7.67	268.56	79.00	24.45	0.38	4.18	149.99	8.63	1.93	0.00
Ata17-196	20° 17.815' S	68° 49.644' W	3798	7.73	236.00	71.55	18.96	0.61	2.64	131.02	10.04	1.18	0.00
Ata17-197a	20° 17.816' S	68° 49.639' W	3796	7.85	245.76	82.71	18.30	0.38	2.35	120.83	19.92	1.26	0.00

(continued)

Ata17-198	20° 17.765' S	68° 49.681' W	3792	7.94	201.42	69.47	16.53	0.43	1.60	94.58	17.84	0.96	0.00
Ata17-199	20° 17.765' S	68° 49.686' W	3794	7.93	181.61	69.67	9.92	0.53	1.00	73.90	25.86	0.73	0.00
Ata17-200a	20° 17.740' S	68° 49.700' W	3791	9.29	65.01	20.00	5.00	0.92	0.46	31.99	5.97	0.67	0.00
Ata17-201	20° 17.726' S	68° 49.731' W	3789	9.10	51.30	15.80	4.44	0.85	0.46	24.36	4.79	0.60	0.00
Ata17-202	20° 17.715' S	68° 49.743' W	3790	8.95	11.75	3.68	1.13	0.58	0.10	4.02	1.90	0.33	0.00
Ata17-203	20° 17.716' S	68° 59.759' W	3790	9.12	113.75	36.61	7.89	0.74	0.86	60.35	6.31	0.97	0.01
Ata17-204	20° 17.663' S	68° 49.818' W	3786	8.87	31.30	10.14	3.46	0.60	0.42	11.13	4.51	1.02	0.01
Ata17-205	20° 17.578' S	68° 49.838' W	3789	8.56	2.12	0.19	0.05	0.51	0.04	0.56	0.50	0.27	0.00
03/2019													
Ata19-115	20° 17.578' S	68° 50.071' W	3784	8.27	149.68	45.00	18.75	0.72	1.05	69.47	14.67	0.01	0.02
SE area													
09/2017													
Ata17-217	20° 20.045' S	68° 49.034' W	3789	8.55	0.82	0.11	0.03	0.23	0.01	0.07	0.23	0.14	0.00
Ata17-219	20° 19.730' S	68° 49.081' W	3791	9.20	0.59	0.09	0.02	0.15	0.01	0.05	0.17	0.10	0.00
Ata17-220	20° 19.408' S	68° 49.437' W	3793	8.84	1.10	0.13	0.02	0.39	0.02	0.08	0.36	0.11	0.00
Ata17-222	20° 19.110' S	68° 49.006' W	3793	9.53	17.65	7.24	1.27	0.34	0.09	3.98	4.38	0.34	0.00
Ata17-223	20° 19.114' S	68° 48.990' W	3793	9.63	0.81	0.15	0.06	0.14	0.02	0.09	0.23	0.12	0.00
Ata17-224	20° 19.122' S	68° 49.006' W	3792	7.89	3.80	0.78	0.29	0.56	0.20	0.36	1.15	0.46	0.00
Ata17-225	20° 19.615' S	68° 48.978' W	3789	8.71	0.69	0.12	0.02	0.15	0.02	0.06	0.20	0.11	0.00
Ata17-226	20° 19.749' S	68° 48.962' W	3791	8.37	1.62	0.11	0.03	0.58	0.05	0.08	0.54	0.22	0.00
Ata17-227	20° 19.856' S	68° 48.966' W	3790	8.48	14.76	4.77	1.26	0.51	0.70	2.64	4.35	0.51	0.00
03/2019													
Ata19-031	20° 19.212' S	68° 49.099' W	3781	8.88	95.98	31.62	11.32	0.63	0.91	35.36	15.27	0.84	0.02
Ata19-032	20° 19.353' S	68° 49.059' W	3782	9.40	77.90	26.05	8.58	0.63	1.26	26.52	13.67	1.13	0.05
Ata19-033	20° 19.531' S	68° 49.034' W	3783	9.15	67.34	23.95	4.56	0.86	3.48	14.19	17.86	2.35	0.08

(continued)

sample	latitude	longitude	elevation (m asl)	pH	TDS ($g \cdot l^{-1}$)	Na ($g \cdot l^{-1}$)	K ($g \cdot l^{-1}$)	Ca ($g \cdot l^{-1}$)	Mg ($g \cdot l^{-1}$)	Cl ($g \cdot l^{-1}$)	S ($g \cdot l^{-1}$)	HCO_3 ($g \cdot l^{-1}$)	CO_3 ($g \cdot l^{-1}$)
SW area													
09/2017													
Ata17-215	20° 19.335' S	68° 51.803' W	3778	8.39	117.75	40.67	8.32	0.58	1.44	49.53	15.05	2.13	0.02
09/2018													
Ata18-046a	20° 18.322' S	68° 53.300' W	3782	9.50	1.49	0.36	0.04	0.04	0.05	0.22	0.12	0.64	0.01
Ata18-052	20° 18.298' S	68° 53.093' W	3783	8.56	58.43	18.71	4.33	0.58	0.83	27.40	5.78	0.78	0.01
Ata18-053a	20° 18.227' S	68° 53.284' W	3786	9.59	1.50	0.40	0.07	0.02	0.03	0.21	0.12	0.63	0.02
Ata18-056	20° 19.323' S	68° 51.831' W	3786	8.37	142.73	52.58	9.32	0.53	1.68	54.54	21.70	2.35	0.02
Ata18-058	20° 19.418' S	68° 51.726' W	3787	8.42	102.64	37.72	6.78	0.59	1.30	40.83	14.97	0.44	0.01
Ata18-061	20° 19.426' S	68° 51.775' W	3790	8.01	9.94	3.71	0.63	0.37	0.23	2.08	2.51	0.39	0.01
03/2019													
Ata19-038	20° 18.286' S	68° 53.240' W	3788	-	-	-	-	-	-	-	-	-	-

Table A1.2: Hydrogen and oxygen isotope data derived from pan evaporation experiments.

sample	$\delta^{17}O$ (‰)	SD	$\delta^{18}O$ (‰)	SD	^{17}O- (per meg)	SD	n	$\delta^{2}H$ (‰)	SD	d-excess (‰)	n
initial water	-5.79	0.24	-10.96	0.39	16	6	9	-83.3	1.4	4.4	4
600 ml											
1a	-1.45	0.26	-2.73	0.54	-11	30	7	-50.5	0.5	-27.7	3
1b	6.24	0.29	12.03	0.58	-91	35	7	10.4	0.5	-85.8	3
1c	10.62	0.18	20.48	0.30	-139	36	7	48.6	0.5	-115.2	3
800 ml											
2a	-3.48	0.02	-6.59	0.04	-1	4	3	-67.4		-14.7	1
2b	0.75	0.02	1.47	0.02	-17	6	4	-34.5		-46.2	1
2c	3.01	0.17	5.81	0.32	-50	2	3	-15.7		-62.2	1
2d	5.93	0.22	11.37	0.39	-55	18	3	9.8		-81.2	1
1000 ml											
3a	-3.76	0.05	-7.13	0.10	8	0	3	-69.8		-12.8	1
3b	-0.46	0.02	-0.82	0.06	-24	11	3	-43.7		-37.1	1
3c	1.04	0.01	2.02	0.02	-23	5	2	-31.0		-47.1	1
3d	3.43	0.09	6.58	0.13	-44	17	3	-11.9		-64.6	1

Table A1.3: Oxygen isotopic composition of atmospheric vapor measured at different sites in the Atacama Desert.

Sample site	$\delta^{18}O$ (‰)	SD
Antofagasta		
12.09.2017	-12.6	
25.09.2017	-12.4	
25.09.2017	-11.5	
mean	**-12.2**	**0.6**
Salar de Llamará		
20.03.2017	-16.1	
14.09.2017	-16.1	
15.09.2017	-12.8	
mean	**-15.0**	**1.9**
Pica		
23.03.2017	-19.7	
23.09.2017	-15.6	
16.09.2017	-18.8	
18.09.2017	-17.9	
mean	**-17.4**	**1.6**
Salar del Huasco		
20.09.2017	-21.0	
21.09.2017	-17.8	
mean	**-19.4**	**2.3**

Table A1.4: Hydrogen and oxygen isotope data of sampled lakes and ponds from the Salar del Huasco.

sample	$\delta^{17}O$ (‰)	SD	$\delta^{18}O$ (‰)	SD	^{17}O-excess (per meg)	SD	n	$\delta^{2}H$ (‰)	SD	d-excess	n
springs											
09/2017											
Ata17-192	-6.22	0.02	-11.75	0.04	3	5	2	-95.0	0.8	-1.0	2
Ata17-212	-6.51	0.00	-12.31	0.02	10	6	2	-96.7	1.4	1.8	2
Ata17-214	-6.58	0.18	-12.46	0.36	17	17	5	-97.8	0.4	1.9	2
Ata17-216	-7.02	0.05	-13.28	0.09	15	3	2	-100.2	0.7	6.0	2
mean	**-6.58**	**0.33**	**-12.45**	**0.64**	**11**	**7**		**-97.4**	**2.2**	**2.2**	
09/2018											
Ata18-044	-6.58	0.09	-12.43	0.18	3	6	3	-97.7	0.2	1.8	2
Ata18-048	-6.31	0.15	-11.94	0.29	15	5	3	-96.2		-0.7	1
Ata18-050	-6.83	0.14	-12.91	0.23	9	13	3	-101.0		2.3	1
Ata18-063	-6.89	0.10	-13.03	0.16	7	14	3	-99.1	1.2	5.1	2
Ata18-066	-6.17	0.06	-11.66	0.10	6	10	3	-94.8		-1.5	1
Ata18-069	-6.35	0.08	-12.00	0.13	3	13	3	-95.6		0.4	1
Ata18-070	-6.51	0.05	-12.28	0.11	-5	5	3	-96.1	1.9	2.1	2
mean	**-6.52**	**0.27**	**-12.32**	**0.51**	**5**	**6**		**-97.2**	**2.2**	**1.4**	
03/2019											
Ata19-024	-6.99	0.02	-13.22	0.04	9	3	2	-99.4		6.3	1
Ata19-035	-6.96	0.01	-13.16	0.01	6	5	2	-99.1		6.1	1
Ata19-116	-6.14	0.11	-11.59	0.22	-1	4	3	-87.3		5.4	1
Ata19-123	-6.57	0.02	-12.41	0.04	3	0	2	-97.1		2.2	1
Ata19-126	-6.57	0.07	-12.39	0.15	-6	5	3	-91.7		7.4	1
mean	**-6.65**	**0.35**	**-12.55**	**0.68**	**2**	**6**		**-94.9**	**5.3**	**5.5**	

(continued)

Collacagua river											
09/2018											
Ata18-065	-6.55	0.03	-12.38	0.07	5	9	4	-97.5		1.6	1
03/2019											
Ata19-021	-6.59	0.04	-12.45	0.05	5	15	4	-93.8		5.8	1
Laguna Gande											
09/2017											
Ata17-213	-1.35	0.01	-2.48	0.03	-37	2	2	-49.2	0.0	-29.4	2
09/2018											
Ata18-089	1.65	0.08	3.20	0.13	-39	7	3	-16.3	0.5	-41.9	1
03/2019											
Ata19-124	-2.20	0.10	-4.14	0.18	-15	4	3	-55.1		-21.9	1
NW area											
09/2017											
Ata17-181a	-5.24	0.01	-9.90	0.02	3	4	2	-87.5	0.8	-8.2	2
Ata17-182	-4.07	0.07	-7.69	0.11	-4	13	3	-76.0	0.6	-14.5	2
Ata17-183	-4.00	0.01	-7.55	0.02	-3	2	2	-75.8	0.5	-15.4	2
Ata17-184	-4.89	0.01	-9.26	0.01	12	6	2	-84.6	1.3	-10.5	2
Ata17-185	-4.76		-9.00		7		1	-82.8	1.5	-10.8	2
Ata17-186	-4.54	0.02	-8.59	0.04	2	0	2	-81.3	0.2	-12.6	2
Ata17-187	-4.37		-8.27		11		1	-77.6	0.1	-11.5	2
Ata17-188	-1.06	0.06	-1.94	0.12	-32	9	2	-51.5		-35.9	1
Ata17-189a	-1.85	0.06	-3.46	0.10	-21	7	3	-57.7	0.1	-30.0	2
Ata17-190	-1.26	0.01	-2.31	0.01	-39	1	2	-53.6		-35.0	1
Ata17-191	-3.67	0.06	-6.91	0.10	-11	7	2	-70.7	1.0	-15.4	2

(continued)

sample	$\delta^{17}O$ (‰)	SD	$\delta^{18}O$ (‰)	SD	^{17}O-excess (per meg)	SD	n	$\delta^{2}H$ (‰)	SD	d-excess	n
N area											
09/2017											
Ata17-194	0.04	0.02	0.17	0.04	-54	2	2	-37.4	5.3	-38.8	2
Ata17-195	-0.52	0.18	-0.90	0.35	-38	8	2	-50.2	2.7	-42.9	2
Ata17-196	-0.64	0.08	-1.11	0.16	-50	4	2	-52.5	3.3	-43.6	2
Ata17-197a	-1.20	0.06	-2.21	0.12	-34	6	3	-54.7		-37.1	1
Ata17-198	-1.27	0.00	-2.33	0.01	-36	2	2	-57.5		-38.8	1
Ata17-199	-2.53	0.01	-4.74	0.01	-25	3	2	-65.2		-27.3	1
Ata17-200a	1.96	0.05	3.85	0.09	-67	7	3	-27.5	1.3	-58.3	2
Ata17-201	1.48	0.00	2.94	0.00	-73	4	2	-30.0	1.4	-53.5	2
Ata17-202	-5.63	0.09	-10.65	0.17	7	1	2	-90.4	0.9	-5.3	1
Ata17-203	2.24	0.05	4.34	0.12	-54	12	2	-29.7	1.3	-64.4	2
Ata17-204	-0.66	0.02	-1.20	0.04	-29	1	2	-44.4		-34.8	1
Ata17-205	-5.55	0.02	-10.51	0.05	16	4	3	-87.2	1.3	-3.1	2
03/2019											
Ata19-115	0.36	0.14	0.74	0.26	-32	3	2	-36.5		-42.4	1
SE area											
09/2017											
Ata17-217	-4.75	0.13	-9.02	0.25	19	16	4	-81.4	0.7	-9.3	2
Ata17-219	-3.63	0.15	-6.85	0.28	-13	1	2	-73.0	0.1	-18.2	2
Ata17-220	-4.21	0.03	-7.99	0.07	17	8	2	-75.0	0.2	-11.0	2
Ata17-222	-0.95	0.00	-1.75	0.01	-31	8	2	-45.9	0.1	-31.9	2
Ata17-223	-3.95	0.05	-7.47	0.08	5	3	2	-75.4	0.5	-15.7	2
Ata17-224	-4.32	0.00	-8.13	0.01	-21	12	2	-79.5	0.4	-14.5	2
Ata17-225	-5.93	0.03	-11.23	0.04	16	5	2	-91.1	0.1	-1.3	2
Ata17-226	-5.41	0.07	-10.24	0.15	14	9	2	-84.4	0.8	-2.5	2

(continued)

Ata17-227	-2.21	0.01	-4.15	0.03	-19	5	2	-60.5	0.0	-27.3	2
03/2019											
Ata19-031	-0.47	0.05	-0.87	0.10	-17	3	2	-45.1		-38.1	1
Ata19-032	3.53	0.14	6.76	0.29	-38	13	3	-10.0		-64.1	1
Ata19-033	7.20	0.10	13.89	0.17	-108	5	2	10.7		-100.4	1
SW area											
09/2017											
Ata17-215	6.44	0.11	12.43	0.22	-102	11	4	30.8	0.4	-68.6	2
09/2018											
Ata18-046a	-2.94	0.08	-5.54	0.16	-13	3	4	-69.0		-24.6	1
Ata18-052	4.48	0.04	8.63	0.06	-61	5	2	12.7		-56.3	1
Ata18-053a	-2.70	0.09	-5.09	0.16	-14	4	3	-66.8		-26.1	1
Ata18-056a	7.53	0.05	14.50	0.09	-98	5	4	38.0		-78.0	1
Ata18-058	5.74		10.55		-82		1	18.9	1.3	-65.5	2
Ata18-061	-2.33	0.03	-4.40	0.05	-11	1	3	-57.9		-22.8	1
03/2019											
Ata19-038	-0.32	0.01	-0.56	0.02	-24	0	2	-43.2		-38.7	1

A.2 Supplementary material to Chapter 6

A2.1 Boundary Conditions

The C-G model consists of three equations (δ^2H, $\delta^{17}O$, $\delta^{18}O$) with at least six variables (δ_{WI}, δ_V, T, h, n, E/I). Some of these variables can be independently constrained considering the environmental setting (coastal, continental, low/high altitude, low/high latitude) and site information gained from other archives.

A2.1.1 Isotopic composition of inflowing water

The isotopic composition of inflowing water can be appropriately estimated from the evaporation trend spanned by measured isotopic data (Fig. 6.2, cf. section 6.7.1). High $\delta^{18}O_{AW}$ values (> 2 ‰) in samples from Mejillones indicates that the paleo-lake might be recharged by seawater. This is consistent with the proposed marine origin and the coastal position of the gypsum deposits on the Mejillones Peninsula (Di Celma et al., 2014). Considering spatial and glacial-interglacial variability in ocean's isotope composition the $\delta^{18}O$ of seawater can range between -1 and +1 ‰ (Shackleton and Kennett, 1975; Schrag et al., 2002). Since changes in ice sheet volume introduced low variability in $^{17}O\text{-excess}_{sea}$ and $d\text{-excess}_{sea}$ (Schrag et al., 2002; Sengupta and Pack, 2018), modern average values of -5 per meg and 0 ‰ were used (Luz and Barkan, 2010).

The Tiliviche data indicates a $\delta^{18}O_{WI}$ value between -12 and -6 ‰ (cf. Fig. 6.2), which is comparable to the isotopic composition of modern groundwaters and rivers in the northern part of the Atacama Desert (Aravena, 1995). Sedimentologic and geomorphologic investigations in the study area indicate that the lake may have been recharged by streams draining headwaters from the high Andes (Kirk-Lawlor et al., 2013). The modern isotopic composition of stream water from Quebrada Tiliviche ($\delta^{18}O$ = -9.0 ‰) and Quebrada Aroma ($\delta^{18}O$ = -7.3 ‰) that probably contributed to the Tiliviche paleo-lake, coincides well with the isotopic composition of inflow water indicated by SBW of gypsum samples from the Tiliviche site (cf. Fig. 6.2).

In other continental lake settings, the isotopic composition of inflowing water may be estimated from paleo-precipitation recorded in speleothems, paleo-groundwaters and ice cores (Gázquez et al., 2018). Care must be taken, if the lake received water by streams, since they can be very different in isotopic composition compared to local precipitation. However, as for the Tiliviche site, there might be geomorphologic evidence for this.

A2.1.2 Isotopic composition of atmospheric vapor

The isotopic composition of atmospheric vapor is difficult to constrain because recent measurements are scarce and there are no estimates about changes in the past. The coastal position of the Mejillones site implies a marine source of atmospheric vapor. The flux of evaporating water vapor from seawater can be calculated by (Barkan and Luz, 2007):

$$R_V = R_E = \frac{R_{sea}}{\alpha_{diff} \cdot (1 - h) + h) \cdot \alpha_{eq}}$$

where R_{sea} and R_E are the isotopic ratios of seawater and evaporating vapor, respectively. Assuming that the relative humidity h above the sea ranges between 70-100 %, $\delta^{18}O_V$ can vary from -12.5 to -9.5 ‰. Two measurements of atmospheric vapor at Antofagasta located 30 km south of the Mejillones Peninsula, yield an average $\delta^{18}O_V$ of -12.2 ± 0.6 ‰ within the assumed range (cf. Table A.1.3). Values of d-excess$_V$ and ^{17}O-excess$_V$ of atmospheric vapor above the ocean were estimated using the humidity relationship defined by Uemura, et al. (2008, 2010).

The Tiliviche site is located at about 10 km distance from the coast indicating that atmospheric moisture is mainly derived by advection of marine air masses. The frequent occurrence of fog in austral winter supports this hypothesis (Hoffmeister, 2018). Due to ascent of air masses along the Coastal Cliff (~1000 m) and the formation of clouds, the $\delta^{18}O_V$ will be more depleted. At Salar de Llamará that is located even further inland (80 km distance from the coast at 750 m a.s.l.) measured $\delta^{18}O_V$ range around -15.0 ± 1.9 ‰. Thus, constraining $\delta^{18}O_V$ between -15 and -12 ‰ seems reasonable for Tiliviche.

A2.1.3 The turbulence coefficient

The turbulence coefficient is an empirical parameter that usually ranges between 0.5 (turbulent) and 1.0 (no wind) in natural environments (Dongmann et al., 1974; Merlivat and Jouzel, 1979; Gonfiantini, 1986; Mathieu and Bariac, 1996; Gázquez et al., 2018; Surma et al., 2018). Its value may be estimated from wind speed (Merlivat and Jouzel, 1979), however, their relationship is not yet fully understood. Wind significantly increases evaporation rates. Hence, it is reasonable to assume that wind conditions in times of high evaporation are generally rough. The turbulence coefficient can be well approximated by pan evaporation experiments data. Turbulence coefficients determined from evaporation experiments performed by Surma et al. (2018) at the Salar de Llamará (n = 0.5) and from experiments of a study at the Salar del Huasco presented within this

thesis (Chapter 5) (n = 0.54) are in good agreement. Defining $n = 0.5 \pm 0.1$ appears to be reasonable for wind conditions in the Atacama Desert.

A2.1.4 Evaporation to inflow ratio (E/I)

The hydrologic balance of the lake (E/I) has a large impact on the isotopic composition of lake water. The E/I ratio may be estimated by simple mass balance of conservative elements (e.g. K, Cl) in modern lake water (Surma et al., 2018). However, E/I of fossil lakes are difficult to constrain. In our model, the isotopic composition of evaporated recharged lakes is determined in dependence on the E/I ratio. Thus, it is only necessary to constrain a maximum E/I ratio (E/I_{max}). In principal, long-term steady state conditions ($E/I \leq 1$) are required to precipitate large amounts of gypsum, because hydrological unbalance ($E/I > 1$) would lead to desiccation of lakes within months. However, in complex and dynamic lakes that are episodically flooded, e.g. during storm events, individual ponds with apparent $E/I > 1$ can be maintained permanently or at least over significant timescales. Frequent flooding events can produce extensive gypsum deposition at hydrologically unbalanced conditions implying that the restriction of $E/I = 1$ should be relaxed to some degree. Assuming $E/I_{max} = 1.2$ appears to be a reasonable approximation.

Figure A2.1: Sampling sites at Mejillones (23°20.14'S 70°32.85'W). Sample names are indicated on the photos.

Figure A2.2: Sampling sites at Tiliviche (19°33.90'S 70°07.05'W). Sample names are indicated on the photos.

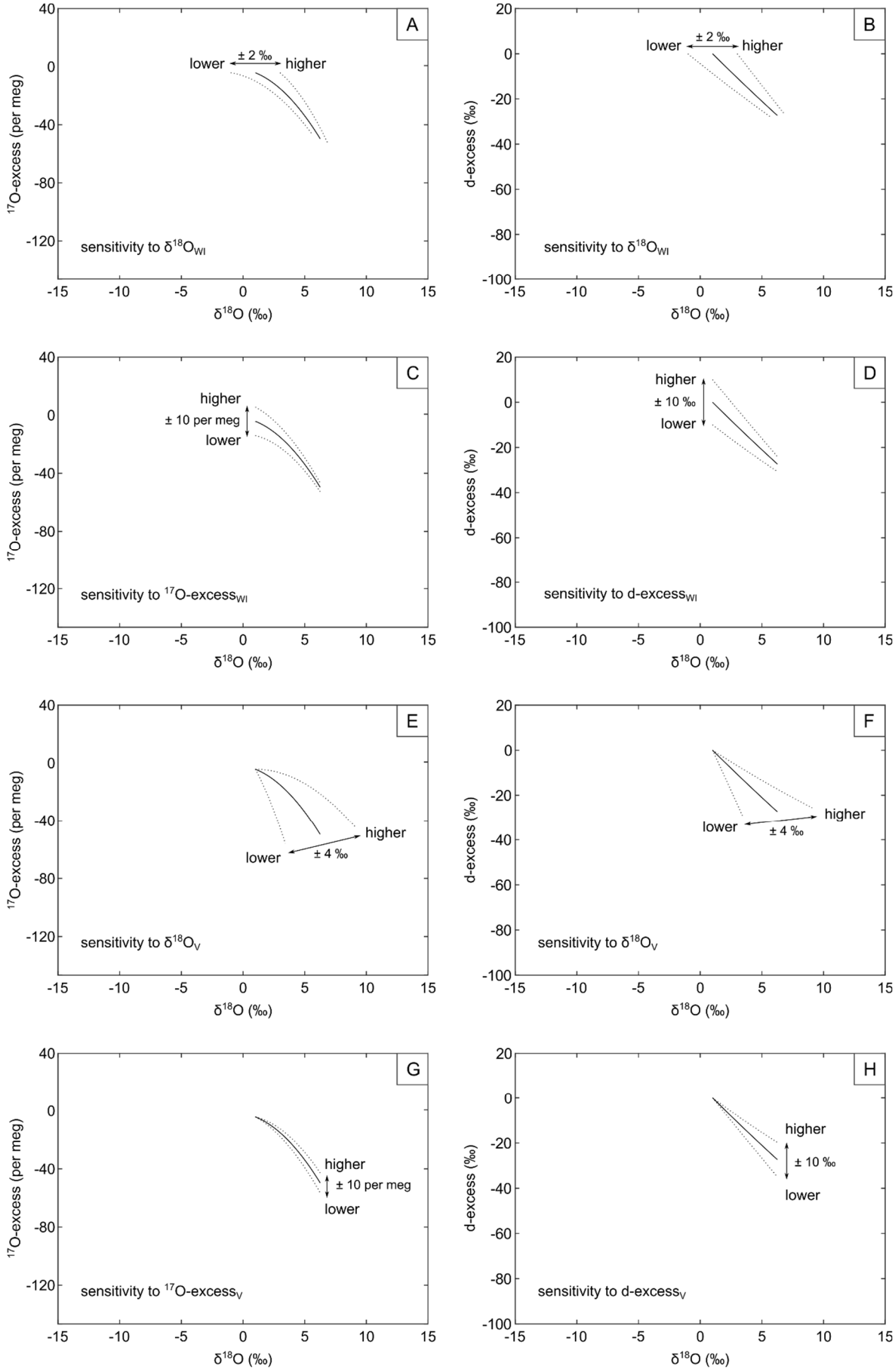
A
lower
± 2 ‰
higher
sensitivity to δ18OWI
17O-excess (per meg)
δ18O (‰)
B
lower
± 2 ‰
higher
sensitivity to δ18OWI
d-excess (‰)
δ18O (‰)
C
higher
± 10 per meg
lower
sensitivity to 17O-excessWI
17O-excess (per meg)
δ18O (‰)
D
higher
± 10 ‰
lower
sensitivity to d-excessWI
d-excess (‰)
δ18O (‰)
E
higher
lower
± 4 ‰
sensitivity to δ18OV
17O-excess (per meg)
δ18O (‰)
F
lower
higher
± 4 ‰
sensitivity to δ18OV
d-excess (‰)
δ18O (‰)
G
higher
± 10 per meg
lower
sensitivity to 17O-excessV
17O-excess (per meg)
δ18O (‰)
H
higher
± 10 ‰
lower
sensitivity to d-excessV
d-excess (‰)
δ18O (‰)

(continued)

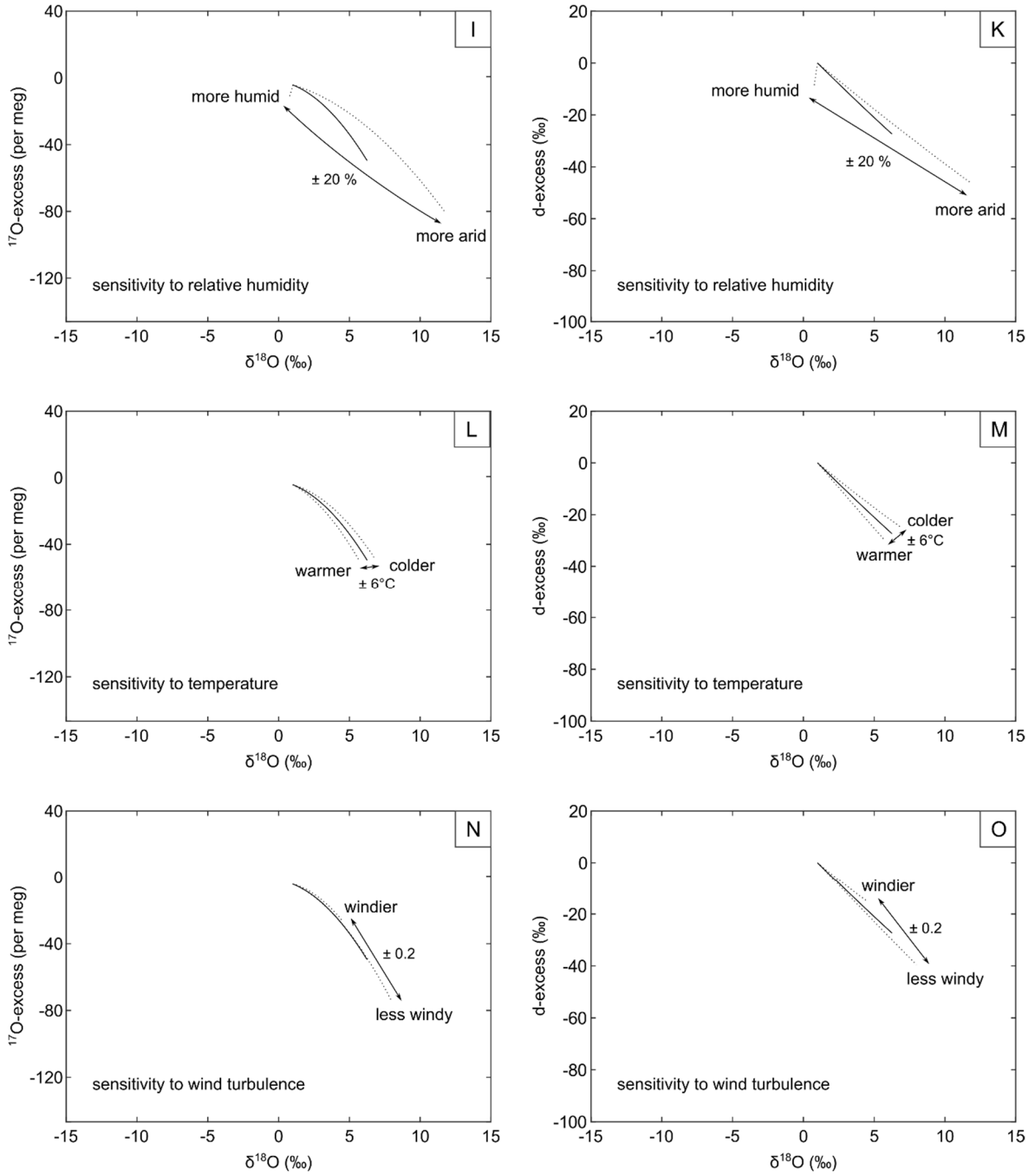

Figure A2.3: Sensitivity of evaporation trajectories in plots of ^{17}O-excess over δ^{18}O and d-excess over δ^{18}O to different input parameters for the present environmental conditions at the Mejillones site. Evaporation trajectories have been modeled for hydrologically balanced conditions ($E/I \leq 1$) at variable isotopic composition of inflowing water (A-D), isotopic composition of atmospheric vapor (E-H), relative humidity (I-K), temperature (L-M), and turbulence coefficient (N-O). Model input parameters are: $\delta^{18}O_{WI} = 0$ ‰, ^{17}O-excess$_{WI} = -5$ per meg, d-excess$_{WI} = 0$ ‰, $\delta^{18}O_V = -12$ ‰, ^{17}O-excess$_V = 0$ per meg, d-excess$_V = 0$ ‰, h = 70 %, T = 16°C, n = 0.5.

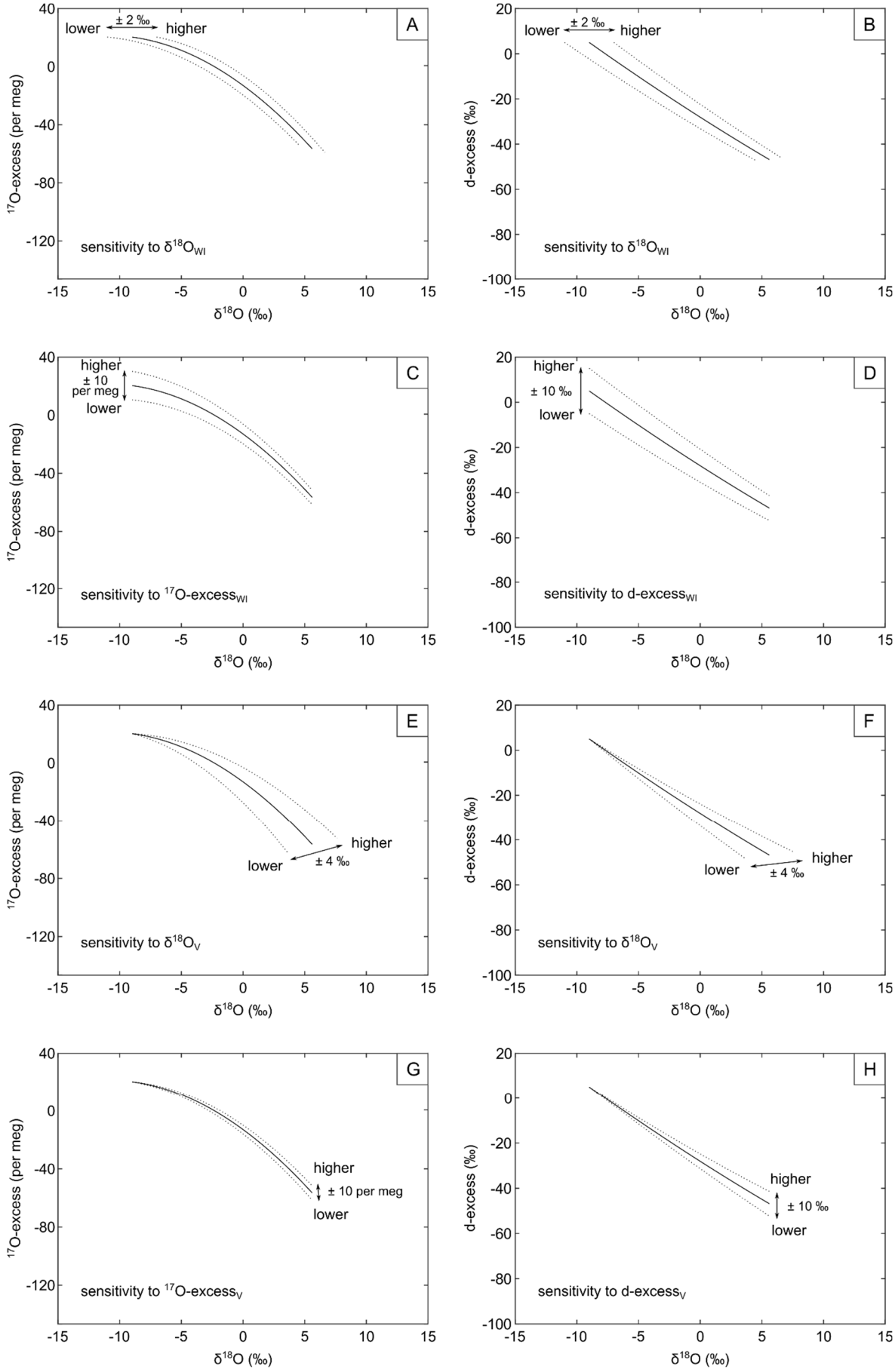
A
lower
± 2 ‰
higher
sensitivity to δ18OWI
17O-excess (per meg)
δ18O (‰)
B
lower
± 2 ‰
higher
sensitivity to δ18OWI
d-excess (‰)
δ18O (‰)
C
higher
± 10
per meg
lower
sensitivity to 17O-excessWI
17O-excess (per meg)
δ18O (‰)
D
higher
± 10 ‰
lower
sensitivity to d-excessWI
d-excess (‰)
δ18O (‰)
E
lower
higher
± 4 ‰
sensitivity to δ18OV
17O-excess (per meg)
δ18O (‰)
F
lower
higher
± 4 ‰
sensitivity to δ18OV
d-excess (‰)
δ18O (‰)
G
higher
± 10 per meg
lower
sensitivity to 17O-excessV
17O-excess (per meg)
δ18O (‰)
H
higher
± 10 ‰
lower
sensitivity to d-excessV
d-excess (‰)
δ18O (‰)

(continued)

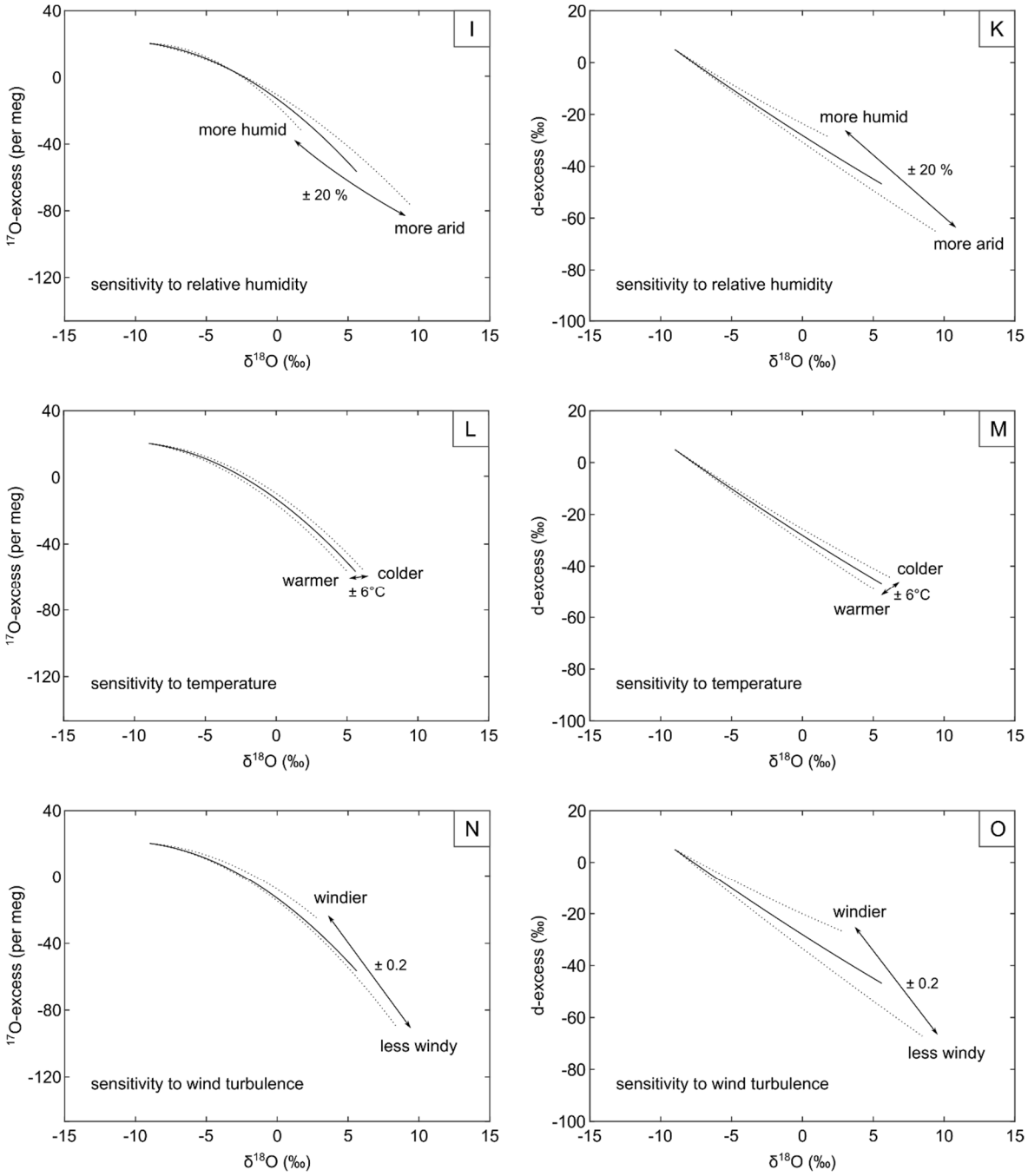

Figure A2.4: Sensitivity of evaporation trajectories in plots of ^{17}O-excess over δ^{18}O and d-excess over δ^{18}O to different input parameters for the present environmental conditions at the Tiliviche site. Evaporation trajectories have been modeled for hydrologically balanced conditions ($E/I \leq 1$) at variable isotopic composition of inflowing water (A-D), isotopic composition of atmospheric vapor (E-H), relative humidity (I-K), temperature (L-M), and turbulence coefficient (N-O). Model input parameters are: $\delta^{18}O_{WI}$ = -9 ‰, ^{17}O-excess$_{WI}$ = 20 per meg, d-excess$_{WI}$ = 5 ‰, $\delta^{18}O_V$ = -14 ‰, ^{17}O-excess$_V$ = 10 per meg, d-excess$_V$ = 10 ‰, h = 50 %, T = 16°C, n = 0.5.

Table A2.1: Isotopic data of structurally bonded water (SBW) in gypsum samples from Mejillones (23°20.14'S 70°32.85'W) and Tiliviche (19°33.90'S 70°07.05'W). The isotopic composition of ambient water (AW) was calculated using $^{2}\alpha_{SBW\text{-}AW} = 0.9802$, $^{17}\alpha_{SBW\text{-}AW} = 1.0019$, and $^{18}\alpha_{SBW\text{-}AW} = 1.0035$ (20°C) (Gázquez et al., 2018).

sample	$\delta^{2}H_{SBW}$ (‰)	1σ SD	$\delta^{17}O_{SBW}$ (‰)	1σ SD	$\delta^{18}O_{SBW}$ (‰)	1σ SD	$\delta^{2}H_{AW}$ (‰)	$\delta^{17}O_{AW}$ (‰)	$\delta^{18}O_{AW}$ (‰)	$^{17}O\text{-excess}_{AW}$ (per meg)	$d\text{-excess}_{AW}$ (‰)
Mejillones											
Ata19-001a	-1.3	1.6	4.02	0.21	7.67	0.41	18.8	2.16	4.15	-32	-14.4
Ata18-133a	6.6	2.4	4.74	0.01	9.08	0.03	26.9	2.88	5.56	-51	-17.6
Ata19-001c1_top	6.9	1.0	5.12	0.03	9.78	0.05	27.2	3.26	6.25	-36	-22.9
Ata19-001c1_bottom	9.5	1.4	5.66		10.85		29.8	3.80	7.32	-57	-28.7
Ata19-001c2	-1.2	0.2	4.85	0.06	9.28	0.18	18.9	2.99	5.76	-46	-27.1
Ata19-001d4	1.3	1.7	4.81	0.02	9.23	0.03	21.4	2.95	5.70	-57	-24.2
Ata19-001d5	4.9	0.2	5.51		10.58		25.1	3.65	7.05	-71	-31.3
Ata19-001d6	5.1	0.1	5.70	0.01	10.96	0.05	25.4	3.83	7.43	-83	-34.0
Ata19-001f_top	6.8	0.1	4.58		8.75		27.1	2.72	5.23	-37	-14.7
Ata18-133b	6.0	2.0	4.44		8.51		26.9	2.88	5.56	-51	-17.6
Tiliviche											
Ata17-069a_I	-65.6	0.3	-0.35	0.17	-0.66	0.34	-46.7	-2.20	-4.15	-12	-14
Ata17-069a_II	-72.6	0.5	-0.94		-1.78		-53.9	-2.79	-5.27	-9	-12
Ata17-069a_III	-74.7	2.3	-1.09	0.23	-2.06	0.43	-56.0	-2.94	-5.54	-8	-12
Ata17-069a_IV	-65.4	0.4	0.06		0.13		-46.5	-1.80	-3.36	-20	-20
Ata18-025a	-72.8	0.6	-1.20	0.15	-2.27	0.29	-54.1	-3.05	-5.76	-4	-8
Ata18-025b	-70.5	0.2	-0.53	0.40	-0.98	0.78	-51.7	-2.38	-4.47	-19	-16
Ata18-025c	-71.1	0.0	-1.07	0.13	-2.00	0.24	-52.4	-2.92	-5.49	-15	-8
Ata18-025x	-71.1	0.3	-1.37		-2.61		-52.4	-3.22	-6.09	3	-4

A.3 Supplementary material to Chapter 7

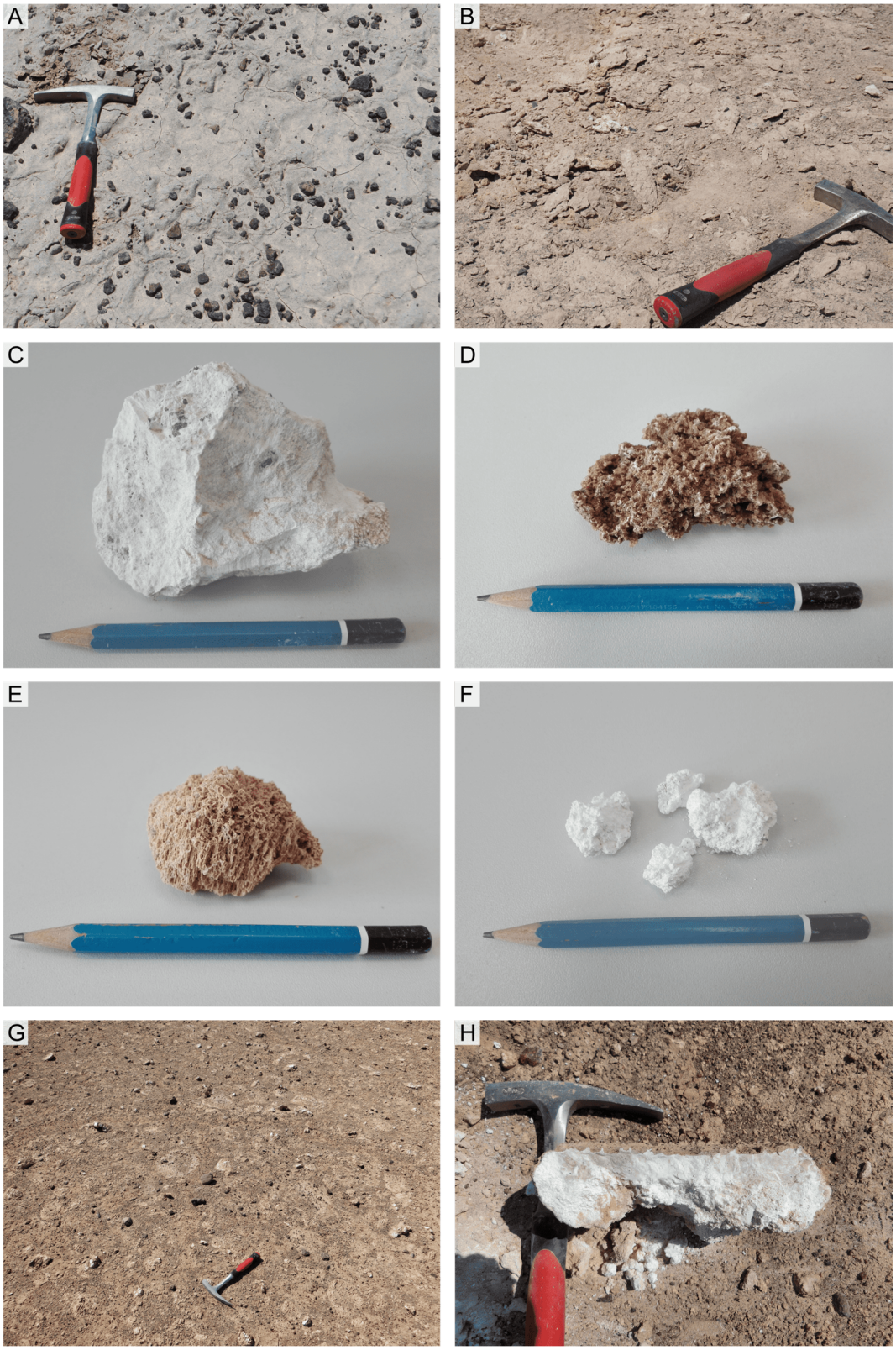

Figure A3.1: A-B – Well developed gypsiferous surface crusts that protect underlying loose material from erosion. C-F – Different types of sub-surface concretions observed in Atacama soils. The pen is about 10 cm long. G – Surface concretions embedded in residual chuca material. H – Cross section of a surface concretion.

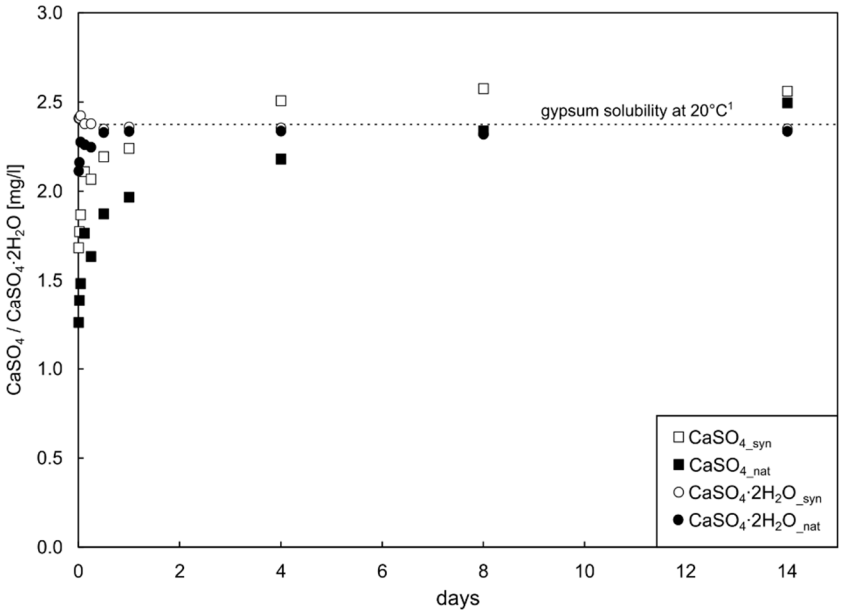

Figure A3.2: Time series leaching experiment of gypsum (circles) and anhydrite (squares). Open symbols represent synthetic gypsum/anhydrite samples, while filled symbols indicate natural soil gypsum/anhydrite samples from the Atacama Desert. The gypsum solubility of 2.4 $g \cdot l^{-1}$ is illustrated by the dashed black line (Bouis, 2006).

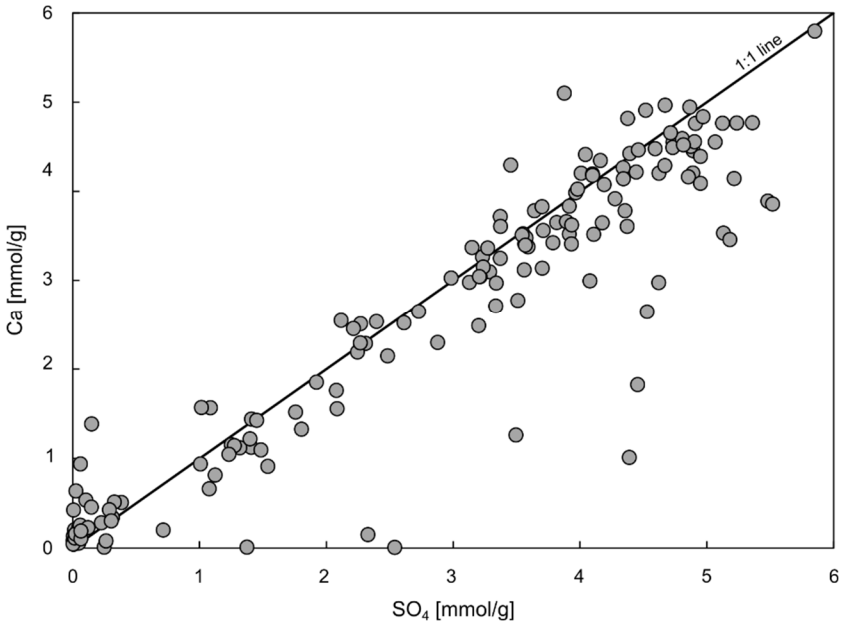

Figure A3.3: Ca in residue vs total sulfate in bulk sediment samples. Most of the samples follow a 1:1 relationship as indicated by the solid line. Deviations may occur due to the presence of sulfates other than $CaSO_4$ or calcium containing salts in bulk sediment samples as occasionally indicated by XRD analyses.

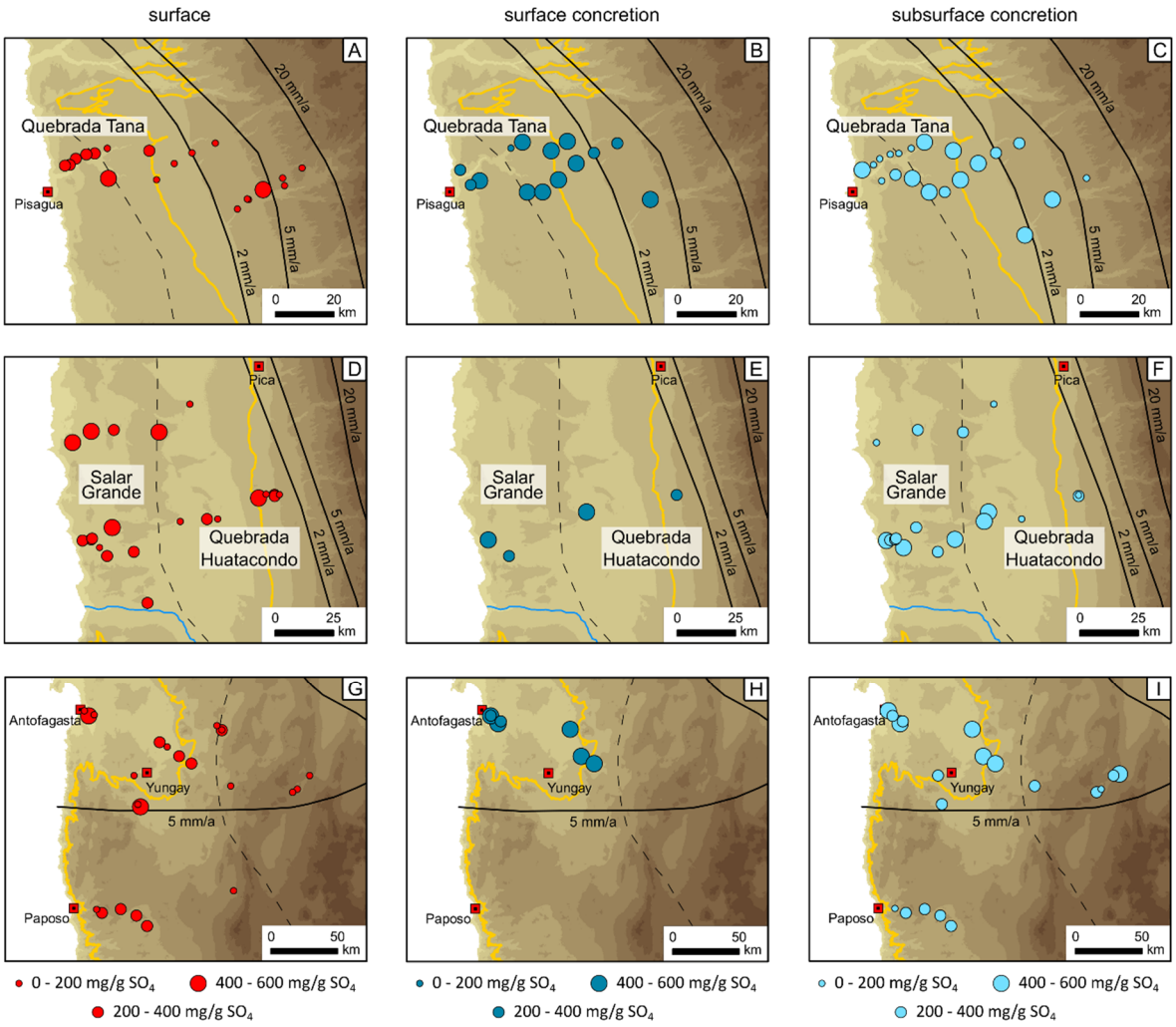

Figure A3.4: Sulfate concentrations in surface samples (red), surface concretions from deflated/eroded surfaces (dark blue) and sub-surface concretions (light blue) divided in three categories: low (0-200 mg·g^{-1}), moderate (200-400 mg·g^{-1}), and high (400-600 mg·g^{-1}). For map features cf. Fig 7.1.

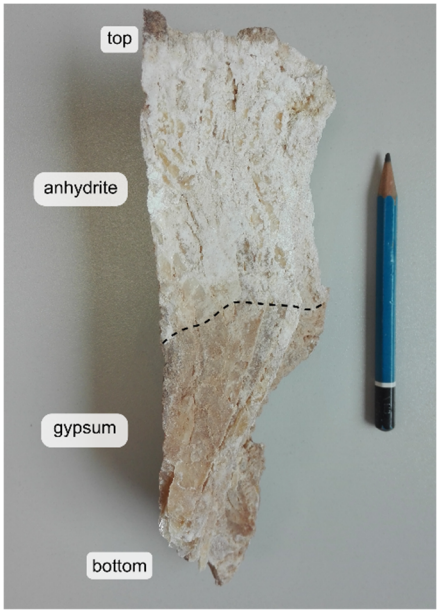

Figure A3.5: Selenite sample from the Atacama Desert. The upper part, which cropped out at surface, consists of secondary formed anhydrite, while the lower part remains gypsum. The pen is about 10 cm long.

Erklärung

Ich versichere, dass ich die von mir vorgelegte Dissertation selbständig angefertigt, die benutzten Quellen und Hilfsmittel vollständig angegeben und die Stellen der Arbeit – einschließlich Tabellen, Karten und Abbildungen –, die anderen Werken im Wortlaut oder dem Sinn nach entnommen sind, in jedem Einzelfall als Entlehnung kenntlich gemacht habe, dass diese Dissertation noch keiner anderen Fakultät oder Universität zur Prüfung vorgelegen hat, dass sie – abgesehen von unten angegebenen Teilpublikationen – noch nicht veröffentlicht worden ist sowie, dass ich eine solche Veröffentlichung vor Abschluss des Promotionsverfahrens nicht vornehmen werde. Die Bestimmungen der Promotionsordnung sind mir bekannt. Die von mir vorgelegte Dissertation ist von Prof. Dr. Michael Staubwasser betreut worden.

Cologne, 23.03.2020

– Claudia Voigt –

Folgende Teilpublikationen liegen vor:

Voigt, C., Klipsch, S. Herwartz, D., Chong, G., Staubwasser, M., 2020. The spatial distribution of soluble salts in the surface soil of the Atacama Desert and their relationship to hyperaridity. Global and Planetary Change, 184, 103077. https://doi.org/10.1016/j.gloplacha.2019.103077